Analytical modeling of electret-based microgenerators under sinusoidal vibrations

by

Cuong Nguyen

A thesis submitted for the degree of

Master of Philosophy

in

Electrical and Electronic Engineering

School of Electrical and Electronic Engineering

Faculty of Engineering, Computer and Mathematical Sciences,

THE UNIVERSITY OF ADELAIDE,

Adelaide, South Australia.

August 2017.

Supervisors:

Dr Said Al-Sarawi, Centre for Biomedical Engineering, School of Electrical and Electronic Engineering

Dr Damith Ranasinghe, Auto-ID Lab, School of Computer Science.

Statement of originality

I certify that this work contains no material which has been accepted for the award of any other degree or diploma in my name, in any university or other tertiary institution and, to the best of my knowledge and belief, contains no material previously published or written by another person, except where due reference has been made in the text. In addition, I certify that no part of this work will, in the future, be used in a submission in my name, for any other degree or diploma in any university or other tertiary institution without the prior approval of the University of Adelaide and where applicable, any partner institution responsible for the joint-award of this degree.

I give consent to this copy of my thesis when deposited in the University Library, being made available for loan and photocopying, subject to the provisions of the Copyright Act 1968.

I acknowledge that copyright of published works contained within this thesis resides with the copyright holder(s) of those works.

I also give permission for the digital version of my thesis to be made available on the web, via the Universitys digital research repository, the Library Search and also through web search engines, unless permission has been granted by the University to restrict access for a period of time.

Cuong Nguyen

August 2nd, 2017.

Abstract

Recent advances in microfabrication technologies and electronics have led to a vast reduction in sizes and power consumption of electronic circuitry. This has revolutionized the field of wireless sensor networks, and in particular, Internet-of-Things, with a booming number of applications that enable the capabilities of autonomous sensing and monitoring. However, the implementation of such applications has been hindered by the slow development of scalable energy sources which provides power for operation. Batteries, which are the most common energy sources, have not kept pace with the demand of these developments. The challenge to provide power for microelectronic devices has, therefore, driven several innovations in vibration energy harvesting - a technology that has been flourished in recent years as a possible alternative to provide continuous energy for autonomous operation. During the last decade, a significant number of microscale vibratory energy harvesters has been fabricated using active materials (piezoelectric, ferroelectric and magnetoelectric) or exploiting the electromechanical coupling mechanisms (electromagnetic and electrostatic) to harvest energy from mechanical stimuli or ambient vibrations. Such transduction mechanisms have both benefits and limitations that vary depending on the employed technology and the targeted application. For miniaturization, electrostatic systems are favorable due to their compatibility with MEMS fabrication processes. In addition, electrostatic systems with pre-charged electrets can autonomously harvest energy to energize microelectronic devices such as wireless sensors and actuators. Hence, this transduction mechanism is selected as the topic of this research.

The main focus of this research is the analytical modeling approach that provides insights into the operating mechanism and trade-off involved when designing an electret-based microgenerator. Sinusoidal excitations which resemble ambient vibration stimuli were considered in this research. The modeling process was, firstly,

undertaken for a simple case when the vibration amplitude is small, and then extended and generalized for an arbitrary sinusoidal vibration. Under these conditions, an electret-based can be modeled as a sawtooth voltage source in series with an equivalent internal resistance, or a current source. These models were validated using a simulation-based method presented in the literature and showed good agreements. A performance optimization was also carried out by employing the proposed analytical model combined with voltage breakdown phenomenon and the limitation of material properties. However, a fully functional micro power generator driven by vibrations has yet to be demonstrated.

In summary, the research has expanded the capability of analytical modeling and understanding of electret-based microgenerators. These can be used in further studies and optimizations to achieve the ultimate goal of autonomous operation.

Acknowledgment

Throughout this research, I have had the chance to learn, work and collaborate with many people. Although I cannot list all of them, I wish to acknowledge some who are particularly helpful.

Dr Said Al-Sarawi and Dr Damith Ranasinghe have fully supported the project from the very beginning. Their energy and intellectual expertise have helped to shape the direction of the research. I also appreciate their fully-hearted support during the mixture of good and difficult periods that happened along my research to encourage and give me useful advice to overcome and complete this work.

I would like to thank many colleagues, including Alban O'Brien, Aubrey Slater, Brandon Pullen, Danny Di Giacomo, Hayden Westell, Ian Linke and Mitchell Carli for their promptly support in order to setup a facility for prototyping, in spite of the limited resources available, and Zeyu Wang for his work that performed experiments to test a prototype. I would also like to thank the kind support from School of Chemical Engineering, the University of Adelaide, especially the research group of Dr Dusan Losic, for helping to deposit thin polymer films and perform some trials of corona treatments.

I acknowledge the support I have received for my research through the Collaboration Pathway Program (CPP 39) from the Department of State Development of South Australia Government. I also acknowledge the South Australia node of the Australian National Fabrication Facility, a company established under the National Collaborative Research Infrastructure Strategy to provide nano and micro-fabrication facilities for Australias researchers, for providing a free training and access to the IntelliSense software.

Finally, I am grateful to my parents and sister for their constant love, support and confidence in me.

Publications

Journal articles

Nguyen, C. C., Ranasinghe, D. C., & Al-Sarawi, S. F. (2017). Analytical modeling and optimization of electret-based microgenerators under sinusoidal excitations, *Microsystem Technologies*, pp. 1-11. DOI: 10.1007/s00542-017-3349-1.

Nguyen, C. C., Ranasinghe, D. C., & Al-Sarawi, S. F. (2017). Electret-based microgenerators under sinusoidal excitations: an analytical modeling. Submitted.

Contents

List of Figures

List of Tables

Chapter 1

Introduction

This chapter introduces the four essential ambient energy sources which can be harvested to energize wireless sensors and actuators. The strengths and weaknesses of each harvesting technology are also discussed to select the most suitable method that can provide power for the operation of microelectronics, and in particular, wearable devices. Subsequently, the aim and objectives of the research are presented. This chapter also includes the overview of this thesis which outlines the content of each chapter.

1.1 Motivation for energy harvesting

The fast-growing development in microfabrication technologies within the last few decades has led to the vast reduction in the size and power consumption of electronic circuitry. Such compact and scalable components with their little power levels have revolutionized different fields of technology, including but not limited to miniature sensors and actuators, data transmitters, controllers and medical implants. These innovations have enabled the possibilities of many applications, which employ hundreds of thousands of micro-scale devices connected into many networks to gather relevant information from many sources to monitor the physical or environmental conditions for planning and decision making. Traditionally, these networks are powered by hard electrical wire, which represents many drawbacks, including high installation and maintenance costs and preventing the further expansion of remote applications. To avoid such issues, devices with wireless interfaces have recently been proposed and are currently being implemented to replace the older hard wi-

red ones (Akyildiz et al. 2002). Such enhancements provide similar functionalities at a lower cost and a higher spatial density of network distribution, opening more opportunities for further expansion and deployment.

Unfortunately, further evolution of these technologies has been hindered by the lack of scalable energy sources which are necessary to provide power for operation. Batteries, which remain the most widely used power sources, have not kept pace with the ever-increasing demands of these fast-growing technologies (Paradiso & Starner 2005). As a result, the problem of powering many nodes in a dense network is very challenging due to the nightmare of replacing and disposing of depleted batteries. In some critical situations such as electronic implants, changing battery may also accompany with surgeries which are extremely undesirable (Görge et al. 2001, Lo & Yang 2005). Such challenges have, therefore, driven several innovations in the field of energy harvesting to develop compact and scalable generators which can transfer available ambient energy to electricity. Ongoing developments include many harvesting methods and designs to improve the energy conversion efficiency to provide a continuous power supply to enable long-term and autonomous operation of microelectronic devices (Sudevalayam & Kulkarni 2011).

Being inspired by the ubiquitous capability of energy harvesting techniques, the research undertaken in this thesis is to investigate and design a small scale generator to be combined with wearable devices, corresponding to a wireless network with only a few nodes, used in human tracking applications such as patient care or fall detection for elderly people. The next section presents a brief discussion of some

Table 1.1. Four essential ambient energy sources that can be harvested (Mikeka & Arai 2011).

Energy source	**Power density (per cm^3)**
Photovoltaic	10 μW to 10 mW
Radio frequency (RF)	0.01 μW to 0.1 μW
Thermal	20 μW to 10 mW
Vibration	4 μW to 100 μW

primary energy harvesting technologies, including their strengths and weaknesses in regard to small-scale applications to select the appropriate technology for the research topic.

1.2 Energy harvesting technologies

In general, renewable energy can be obtained from the four essential ambient sources shown in Table 1.1. The technologies that harvest energy from these sources have their own advantages and disadvantages and the choice of a technology mostly depends on the availability of the energy sources in the application's environment. This section outlines the practicability of these energy harvesting technologies with a focus on wearable devices.

1.2.1 Light or solar energy

Solar energy in one form or another is the source of nearly all energy on the earth. According to the daily total solar irradiance from the Solar Radiation and Climate Experiment (SORCE) shown in Figure 1.1a, the power density received on Earth's surface is approximately 100 mW/cm^2, which can be harvested to charge batteries, supply power for the facility grid or even power off-the-grid areas (Akikur et al. 2013). A solars photovoltaic system can be realized as solar panels consist of silicon crystalline solar cells with an efficiency ranging from 12 percent for matured materials to 38 percent for recently developed materials (Green et al. 2015). In a sunny day, a common solar panel can generate up to 300 W, which can be used to power the lighting system of a regular-size house. The technology quite advantages in macro scale due to the huge amount of availability and high power density compared with other energy harvesting methods as shown in Table 1.1. Given such advantages, solar energy is one of the most popular renewable energy sources with an exponential growing number of installation throughout the world as depicted in Figure 1.1b

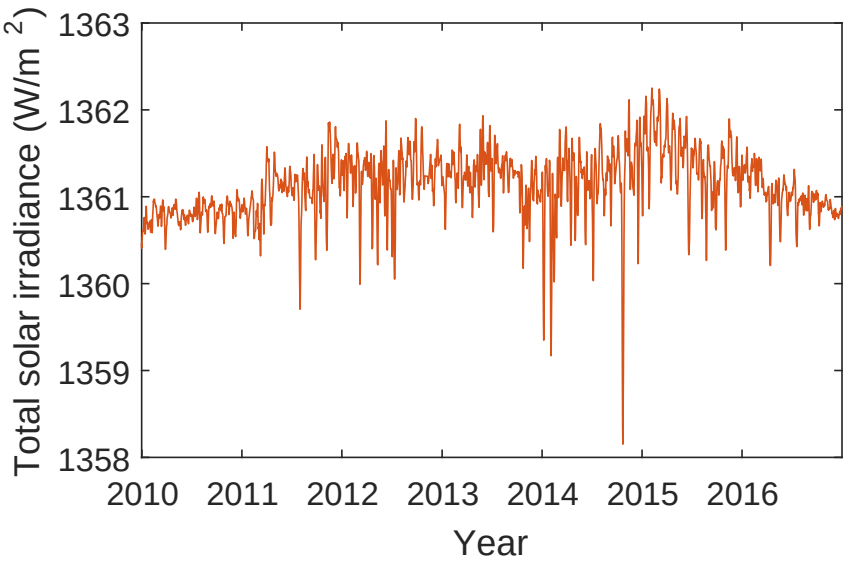

(a)

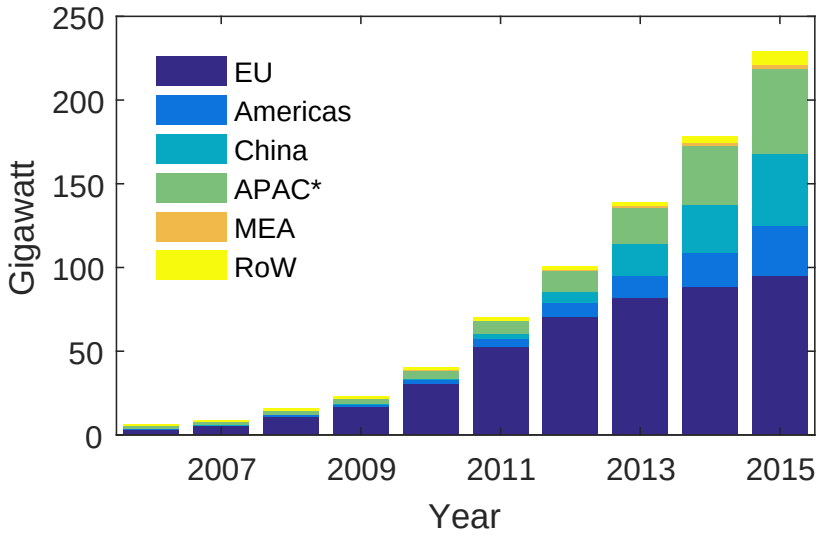

(b)

Figure 1.1. (a) Daily total solar irradiance measurement from the Solar Radiation and Climate Experiment (SORCE) shows that more than a 1 kW/m^2 is available for harvesting, and (b) evolution of global total solar photovoltaic installed capacity taken from SolarPower Europe - Global Market Outlook for Solar Power 2016 - 2020. APAC* is Asian Pacific region excluding China, MEA stands for Middle East and Africa, while RoW stands for rest of the world.

(SolarPower Europe 2016).

At the micro scale, the performance of photovoltaic systems, however, fall off dramatically due to the lack of light availability, especially under indoor conditions. As shown in Table 1.2, a reduction of more than 2000 times is observed when moving

from an outdoor to an indoor environment measured by a 15 percent efficient solar cell. As a result, solar energy harvesting is unsuitable for the applications of mobile and wearable devices where the indoor condition is most likely dominant.

1.2.2 Radio frequency

Harvesting RF energy is also a potential approach due to the availability of RF signals in today's urban landscapes. A major limitation of RF energy harvesting is a very low conversion efficiency and associated power density levels. One can estimate the performance of an RF energy harvester by calculating the power density of the device's receiving antenna E/Z_0, where E is the local electric field and $Z_0 = 376.7\ \Omega$ is the radiation resistance of free space. For an electric field $E = 1\ \mathrm{V/m}$, the maximum energy harvested is 0.26 $\mu\mathrm{W/cm^2}$, which is insufficient to power microelectronics. Higher field strengths are rarely observed due to the risk to the human body and regulated by the International Commission on Non-Ionizing Radiation Protection (Ahlbom et al. 1998). In addition, the power received by an RF harvester decreases dramatically as the distance from the source transmitter increases (Mur-Miranda et al. 2010). To maximize the energy harvested, RF energy harvesters need to be designed with either large collection antennas or placing in a close proximity to an RF transmission source, which is beyond the practical usage in mobile and wearable applications.

Another RF-based approach is, according to (Paradiso & Starner 2005), active wireless power transfer which was initiated from the idea of long distance power trans-

Table 1.2. Solar power density measurements taken under various conditions. Data is taken from Roundy et al. (2003*a*).

Condition	**Power density (μW/cm^2)**
Outdoor - midday	14,000
4 inch from 60 W light bulb	5,000
50 inch from 60 W light bulb	567
Office lighting	6.5

fer proposed by Tesla in 1897 (Tesla 1897). This technology is now widely known as the wireless charging or wireless power transfer which is widely applied in medical and smart home or smart house applications. Similar to the passive RF energy harvesting, the active power transfer technology has a major weakness of a low efficiency and requires transmitters to be close to receivers. The amount of power transferred is also limited due to the concern of human health when exposed to time-varying electromagnetic fields (Ahlbom et al. 1998). Moreover, cost is a critical issue when implementing the technology in large-scale applications due to the increasing number of RF transmitters installed. Research in this field is still active to improve further signal rectification efficiency as well as bring down the installation cost.

1.2.3 Thermal gradient

Thermoelectric generation is another energy harvesting method that generates electricity when there is a temperature difference formed between two dissimilar conductors or semiconductors. A thermoelectric generator consists of a number of thermocouples illustrated in Figure 1.2, connected in either series or parallel depending on whether an output voltage or current is prioritized (Montecucco et al. 2014). For the applications with low thermal gradients, series array configurations are preferred to maximize the output voltage and therefore, eases the rectification and conditioning processes.

The principle operation of thermoelectric generators is based on Seebeck's effect, which can be described by the creation of an electromotive field when there is a difference in temperature between the two conductors, presented as

$$E_{\text{emf}} = s\,\nabla T, \tag{1.1}$$

where s is the Seebeck coefficient, also known as thermopower, and ∇T is the thermal gradient between the hot and cold junctions of the generator.

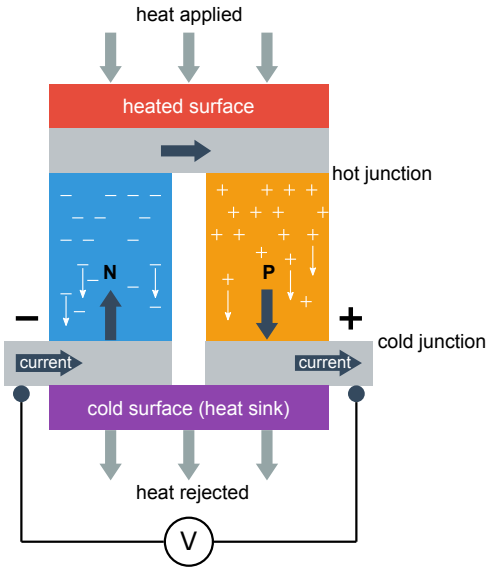

Figure 1.2. Diagram of a thermocouple generating electricity based on Seebeck's effect.

To increase the output voltage, materials with high Seebeck coefficient are required. Table 1.3 presents the Seebeck coefficients of most metals at room temperature. The great majority has Seebeck coefficients much smaller than 10 μV/m which is insufficient for power generation. Recently, some semiconductor materials have been discovered with Seebeck coefficients about 300 μV/m at usable temperature, which provide more advantages in term of power generated.

The most important factor that directly affects the effectiveness of thermoelectric generators is the availability of large thermal gradient between the two junctions given in equation (1.1). As a result, thermoelectric generation is only suitable for macro-scale applications such as houses and buildings. At a smaller scale such as human body, the technology is less attractive due to the extremely low power conversion efficiency.

1.2.4 Kinetic energy

Kinetic energy generation converts mechanical movement present in the application environment into usable energy. Kinetic energy has been harnessed along with the history of humanity. The early form of kinetic energy harvesters can be realized

Table 1.3. Seebeck coefficient of most metals (μV/m) at 300 K. Data source is from (Da Rosa 2012).

Metal	Seebeck coefficient	Metal	Seebeck coefficient	Metal	Seebeck coefficient	Metal	Seebeck coefficient
Ag	1.51	Eu	24.5	Nb	−0.44	Sr	1.1
Al	−1.66	Fe	15	Nd	2.3	Ta	1.9
Au	1.94	Gd	−1.6	Ni	−19.5	Tb	−1
Ba	12.1	Hf	5.5	Np	−3.1	Th	−3.2
Be	1.7	Ho	−1.6	Os	−4.4	Ti	9.1
Ca	10.3	In	1.68	Pb	−1.05	Tl	0.3
Cd	2.55	Ir	0.86	Pd	−10.7	Tm	1.9
Ce	6.2	K	−13.7	Rb	−10	U	7.1
Co	−30.8	La	1.7	Re	−5.9	V	0.23
Cr	21.8	Lu	−4.3	Rh	0.6	W	0.9
Cs	−0.9	Mg	−1.46	Ru	−1.4	Y	−0.7
Cu	1.83	Mn	−9.8	Sc	−19	Yb	30
Dy	−1.8	Mo	5.6	Sm	1.2	Zn	2.4
Er	−0.1	Na	−6.3	Sn	−1	Zr	8.9

as windmills or waterwheels which employ fluid flows to automate some intensive labor works. As the invention of electricity, kinetic energy has been the most common source to generate electricity to power facility grids in many major cities. In addition to the popular usage in macro-scale applications, small-scale kinetic energy generators have also been an interest of research, especially after the booming of microelectronics. Given the recent advances in standard microfabrication processes, the sizes of these generators can also be scaled down further, resulting in a higher possibility of integration into mobile and portable devices. Another essential advantage of these generators is the ability of power generation without the presence of light and thermal.

Small scale kinetic energy harvesting started to shape and evolve in the early of 2000s (Beeby et al. 2006, Mitcheson et al. 2008), including many designs based on a spring-mass-damper linear system with a fixed frequency. Such linear generators can be designed to efficiently operate under repeated excitations at many common locations shown in Table 1.4. To achieve the highest energy conversion efficiency, the

Table 1.4. Acceleration and frequency of common mechanical vibration sources in daily life (Lee et al. 2009, Aktakka et al. 2011, Romero et al. 2009).

	Source	Acceleration (m/s^2)	Frequency (Hz)
Enviroment	5-HP 3-axis machine tool	10	70
	Notebook computer (reading CD)	0.6	75
	Clothes dryer	3.5	120
	Second story of a wood frame building	0.2	100
	Railway	1.078 - 1.568	12-16
	Truck	1.96 - 3.43	8-15
	Ship	0.98 - 2.45	12-13
Human walking	Ankle	24.5 - 26.5	1.0 - 1.7
	Knee	16.7 - 19.6	1.7 - 2
	Hip	3.9 - 7.8	1.7 - 2
	Wrist	2.9 - 4.9	1 - 1.7
	Elbow	2.9 - 4.9	1.2 - 2
	Shoulder	2.9 - 3.9	1.7 - 2
	Chest	2.9 - 3.9	1.7 - 2
	Back of the head	3.9 - 6.9	0.8 - 2

fundamental frequencies of these small-scale energy harvesters must be tuned to be close to the forcing frequencies, also known as resonances. Recent research efforts, including the utilization of non-linear and non-resonant structures, have enabled more opportunities to harvest energy from non-periodic vibration sources such as human body. Nevertheless, the challenge in small-scale kinetic energy harvesting is the small available power density compared with other energy harvesting techniques shown in Table 1.1. As a result, active research is currently focusing on adaptive designs which can scavenge energy at wide bandwidth and low-frequency vibrations. A more in-depth discussion of this energy harvesting method will be presented in Chapter 2.

1.2.5 Comparison of different energy harvesting technologies

Table 1.5 summarizes the strengths and weaknesses of each energy source presented in this section. At large scale applications, light and thermal are the two most potential renewable energy sources for power generation; however, at a smaller scale, their

Table 1.5. Comparison of strengths and weaknesses between some widely-used energy harvesting technologies.

Technology	Advantage	Disadvantage
Solar	High power density	- Poor performance in indoor environment or at night time - High manufacturing and installation cost
RF	Always available	- Low power density - Low efficiency - High installation and maintenance cost when using active power transfer
Thermal	High availability	- Require temperature difference - Low energy conversion efficiency
Kinetics	- Operate without the need of light or thermal gradient - High scalability using standard microfabrication processes	- Inapplicable in stationary environment - Low energy density at low frequency excitations - Most designs have a narrow operating frequency bandwidth, resulting in a challenge when harvesting energy from unpredictable vibration sources.

effectiveness is dramatically reduced due to the low availability. In addition, the two energy harvesting methods are limited in some environments where photonics and temperature difference are absent. In contrast, RF energy is highly available and scalable using the advances in microelectronic circuitry. Recent development in RF active power transfer has focused on improving the conversion efficiency of the technology. However, the cost of installation and maintenance has limited the implementation and deployment of this technology for large-scale applications. Kinetic or vibratory

energy harvesting, on the other hand, can operate sufficiently in indoor conditions or environments without the presence of light or thermal gradient. Such advantages combined with the compatibility with standard microfabrication processes allow the technology to be integrated and implemented widely into mobile and wearable devices. The limitation of the technology is the low energy conversion efficiency at low-frequency excitations.

Given the advantages and limitations of each technology presented in this chapter, the research is to focus on kinetic or vibration energy harvesting due to its suitability to mobile and wearable applications. The challenges of this study are summarized and presented in Section 1.3 along with the objectives of the research.

1.3 Aims and objectives

The aim of the research is to investigate small-scale vibratory energy harvesters that can be integrated into mobile and wearable devices. Due to the nature of the vibrations induced in such applications, namely human body motion, several challenges have been arisen.

First, the low frequencies and small accelerations of the vibrations considered in these applications result in a small amount of available energy. To produce an adequate amount of energy to power a microelectronic device, small-scale linear energy harvesters must be designed with small resonant frequencies, which require soft springs and heavy masses. While fabricating a softer spring is possible, embedding a larger mass is extremely undesirable for the applications of mobile and wearable devices. Moreover, to ease the fabrication and integration into microelectronics, the technology selected to implement into the designs of these small-scale energy harvesters must be compatible with standard microfabrication processes. Hence, it is important to research the strengths and weaknesses of the structures and transduction mechanisms used in vibration energy harvesting to select the appropriate technology

that is suitable for mobile and wearable devices.

Second, the current modeling approach to analyze and optimize the performance of these small-scale energy harvesters is only applicable for some simple excitations, such as constant-speed rotations, while in practice, mechanical stimuli resemble sinusoidal vibrations. Consequently, a combination of finite element modeling (FEM) and numerical methods is the primary approach to analyze and optimize the performance of these devices. This approach is costly, time consuming and more importantly, limit the understanding of design trade-off involved. This leads to a need to develop a more practical analytical model considering sinusoidal vibrations to provide insights into the operating mechanisms of these small-scale energy harvesters.

Finally, the performance optimization of these practical devices is also a concern since most studies in the literature only focus on the absolute values without taking the limitations of material properties into account. Without a careful consideration, material failure or voltage breakdown may occur, and consequently, reduces the performance of these energy harvesters. Hence, it is necessary to include these effects into the calculation when designing and optimizing these structures.

Given such challenges, the objectives of the present research, therefore, includes the following

- Investigating the structures and transduction mechanisms of vibratory energy harvesting to select the most suitable technology with regard to the applications of mobile and wearable devices,
- Modeling small-scale energy harvesters under sinusoidal excitations - a standard form of mechanical vibrations resembling to ambient excitations in practice to provide insights into the operating mechanisms of these small-scale energy harvesters, and
- Optimizing the performance of small-scale vibratory generators using the proposed model combined with the practical limitation of material properties.

The next section outlines the content of the thesis which covers all the works to achieve the above goals.

1.4 Thesis overview

The thesis is organized as follows: Chapter 2 presents the state-of-the-art vibration energy harvesting methods including structural type and power transduction mechanisms. The strengths and weaknesses of each design and method are analyzed with regard to wearable applications. Chapter 3 provides an in-depth explanation of small-scale electret-based energy harvesting. The chapter also includes the derivation of characteristic equation of these small-scale generators and a simulation presented in the literature, that uses finite element modeling combined with numerical methods to computationally predict the output voltage and effective power of these generators. An example of employing the presented simulation to validate an analytical model of electret-based microgenerators under constant-speed rotations is also included at the end of the chapter. Chapter 4 is dedicated to present the formulation and validation of an analytical modeling for electret-based microgenerators under small sinusoidal translational vibrations - a more practical excitation type. The proposed analytical model is then employed to optimize the performance of the microgenerator with regard to the voltage breakdown phenomenon and material properties. In Chapter 5, the proposed model is extended further to take a general sinusoidal excitation into account. Finally, Chapter 6 summarizes the original contributions of this research in the field of vibration energy harvesting and present the future works.

Chapter 2

Small-scale vibration energy harvesting

This chapter presents a brief survey of different power conversion models and transduction mechanisms of vibration energy harvesting. The discussion of each approach and conversion technology covers a wide range of several practical factors, including usability, scalability, and manufacturability. In addition, the effectiveness of each power transduction method is also summarized and compared using those practical considerations in order to decide on the most suitable technology to be used for a targeted mobile or sensory wearable application.

Before delving into the approaches and technologies, it is important to explain the meaning of the word "micro" used throughout this thesis. In the state-of-the-art of vibration energy harvesting, the word "micro" mostly refers to different aspects of a system. Firstly, it describes the power level generated from small-scale energy harvesters, which is often in the range of tens of microwatts. Secondly, it is used to refer to the scale of the energy harvesters, which is in the order of micrometers. Although the overall dimension of practical micro energy harvesters can be in millimeter or centimeter range, the primary features of the transducers are often in micro scale or can be scaled down to micro scale. Finally, "micro" also refers to the fabrication method using standard fabrication techniques that are common in the semiconductor or micro-electro-mechanical-system (MEMS) industries. In addition, the term "small-scale energy harvesters" and "microgenerators" are used interchangeably.

2.1 Vibration to electricity conversion model

In order to convert mechanical stimuli to electricity, external vibrations are transmitted to inertially oscillate masses inside energy harvesters. The resultant relative displacements of those masses are then coupled with one of transduction mechanisms such as piezoelectrics, electromagnetics or electrostatics for electricity generation.

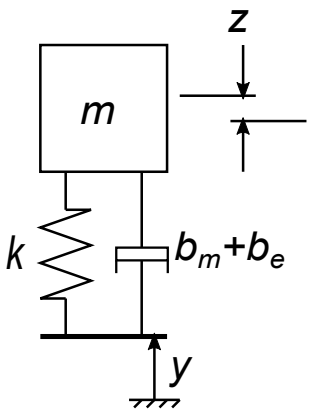

Figure 2.1. Schematic of a single-degree-of-freedom second-order spring-mass-damper system.

The most prolific energy harvester can be illustrated in Figure 2.1. The system consists of an inertial frame which transmits the vibration to a suspended mass m, via the spring k and the damper $(b_m + b_e)$. When an external excitation y is applied on the base of the structure, the mass m is relatively moved a distance z with regard to the base, which can drive the damper $(b_m + b_e)$ to generate electricity. The notation b_m represents the mechanical damping coefficient or losses occur during the inertial transmission, while b_e represents electrically induced damping or coupling coefficient that converts mechanical to electrical energy. Hence, it is desirable to minimize b_m and maximize b_e to achieve higher power conversion efficiency.

In general, a different number of mass m and different characteristics of k, b_m and b_e result in different dynamic behaviors of energy harvesting systems. For the ease of analysis, energy harvesting model is, therefore, divided into several categories as illustrated in Figure 2.2. This section presents a brief description of those energy

harvesting system types and analyzes their strengths and weaknesses with regard to the application of wearable devices.

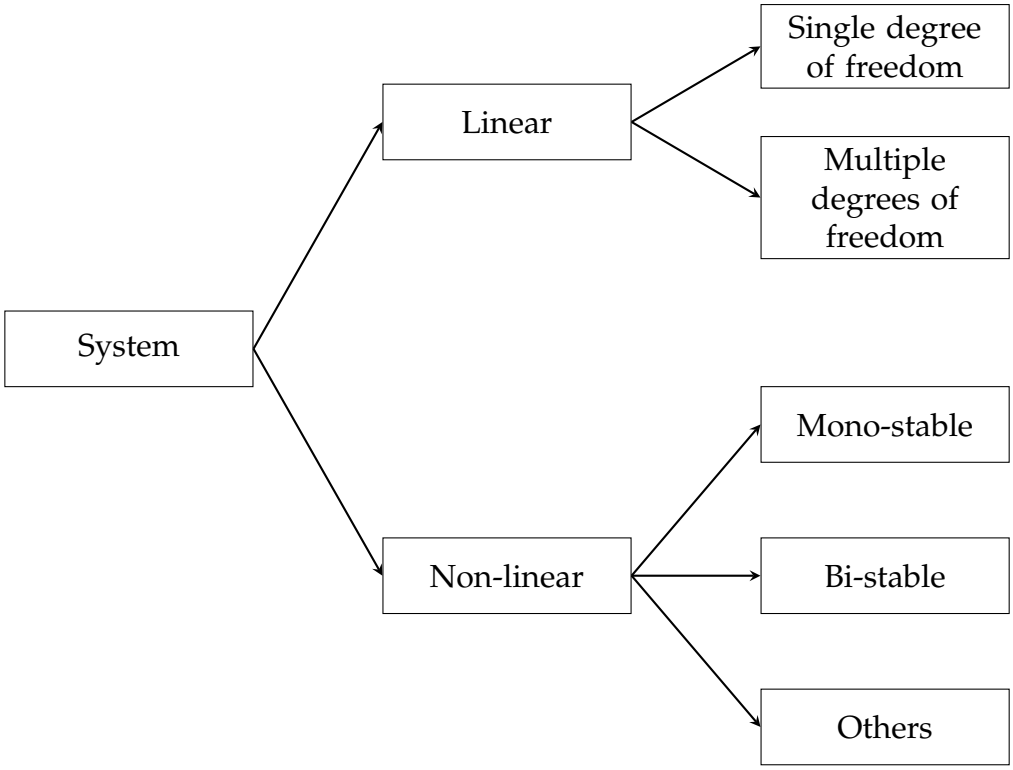

Figure 2.2. Classification diagram of different energy harvesting systems.

2.1.1 Linear system - Single degree of freedom

Single-degree-of-freedom (SDOF) second-order spring-mass-damper system is the most typical model used for vibration energy harvesting. The model which is firstly described by Williams & Yates (1996) consists of only one mass m with a linear spring k and linear dampers b_m and b_e. Under an external excitation $y(t)$, the mass m is inertially moved a distance $z(t)$ characterized as

$$m\ddot{z}(t) + (b_m + b_e)\dot{z}(t) + kz(t) = -m\ddot{y}(t). \tag{2.1}$$

The damper coefficient in equation (2.1) is presented as a sum of the mechanical and electrical damping b_m and b_e, respectively. For simplicity, b_m and b_e are assu-

med to be constant. Nevertheless, several important conclusions can be made when analyzing this simplified model.

Given such assumptions, the generated power at the output of energy harvesters is equal to the power dissipated by the electrically induced damping b_e, which can be calculated as

$$P_e = \frac{1}{2} b_e \dot{z}^2 \tag{2.2}$$

When the external excitation is a sinusoidal function $y = Y \sin \omega t$, the output power generated can be found as

$$P = \frac{m \frac{\zeta_e}{\omega_n} \left(\frac{\omega}{\omega_n}\right)^2 A^2}{\left[1 - \left(\frac{\omega}{\omega_n}\right)^2\right]^2 + \left(2\zeta \frac{\omega}{\omega_n}\right)^2}, \tag{2.3}$$

where

$\omega_n = \sqrt{\frac{k}{m}}$ is the natural frequency of the system

$\zeta_e = 2mb_e\omega_n$ is the electrically induced damping ratio

$\zeta = \zeta_m + \zeta_e$ is the composite damping ratio

$A = \omega^2 Y$ is the acceleration magnitude of the input vibration.

Figure 2.3 shows the normalized output power given in equation (2.3) as a function of normalized frequency. The peak of the output power generated from the generator occurs at the resonance where the forcing frequency ω is equal to the system natural frequency ω_n. As ω is shifted away from ω_n, the output power is reduced dramatically. Another observation is the wider shape of the output power at a higher damping ratio ζ, which can adapt well to various excitation frequencies. However, the downside of a large ζ is the reduction of the peak power.

In many cases, the spectrum of the targeted vibration sources is known and therefore, the generator can be designed to resonate at the input vibration frequency. In

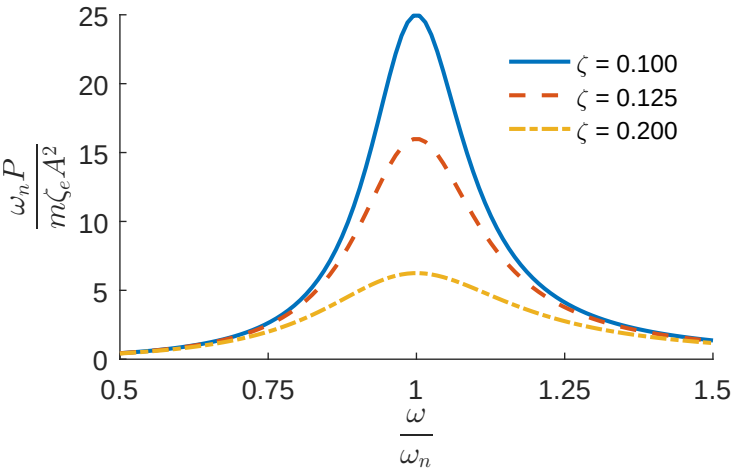

Figure 2.3. Output power of vibration energy harvesters is a function of input frequency.

this case, the expression of the output power is simplified to

$$P_{\max} = \frac{m\zeta_e A^2}{4\omega\zeta^2}. \tag{2.4}$$

Another important parameter is the bandwidth which is used to determine the sharpness of the output power in the frequency domain. Bandwidth is defined as an increment $\Delta\omega$ measured at "half-power point" ($P = P_{\max}/2$). Given this definition, one can use equation (2.3) to derive the correlation between the system bandwidth and the damping ratio, and express as

$$\frac{\Delta\omega}{\omega_n} = 2\zeta. \tag{2.5}$$

Several important conclusions of SDOF systems can be made from the expressions given in equations (2.3), (2.4) and (2.5)

- Maximum output power is obtained at resonance. Therefore, it is critical to design a SDOF generator in which the natural frequency closely matches the fundamental vibration frequency of external vibrations.

- The peak output power is directly proportional to the square of input accelera-

tion amplitude. In other words, either a higher forcing frequency or vibration amplitude results in a higher output power. The downside of this characteristic is a low output power when scavenging low-acceleration vibrations.

- The output power is optimized when ζ_m is as small as possible, while ζ_e equals to ζ_m. The trade-off of small damping ratios is the narrow bandwidth, in which a slight shift from the resonant frequency can dramatically decrease the power generated from the generator. Since ζ_e relates to coupling coefficient which is generally a function of circuit parameters, the appropriate value of ζ_e needs to be carefully designed to balance between the peak power and the bandwidth of the generator.

2.1.2 Linear system - Multiple degree of freedom

The major weakness of SDOF systems is narrow bandwidth which limits the amount of energy generated in the real-world environment where the driving frequency is varied. One of the approaches to overcome this limitation is to employ multiple degrees of freedom (MDOF) systems which are illustrated in Figure 2.4 in order to

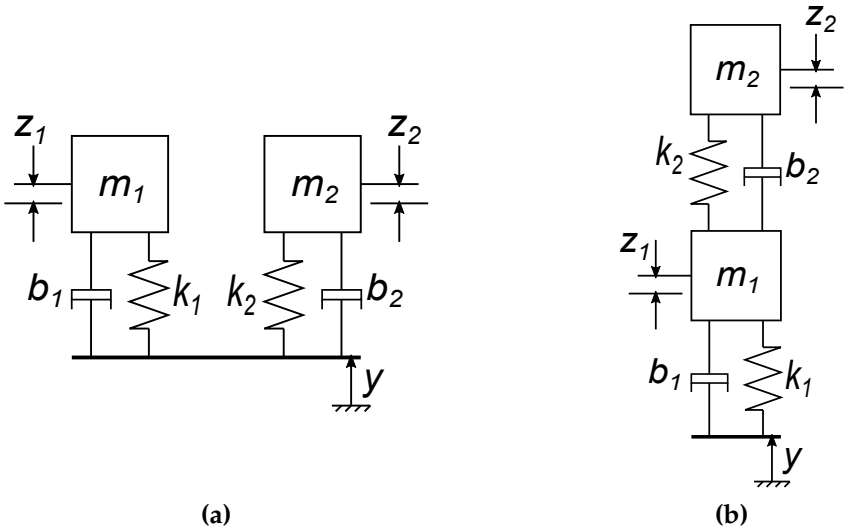

Figure 2.4. Two configurations of two degrees of freedom system (a) an array of two SDOFs and (b) composite two degrees of freedom system.

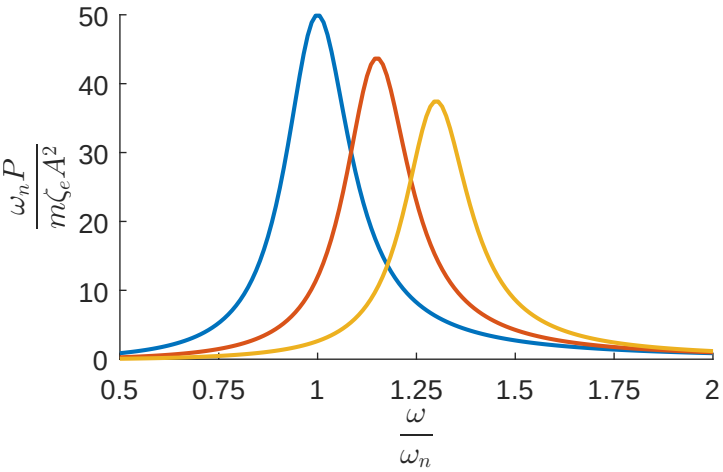

Figure 2.5. Output power of an arrayed type MDOF system is the sum of performance of each SDOF system. Different colors illustrated the output power of different SDOF elements within the whole MDOF system.

resonate at many natural frequencies.

One of the simplest forms of a MDOF system is an array of several SDOF systems (Shahruz 2006, Xue et al. 2008, Ferrari et al. 2008, Liu et al. 2008, Sari et al. 2008) as shown in Figure 2.4a. In this case, each SDOF structure is operated independently and therefore, the superposition principle can be applied to analyze the system using the result derived in Subsection 2.1.1. The output power generated from this type of generators is a sum of all elementary devices in the array, which is illustrated in Figure 2.5.

Another popular structure of MDOF is the composite system (Wu et al. 2013) shown in Figure 2.4b. The equation of motion expressed in (2.6) is more complicated than the arrayed type due to the sophisticated relation of motions between masses m_1 and m_2, given by

$$\begin{cases} m_1\ddot{z}_1 + (b_1+b_2)\dot{z}_1 + (k_1+k_2)z_1 - b_2\dot{z}_2 - k_2 z_2 &= (b_1-b_2)\dot{y} + (k_1-k_2)y \\ m_2\ddot{z}_2 + b_2\dot{z}_2 + k_2 z_2 - b_2\dot{z}_1 - k_2 z_1 &= b_2\dot{y} + k_2 y. \end{cases} \tag{2.6}$$

For convenience, equation (2.6) can be rewritten in a state-space form using vectors

and matrices

$$\begin{bmatrix} 1 & 0 & 0 & 0 \\ 0 & m_1 & 0 & 0 \\ 0 & 0 & 1 & 0 \\ 0 & 0 & 0 & m_2 \end{bmatrix} \begin{bmatrix} \dot{z}_1 \\ \ddot{z}_1 \\ \dot{z}_2 \\ \ddot{z}_2 \end{bmatrix} + \begin{bmatrix} 0 & -1 & 0 & 0 \\ k_1+k_2 & b_1+b_2 & -k_2 & -b_2 \\ 0 & 0 & 0 & -1 \\ -k_2 & -b_2 & k_2 & b_2 \end{bmatrix} \begin{bmatrix} z_1 \\ \dot{z}_1 \\ z_2 \\ \dot{z}_2 \end{bmatrix} = \begin{bmatrix} 0 \\ (k_1-k_2)y + (b_1-b_2)\dot{y} \\ 0 \\ k_2 y + b_2 \dot{y} \end{bmatrix} \tag{2.7}$$

Here, it is important to determine the natural frequencies and shape modes of the system. This can be done by zeroing all terms related to damping coefficients b_1 and b_2 and the external vibration y. Under this condition, the system is simplified to

$$\mathbf{M_n}\ddot{\mathbf{x}}_\mathbf{n} + \mathbf{K_n}\mathbf{x_n} = 0, \tag{2.8}$$

where

$$\mathbf{M_n} = \begin{bmatrix} m_1 & 0 \\ 0 & m_2 \end{bmatrix}, \quad \mathbf{x_n} = \begin{bmatrix} z_1 \\ z_2 \end{bmatrix}, \text{ and } \quad \mathbf{K_n} = \begin{bmatrix} k_1+k_2 & -k_2 \\ -k_2 & k_2 \end{bmatrix} \tag{2.9}$$

Since we are interested in finding harmonic solutions for $\mathbf{x_n}$, we can simply assume that the solution has the form $X \sin \omega_n t$, and substitute into equation (2.8)

$$-\mathbf{M_n}\mathbf{X}\omega_n^2 \sin \omega_n t + \mathbf{K_n}\mathbf{X} \sin \omega_n t = 0 \quad \rightarrow \mathbf{K_n}\mathbf{X} = \omega_n^2 \mathbf{M_n}\mathbf{X}. \tag{2.10}$$

According to linear algebra, ω_n and $\mathbf{X}$ are the eigenvalues and eigenvectors of equation (2.8). Therefore, it is important to note that the natural frequencies of a composite MDOF system are different from the conventional formula $\sqrt{k/m}$ of an SDOF system. Figure 2.6 illustrates the displacement of the two masses of a composite-configured two-degree-of-freedom generator. The additional mass-spring-damper introduce another natural frequency and vibration mode, resulting in additional displacement peak. If an appropriate value of m_2 is selected, the generator can harvest energy at a broader range of frequency, compared with SDOF systems.

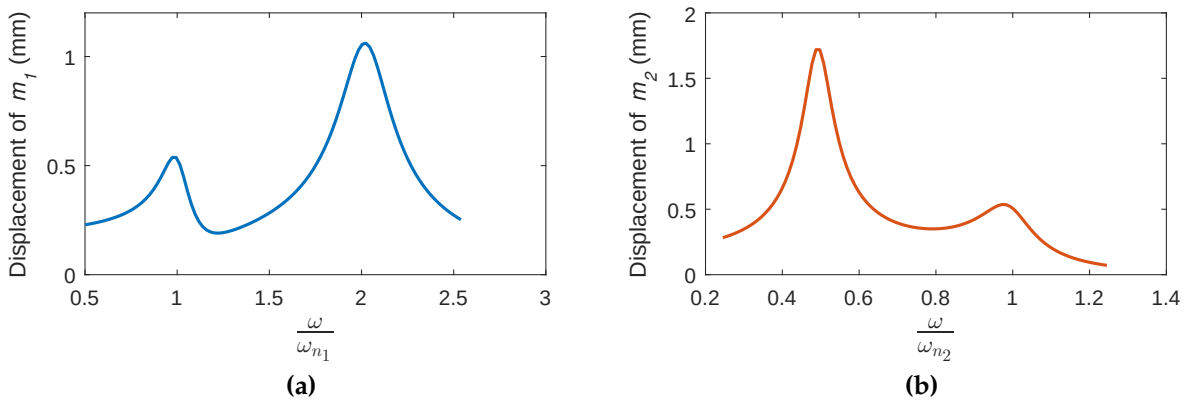

Figure 2.6. Response of a composite-configured two degrees-of-freedom system in the frequency domain (a) displacement of mass m_1, and (b) displacement of mass m_2.

In spite of a wider bandwidth response, the severe trade-off of MDOF generators is the increasing of device dimensions due to the introduction of additional masses, dampers, and springs. Consequently, the generators become bulky and thus, difficult to integrate and implement into microelectronic devices. Another disadvantage of MDOF structures is the complexity of management circuits which are used to rectify, condition and combine the output voltage signals with different phases generated from several masses. Such challenges limit the usage of MDOF systems, making the structure unsuitable for mobile and wearable applications.

2.1.3 Nonlinear generators

Nonlinear vibration energy harvesters or generators are designed to overcome the weakness of both SDOF and MDOF structures by broadening the bandwidth without significantly increasing the generator sizes. The operation mechanism of a nonlinear generator is similar to a SDOF structure, except the nonlinear effect of the springs used in the structures is taken into account. The equation of motion for such structure can, therefore, be written in the following general form

$$m\ddot{z} + b\dot{z} + \frac{dU(z)}{dz} = -m\ddot{y}, \tag{2.11}$$

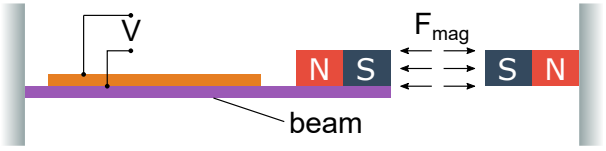

Figure 2.7. An example of a nonlinear energy harvester in which a pair of permanent magnets are employed to create a nonlinear spring.

where the function $U(z)$ represents the potential energy of the mechanical system.

The shape of the potential function depends on the nonlinearity present in the generator. One of the most popular nonlinear structures heavily studied in the literature is Duffing oscillator (Beeby et al. 2007, McInnes et al. 2008, Mann & Sims 2009, Cottone et al. 2009, Erturk et al. 2009, Harne & Wang 2013, 2016), in which the potential function is defined as

$$U(z) = \frac{1}{2}k_1 z^2 + \frac{1}{4}k_2 z^4, \tag{2.12}$$

where k_1 and k_2 are linear and nonlinear stiffness coefficients, respectively.

An example of this nonlinear generator is depicted in Figure 2.7, where the generator consists of a piezoelectric cantilever beam and a pair of permanent magnets. When the beam is deformed, the distance between the two magnets changes, resulting in a nonlinear repulsive force and hence, can be considered as a nonlinear spring.

Given the Duffing's potential function, equation (2.11) can, therefore, be rewritten as

$$\ddot{z} + \delta\dot{z} + \alpha z + \beta z^3 = -A\sin\omega t, \tag{2.13}$$

where

$$\delta = \frac{b}{m}, \qquad \alpha = \frac{k_1}{m} = \omega_n^2 \qquad \text{and} \qquad \beta = \frac{k_2}{m}.$$

Figure 2.8a illustrates the displacement of a nonlinear generator with different nonlinear coefficients of the spring stiffness. Depending on the linearity of the spring

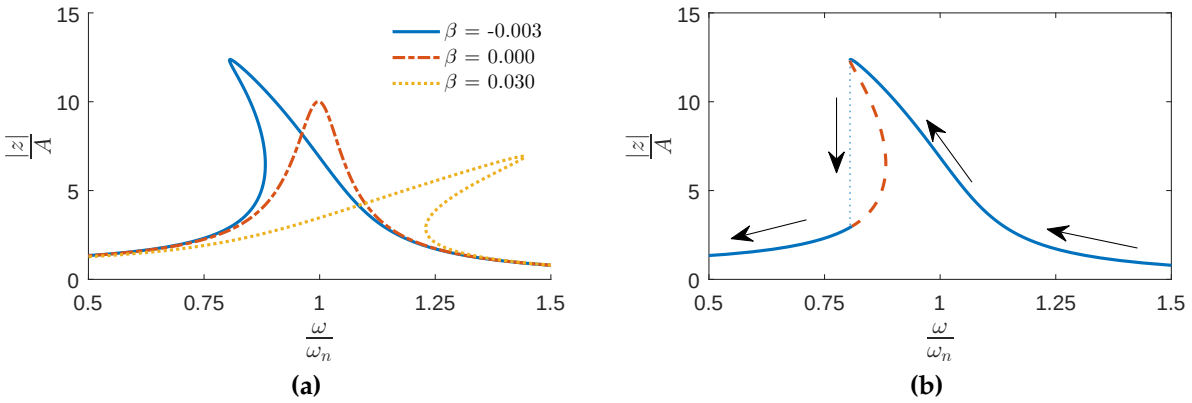

Figure 2.8. (a) Frequency response of nonlinear microgenerator displacement with $\delta = 0.1$ and $\alpha = 1$ is plotted with various values of nonlinear spring stiffness. The bend to the left corresponds to a softening nonlinearity, while the bend to the right indicates a hardening nonlinearity. (b) The response of a nonlinear structure starts from a high initial frequency and sweeps slowly as illustrated as arrows to reach to the peak displacement. When the frequency crosses the peak, there is a jump in which the response drops from the peak to the branch on the left. The red dashed line illustrates the unstable response of the system.

stiffness, the generated power can be bent to the left of the frequency axis, corresponding to a softening case, or to the right, corresponding to a hardening spring. As a result, a broader bandwidth can be obtained to harvest energy from a wide range of excited frequencies.

One severe weakness of nonlinear generators is the requirement of certain types of frequency sweeping excitations. For example, to achieve the maximum output power, corresponding to the maximum displacement as shown in Figure 2.8b, the forcing frequency is initially set at a high value and slowly decreased to the desirable point, so that the response of the generator can follow the direction of the arrows to reach to the peak displacement. Too much reduction in the input frequency can result in a "jump" where the maximum displacement suddenly falls off to the lower values as illustrated as the dotted vertical line in Figure 2.8b.

Another popular type of nonlinear generators can be realized as eccentric mass or pendulum-like structures, such as the electrodynamic transducer shown in Figure 2.9, or the electrostatic generator presented in (Nakano et al. 2015). These devices can

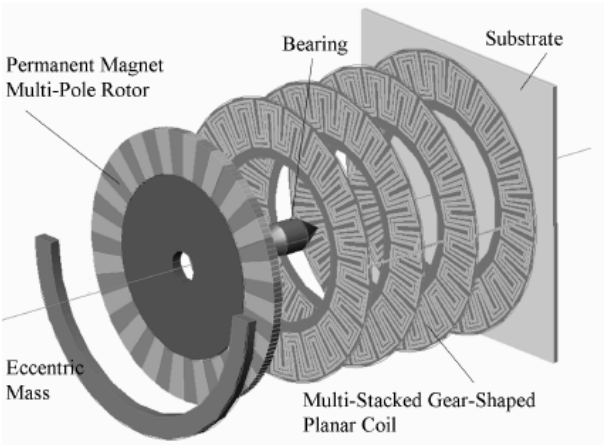

Figure 2.9. An example of non-linear microgenerators employing eccentric mass or pendulum like structure which not only has wide bandwidth, but also be able to harvest energy at low frequency using electromagnetic power transduction mechanism (Romero et al. 2009).

harvest kinetic energy at low-frequency excitations (less than 5 Hz), although the capability of wide bandwidth has yet been demonstrated. In general, an eccentric mass or a pendulum under a harmonic driving torque can be characterized as

$$\ddot{\theta} + \frac{b}{I}\dot{\theta} + \frac{mgl}{I}\sin\theta = A\sin\omega t, \tag{2.14}$$

where θ, I, m and l are respectively the angular amplitude, inertial moment, mass and length of the pendulum, b is damping coefficient, g is the gravitational acceleration, A is the amplitude of the angular acceleration and ω is the angular frequency of the excitation.

For simplicity, only small amplitudes of θ are examined. A higher value of θ results in a much more sophisticated analysis which is beyond the scope of this thesis. Given the considered assumption, the nonlinear term in equation (2.14) can be linearized using the approximation $\sin\theta \approx \theta$. The pendulum can, therefore, be approximated to an SDOF spring-mass-damper system. Otherwise, Taylor's series expansion can be employed to take the effect of nonlinearity into account

$$\sin\theta = \theta - \frac{\theta^3}{3!} + \frac{\theta^5}{5!} - \dots. \tag{2.15}$$

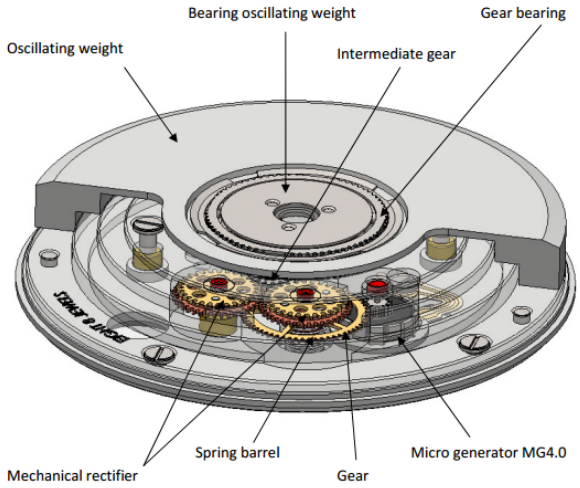

Figure 2.10. A nonlinear microgenerator from Kinetron employs eccentric mass to harvest kinetic energy.

Thus, if the first two terms of the Taylor's series expansion are considered, the pendulum can be analyzed as a Duffing oscillator with $k_1 = 1$ and $k_2 = -1/6$.

The two well-known commercial products based on eccentric mass or pendulum-like structure are Seiko Kinetic Watch and Kinetron Watch as shown in Figure 2.10. With a size of 26.4 mm diameter and a thickness of 4.3 mm, the Kinetron microgenerator is reported to generate 600 mJ per day which yields a significant power density of 6.3 $\mu W/cm^3$, assuming being worn 12 hours per day.

Given the ability of operating at a low frequency and broad bandwidth, nonlinear systems, and in particular the pendulum-like or eccentric-mass structures, are more favorable to implement in wearable applications.

In Subsection 2.1.4, the strengths and weaknesses of each system types are summarized from the application point of view to select the most suitable method to analyze further.

2.1.4 Structural type comparison of vibration energy harvesters

Table 2.1 summarizes the advantages and disadvantages of the three commonly used models of microgenerators in the literature. While the linear systems, including SDOF

Table 2.1. Comparison of three common structural models used to convert mechanical vibrations to electricity.

	SDOF	MDOF	Nonlinear system
Low frequency	Small natural frequencies require heavier masses and softer springs. While elastic springs are able to be fabricated, large masses increase the dimensions of the structure, resulting in bulky devices.		In general, the systems can harvest energy at low-frequency excitations; however, certain type of excitation such as slowly sweeping down as shown in Figure 2.8b may require.
Bandwidth	Small in general; increasing damping ratio can widen bandwidth, but the trade-off is the reduction of power generated at the output	Wide bandwidth, however, accompanied by an increased size or weight, and consequently, the overall power density may be sacrificed	Broad bandwidth can be obtained when the system nonlinearity is sufficiently strong. The trade-off is a complicated type of excitations required.
Interface circuit	Simple due to only one output signal	Sophisticated to avoid the cancellation of phase difference between several output voltages	May accompany with some active controllers or actuators, which results in a net loss of the energy harvested.

and MDOF, are simple to be fabricated and easy to be analyzed and optimized, their performances heavily depend on natural frequencies. As a result, the implementation of these structures is quite limited, especially at low-frequency excitations due to the requirement of larger masses and softer springs. The nonlinear systems, on the other hand, can provide a better performance when operating under low-frequency vibrations. The trade-off, however, is the complexity of designing and analyzing to optimize the performance under targeted applications.

Given the advantages of scavenging energy at low frequencies while maintaining a compact size, non-linear systems are, therefore, selected as the main focus of this research. In the following subsection, the principle of a few common power trans-

duction mechanisms when designing a microgenerator are discuss in details.

2.2 Transduction mechanisms

This section presents a brief overview of three most widely-used power transduction mechanisms, converting mechanical vibrations into electricity. A comparison of performance effectiveness of various prototypes using different transduction mechanisms is also carried out to explore the applicability of each mechanism in mobile and wearable applications.

2.2.1 Piezoelectric power conversion

Piezoelectric effect is the most mature transduction mechanism in vibration energy harvesting, in which a piezoelectric material generates an electric charge when it is subjected to a mechanical stress. This is called the direct effect. The other effect is that the material undergoes deformation when an external electric field is applied. Hence, a piezoelectric material can be used as a sensor and transducer by employing the direct effect, or actuators when reserved effect is used. The coupled electromechanical behavior of piezoelectric materials can be presented by the two linearized constitutive equations

$$\delta = \frac{\sigma}{Y} + Ed \tag{2.16}$$

$$D = \varepsilon E + \sigma d, \tag{2.17}$$

where δ is mechanical strain induced due to the deformation of the piezoelectric material, σ is the mechanical stress, Y, E and ε are respectively Young's modulus, electric field and dielectric constant of the piezoelectric material, d is piezoelectric strain coefficient and D is electric displacement generated within the piezoelectric material.

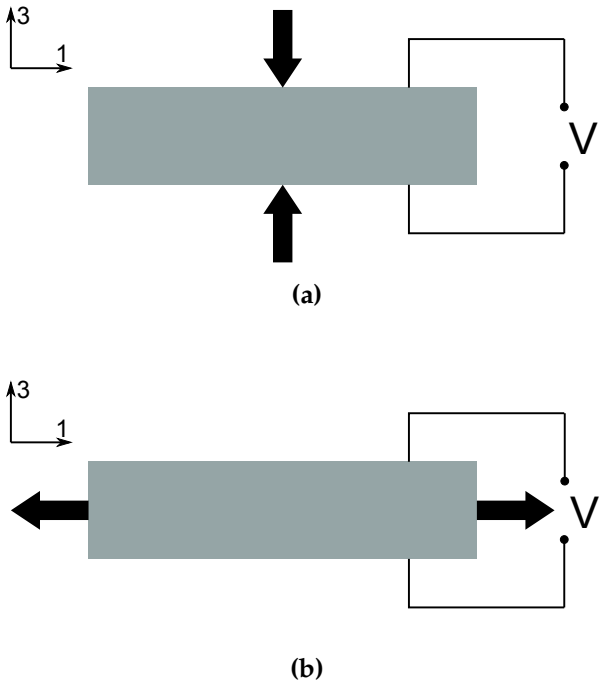

Figure 2.11. Two common operation modes of piezoelectric material (a) mode 33 and (b) mode 31.

Without the effect of the electric field E, equation (2.16) simply becomes Hook's law which correlates the mechanical stress and strain. Similarly, without the coupling term σd, equation (2.17) is simply a form of electric displacement of a linear, homogeneous and isotropic dielectric. Hence, the electric field of piezoelectric material modifies the material mechanics, while the stress in the material modifies its dielectric properties.

One important parameter of piezoelectric materials is piezoelectric coefficient, d, which is, in general, a 3-by-6 tensor or matrix. However, only 3 coefficients are often used, while the rest are zero. The two most common coefficients used in energy harvesting are d_{31} and d_{33} which correspond to the two operation modes shown in Figure 2.11. The coefficient d_{33} often refers as the longitudinal coefficient which describes the electric polarization generated in the same direction of the applied stress. In contrast, the coefficient d_{31} is the transverse coefficient which describes the electric polarization generated in the direction perpendicular to the direction of the applied stress.

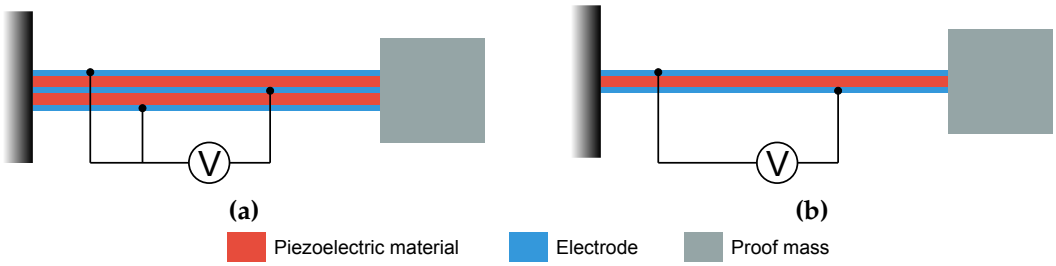

Figure 2.12. Two common configurations of piezoelectric cantilever beam (a) bimorph and (b) unimorph.

The most prolific piezoelectric microgenerator can be realized as a cantilever beam operating in mode 31, as shown in Figure 2.11. When the beam is bent downward, the layer on the top surface is stretched, while the layer at the bottom surface is compressed. In the other words, the large deflection in the vertical direction, corresponding to the direction 3, is transformed into a small deformation in the horizontal direction, corresponding to the direction 1. The same principle is applied when the beam is bent upward. Hence, designing such piezoelectric cantilever beam can increase the compliance, up-scale the strain induced and lower the resonant frequency. The proof mass added at the end of the beam further increases the compliance of the system, resulting in an even lower resonant frequency. Given these advantages, operating in mode 31 is more preferred in energy harvesting application, despite the superior value of d_{33} compared with d_{31}.

Another consideration when designing piezoelectric generators is the configuration of piezoelectric materials embedded in the structures shown in Figure 2.12. A bimorph-configured cantilever beam shown in Figure 2.12a consists of several layers of piezoelectric materials with their electrodes connected either in serial or parallel, resulting in a higher current or voltage at the output, respectively. However, at micro scales, making thin films and assembling bimorph structures are less manufacturable with existing standard microfabrication processes. As a result, most recent piezoelectric MEMS-based structures are in unimorph-configuration (Priya et al. 2017).

Piezoelectric materials can be categorized into piezoceramics and piezopolymers.

Table 2.2. Specification of some common piezoelectric materials.

Coefficient	PZT-5H	PZT-8	PVDF	Parylene-C
d_{31} (10^{-12}m/V)	-274	-97	18 to 24	-
d_{32} (10^{-12}m/V)	-274	-97	2.5 to 3	-
d_{33} (10^{-12}m/V)	593	225	-33	2.0
Dielectric constant	3400	1000	7.5	3.15
Dielectric breakdown (kV/mm)	2		10	0.142
Density (g/cm^3)	7.5	7.6	1.8	1.29

Piezoceramic materials, such as PZT-5H and PZT-8, are widely used in the literature of vibration energy harvesting due to large electro-mechanical coupling coefficients, resulting in a higher power generated at the device output. However, the materials are brittle and consequently, limit the usage to prototype general-shape generators. In addition, piezoceramic materials are incompatible with standard microfabrication processes such as MEMS, making the materials less manufacturable to implement into micro-scale applications (Kim et al. 2011). Recently, polymer-based materials, such as polyvinylidene fluoride (PVDF) or Parylene-C, have been widely used to designed and prototyped vibration microgenerators due to the material flexibility compared with piezoceramics. The trade-off when using piezopolymer materials is the low electromechanical coupling coefficients compared with piezoceramic materials. As shown in Table 2.2, the performance of PVDF is about 5 to 20 times less than PZT-based materials. Hence, depending on the applications and operating conditions, one can select suitable materials to design and fabricate piezoelectric generators.

Piezoelectric microgenerators can provide high voltage and low current. In general, piezoelectric microgenerators can produce a few volts to several volts. Hence, one notable advantage of piezoelectric microgenerators is the direct generation of the appropriate output voltage which eases the rectification and conditioning processes. In addition, Roundy & Wright (2004) report that piezoelectric microgenerators have the highest power density compared with other transducers such as electromagnetics and electrostatics. That is why the transduction mechanism is more favorable to be

Table 2.3. Comparison of recent small scale piezoelectric generators.

Reference	Active volume (cm^3)	Acceleration (m/s^2)	Frequency (Hz)	Power (μW)	Power density ($\mu W/cm^3$)
Roundy et al. (2003*b*)	4.8	2.25	40	1700	354.2
Roundy & Wright (2004)	1	2.5	120	80	80
Roundy & Wright (2004)	1	2.5	120	365	365
Roundy & Wright (2004)	1	2.5	120	207	207
Tanaka et al. (2005)	9	0.987	50	180	20
Ng & Liao (2005)	0.2	72.7	100	35.5	177.5
Lee et al. (2009)	0.452	24.5	255.9	2.765	6.12
Durou et al. (2010)	0.464	0.98	77	3.2	6.9
Durou et al. (2010)	0.464	1.96	76	13.9	30.0
Morimoto et al. (2010)	4.884	5	126	5.3	1.1
Aktakka et al. (2011)	5.6E-3	134	92.1	7.5	1339
Aktakka et al. (2011)	11	134	92.1	11.5	1046
Defosseux et al. (2012)	2.8E-3	2.7	214	0.63	225
Liu et al. (2012)	6.27E-5	7.85	25	0.01	159.5
Ibrahim & Salehian (2015)	4.74	2.94	15-27	22	4.64
Ibrahim & Salehian (2015)	1.66	2.94	21	52	31.33

implemented into several designs for micro power generation. In addition, piezoelectric microgenerators do not require any external priming sources to initiate the conversion process, making the technology suitable for autonomous operation.

Given such advantages, piezoelectrics has been the most popular transduction mechanism used in small-scale vibration energy harvesting. Table 2.3 summarizes several studies of small-scale piezoelectric generators with their input accelerations and volumetric power densities published in the literature.

The disadvantage using piezoelectric materials in vibration energy harvesting is the difficulty to implement the high performance or piezoceramic materials into micro scale applications. Although using thin piezopolymer film is possible, the coupling coefficient is dramatically reduced, resulting in a significant reduction of performance. Another disadvantage of piezoelectric microgenerators is that the structures often resonate at high resonant frequencies, mostly in the order of 100 Hz (Zhu et al. 2009). Recent research is focusing on softening the stiffness of piezoelectric cantilever

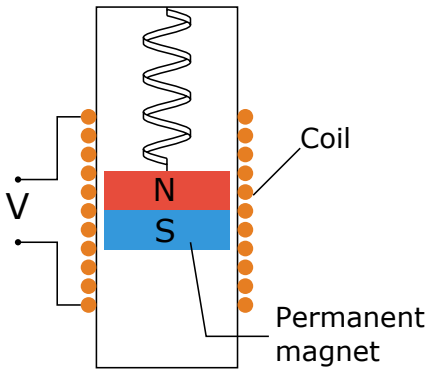

Figure 2.13. A simple electromagnetic transducer.

beams to work at lower frequencies, while widening the operating bandwidth. One of the most common approaches is to install additional permanent magnets similar to Figure 2.7 to increase the nonlinearity of the beam stiffness which is presented in Subsection 2.1.3. Research in this field is still active to look for new materials with high electromechanical coupling as well as design non-resonant structures to harvest energy at low-frequency excitations (Priya et al. 2017).

2.2.2 Electromagnetic power conversion

The principle of electromagnetic power conversion is based on Faraday's law of induction where electricity is generated from the relative motion of an electrical conductor in a magnetic field. Figure 2.13 illustrates a typical setup of an electromagnetic transducer in which the conductor is wound several turns into a coil and moves relatively in the magnetic field generated by the permanent magnets.

The voltage of the conductor is determined using Faraday's law of induction, which is presented as

$$\mathcal{E} = -\frac{d\Phi_B}{dt}, \tag{2.18}$$

where $\mathcal{E}$ is the induce electromotive force (EMF) and Φ_B is the magnetic flux.

For a tightly wound coil of wire moving in the perpendicular direction of a con-

stant magnetic field, the maximum open circuit voltage is simplified to

$$V_{oc} = NBl\frac{dz}{dt}, \tag{2.19}$$

where N and l are respectively the number of turns and the total length of the coil, B is the strength of the constant magnetic field, and z is the distance that the coil travels in the magnetic field.

Given equation (2.19), the output voltage of the electromagnetic generator is directly proportional to the number of turn of the coil, the strength of magnetic field and the relative velocity of the coil and the magnetic field. Hence, to increase further the output voltage, the transducer must be designed with a higher number of turns of the coil and a larger strength of the magnetic field.

To obtain a higher density of coil turns in a compact electromagnetic generator, a fine conductive wire is desirable. However, as shown in Table 2.4, the finer the wire, the greater its resistance per unit length. Typically, each type of copper wire is insulated by a different thin polymer film, which offers a different degree of operating temperature range, solderability, and solvent resistance. The choice of wire type used in the coil is, therefore, important and mostly depends on applications.

While increasing the density of coil turns is limited by the physical properties of wire and the generator size, increasing the strength of the magnetic field heavily depends on the permanent magnets used in the device. Table 2.5 presents a list of common materials which are widely used to fabricate MEMS-based permanent magnets. A useful figure of merit to compare magnetic materials is the maximum energy product, BH_{max}, calculated from a materials magnetic hysteresis loop. Another considered factor is the Curie temperature, which is the maximum operating temperature the material can withstand before being demagnetized. In addition, corrosion resistance is also another essential factor considered when selecting permanent magnet materials to reduce the risk of failure. The choice of the materials used, therefore,

Table 2.4. Properties of fine copper wire from American Wire Gauge standard.

Copper diameter (μm)	**Wire diameter (including insulation)** (μm)	**Resistance** (Ω/m)
10	10.612.9	0.22
11	11.714.1	0.18
12.5	13.216.5	0.14
14	14.717.8	0.11
15.8	16.519	0.09
17.8	18.521.6	0.07
20	21.625.4	0.056
22	24.127.8	0.044
25	26.730.5	0.035
28	29.733	0.028
31.5	32.838.1	0.022
35.6	36.843.2	0.017

depends on the applications. For miniaturization, $Nd_2Fe_{14}B$ is the most commonly used material in small-scale inertial electromagnetic generators due to their high performance of the magnetic field produced and broad operating temperature ranges. These magnets also have a high coercive force and therefore, the vibration of these miniature generator will not de-pole the magnets (Beeby et al. 2009).

Although macro-scale electromagnetic generators have been the primary source that produce electricity to power facility grid for years, the performance of the transduction mechanism at small scale is dramatically reduced as shown in Table 2.6. At small scale, the magnetic field generated by miniature permanent magnets is much weaker and the number of coil turns is much smaller. Consequently, the output voltage is extremely low, most likely less than 200 mV. This low output voltage presents a serious problem which complicates the rectification and conditioning processes. In order to rectify the voltage, transformers with conversion ratios in the order of 100 are necessary to bring up the range to a few volts. Such transformers are problematic to implement within a small volume device commonly needed in mobile and wearable applications. One way to overcome this is to reduce the proof mass of the

Table 2.5. Properties of some common materials to make permanent magnets used in MEMS applications presented in (Arnold & Wang 2009).

Material	**Category**	**Bulk manufacturing method**	**Intrinsic coercivity** H_{ci} (kA/m)	**Remanence** B_r (T)	**Energy product** BH_{max} (kJ/m^3)	**Curie temp.** (^{o}C)	**Max. operating temp.** (^{o}C)	**Corrosion resistance**
$Mo{\cdot}6Fe_2O_3$	Ferrite	Powders	200-380	0.2-0.4	8-30	450-470	200-300	Excellent
Al-Ni-Co	Metal alloy	Case, powders	40-170	0.7-1.3	11-72	810-860	450-550	Very good
CoPt-$L1_0$	Metal alloy	Cast, powders	360	-	75	840	-	Very good
FePt-$L1_0$	Metal alloy	Cast, powders	390	-	160	750	-	Very good
$SmCo_5$	Rare earth	Powders	1300-2400	0.83-0.95	130-180	685-750	250-300	Moderate
SM_2Co_{17}	Rare earth	Powders	560-2100	1.0-1.2	190-240	750-970	300-350	Moderate
$Nd_2Fe_{14}B$	Rare earth	Powders	880-3300	1.0-1.4	190-400	310	125-150	Poor

Table 2.6. Comparison of recent small scale electromagnetic generators.

Reference	Active volume (cm^3)	Acceleration (m/s^2)	Frequency (Hz)	Power (μW)	Power density ($\mu W/cm^3$)
Li et al. (2000)	1.24	16.17	64	10	8.06
Ching et al. (2001)	1	28.42	60	680	680
Lee et al. (2003)	7.3	42.78	85	830	114
Beeby et al. (2007)	0.15	0.6	52	46	306.67
Huang et al. (2007)	0.04	19.7	100	1.4	35
Ayala et al. (2009)	1.12	0.8	45	200	178.57
Chang et al. (2009)	0.96	24.7	25	400	416.67
Wang & Arnold (2009)	0.014	10	530	2.3E-5	1.64E-3
Oliver & Priya (2010)	68.64	6.87	147.5	28E3	408
Sari et al. (2010)	0.148	220	113	6.6E-3	0.045
Jiang et al. (2011)	0.1	11.7	115	120	1200
Dai et al. (2012)	0.108	8	190	4.9E-3	0.045
Tao et al. (2012)	0.02	10	365	1.6E-5	8E-4
Liu et al. (2013)	0.35	10	840	5.5E-3	15.7E-3
Perpetuum (2013)	398	0.5	25-120	4.2E3	10.55
Perpetuum (2013)	398	0.25	25-120	1.2E3	3
Zhang & Kim (2015)	0.2	64	400	5.5E-4	2.5E-3
Tao et al. (2016)	0.29	1.2	391	9.6E-4	3.3E-3

electromagnetic microgenerators; however, the side effect is a severe reduction of the system potential, resulting in an even smaller output voltage and power.

2.2.3 Electrostatic power conversion

Electrostatic generation can be realized as a capacitive system which consists of two electrically conductive plates separated by a dielectric media. The relative motion between the two plates changes the capacitance of the system, resulting in electricity generation. An example of electrostatic generation is a planar capacitor with the capacitance defined as

$$C = \frac{\varepsilon_0 \varepsilon A}{d}, \tag{2.20}$$

where ε_0 is the permittivity of free space, ε is the relative permittivity of the dielectric or also known as dielectric constant, A and d are the overlapping and distance

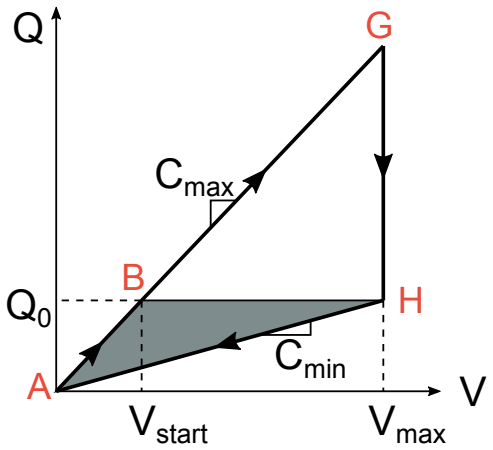

Figure 2.14. Two energy conversion cycles used in electret-free generation.

between two plates, respectively.

The capacitor is assumed to be initially charged to Q_0. The energy stored in the capacitor can, therefore, be expressed as

$$W_0 = \frac{Q_0^2}{C}. \tag{2.21}$$

Under a mechanical vibration that reduces the overlapping area A or the air gap d, the capacitance C is, therefore, decreases. This combined with the relation in equation (2.21) leads to an increase of the energy stored in the capacitor, which can be extracted to charge a battery or a supercapacitor.

In general, electrostatic energy harvesters can be categorized into two types: electret-free and electret-based. The difference is the type of priming sources used to initiate the energy conversion process. Electret-free transducers require additional voltage or charge sources, while electret-based generators employ pre-charged electrets.

Electret-free transducers can generate electricity using the two energy conversion cycles in the charge-voltage plane shown in Figure 2.14. Path A-B-H-A depicts charge constrained conversion, while path A-G-H-A depicts voltage constrained conversion. The name of the path depicts which parameter is held constant during the conversion process while the other changes in response to a capacitance variation. The amount

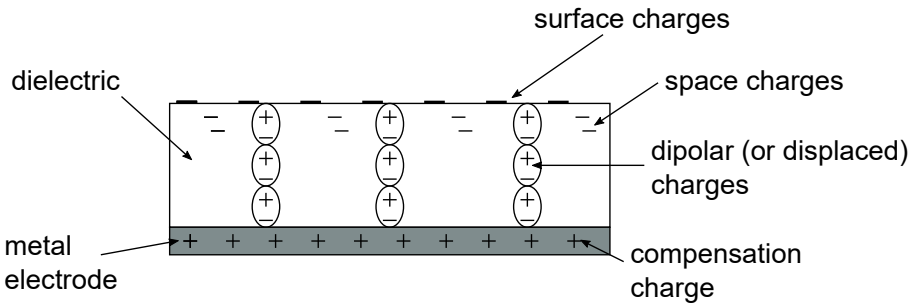

Figure 2.15. Schematic cross section of a one-sided metalized electret consist of excess surface charges, injected space charges and aligned dipolar charges.

of energy harvested within a conversion cycle is the difference of energy stored in the transducer at the beginning and the end of the cycle, presented as

$$\Delta W = \frac{Q_{end}V_{end} - Q_{start}V_{start}}{2}. \tag{2.22}$$

The calculation is also equivalent to the bounded area of the path within the charge-voltage plane highlighted in Figure 2.14.

One major drawback of the electret-free generation is the need of external sources to hold voltage or charge to start a conversion process (Meninger et al. 2001, Yen & Lang 2006). This leads to sophisticated synchronous switching circuits to take charges from the sources to initiate the conversion cycle and returned them back to the reservoir at the end of the cycle. Such interface circuits also increase losses during the conversion process. The reader is referred to (Meninger et al. 2001, Yen & Lang 2006, Boisseau et al. 2012) for a more detailed design of the interface circuits used in electret-free approach.

Electret-based energy harvesting, on the other hand, can autonomously operate without the need of external voltage sources due to the presence of an electret - a dielectric material that has a quasi-permanent electric charge or dipole polarization. An electret can, therefore, be considered as the electrostatic equivalent of a permanent magnet.

Depending on the fabrication process, electret can be categorized into three types,

one may consist of real charges such as surface charge layer or space charges, one may be formed due to the effect of re-aligned dipole polarization, and the other may also be the combination of these. Figure 2.15 illustrates these types of charges which may occur in an electret. Given the ability to generate internal and external electric fields, an electret, when being implemented in vibration energy harvesting, induces charges in the two electrodes of a capacitive microgenerator. Under external mechanical vibrations, the capacitance of an electrostatic microgenerator changes, forcing the induced charges to travel back and forth, and therefore, generates an electric current which can be used to charge a battery or power microelectronic devices. A further detail of electret and electret-based microgenerators is presented in Chapter 3.

The principle of electrostatic vibration energy harvesters is to vary capacitance in order to generate electricity. According to equation (2.20), either dielectric constant ε, overlapping area A or the distance between the two plates, d, can be varied. To change the equivalent relative permittivity of dielectric medium, there is a need to change the material properties during operation, which is impractical. One work-around solution is to employ a multiple dielectric structure, such as air and a non-conductive liquid presented in (Bu et al. 2013*a*). Under a mechanical vibration, the shape of the liquid contained in the encapsulated structure varies, resulting in a change of capacitance and hence, electric generation. One major limitation of this approach is the need to employ a non-conductive liquid, and consequently, increases the cost of packaging to prevent leakage. Also, the capacitance change ratio is relatively small (less than 30), leading to a small amount of energy harvested at the output. As a result, changing ε is unfavorable. On the other hand, the methods of varying either overlapping area A and dielectric distance d are widely implemented in electrostatic-based energy harvesting due to the ease of high capacitance variation. However, these approaches also have two major limitations. First, the mechanical damping is much higher in these structures due to the use of mechanical springs to create the relative movement. Second, mechanical stoppers may be required in some cases to prevent

shorting the two plates which potentially leads to a failure of the whole system. Nevertheless, the most attraction of electrostatic-based transduction mechanism is the ease of the integration into microsystem using standard micro manufacturing processes such as MEMS. In addition, the mechanism can output adequate voltage from a few hundred millivolts to the tens of volts which can be easily rectified and conditioned.

Given these advantages, electrostatic-based transduction mechanism has been attracting much interest in the research community and has demonstrated the capability throughout several studies and prototypes. A summary of the studies in the literature is presented in Table 2.7.

2.2.4 Comparison of transduction mechanisms

The purpose of this comparison is to identify the most suitable power transduction mechanism to implement into our targeted applications for mobile and wearable devices. Here, the three essential requirements of these applications, including compact sizes, the abilities to harvest energy at low-frequency and low-acceleration excitations, are evaluated for three transducer mechanisms discussed in Subsections 2.2.1, 2.2.2 and 2.2.3. The performance of state-of-the-art prototypes listed in Tables 2.3, 2.6 and 2.6 with regard to these three factors are plotted in Figure 2.16. The strengths and weaknesses of each transduction mechanism are also summarized in Table 2.8.

Based on the results shown in Figure 2.16, piezoelectric microgenerators can produce high power density at low acceleration, but poorly perform at low-frequency excitations. A similar observation is also applied to electromagnetic transducers. Here, electrostatic generators can produce high output power at low-acceleration and low-frequency vibrations in small form packages. Electrostatic microgenerators with pre-charged electrets are not only able to autonomously scavenge ambient vibrations to produce high voltages at the output, but also compatible with standard microfa-

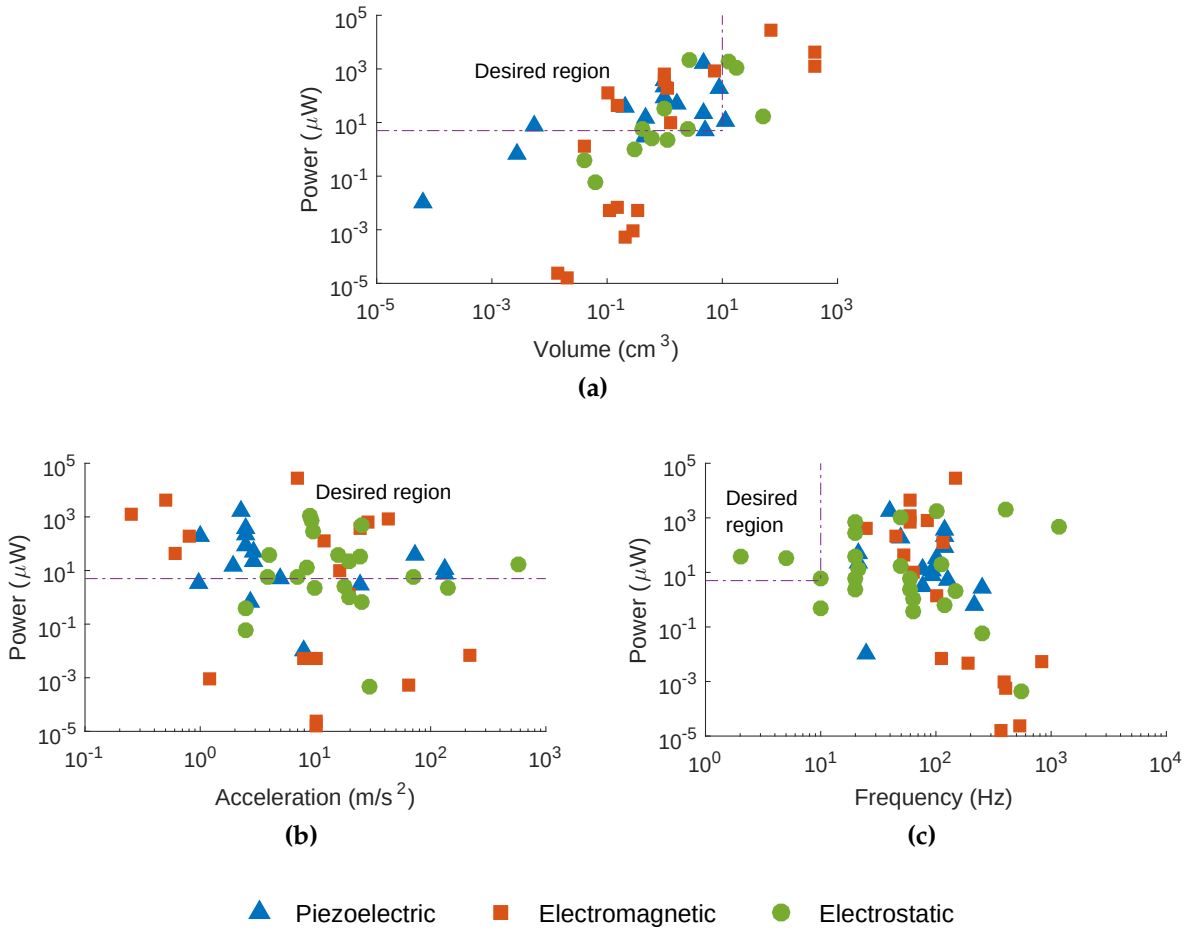

Figure 2.16. Power generated from existing prototypes is a function of (a) device volume, (b) input acceleration and (c) frequency. These plots are based on the data presented in Tables 2.3, 2.6 and 2.7.

brication using MEMS processes. Given such advantages, electrostatics using pre-charged electret is the focused transduction mechanism investigated in this research. The next chapter will provide more details on electrets and the development and characterization of electret-based microgenerators.

2.3 Conclusions

The chapter discusses the advantages and disadvantages of some common system types and power transduction mechanisms when designing a vibratory microgenerator. Based on the considerations, non-resonant electrostatic transducers with pre-charged

Table 2.7. Comparison of recent small scale electrostatic generators.

	Reference	Active volume (cm^3)	Acceleration (m/s^2)	Frequency (Hz)	Power (μW)	Power density ($\mu W/cm^3$)
Electret-free	Despesse et al. (2005)	18	8.9	50	1052	58.44
	Basset et al. (2009)	61.49E-3	2.5	250	61E-3	1
	Yang et al. (2010)	0.0394	2.5	63	0.39	9.90
	Kiziroglou et al. (2010)	-	-	10	0.5	
	Choi et al. (2011)	1	24.67	5	35.3	35.3
	Basset et al. (2014)	1.1	9.81	150	2.2	2
Electret-based	Arakawa et al. (2004)	0.4	3.9	10	6	15
	Boland et al. (2005)	-	70	60	6	-
	Miao et al. (2006)	0.6	17.8	20	2.4	4
	Tsutsumino, Suzuki, Kasagi & Sakane (2006)	-	15.8	20	37.7	-
	Tsutsumino, Suzuki, Kasagi, Kashiwagi & Morizawa (2006)	-	9.5	20	278	-
	Lo et al. (2007)	-	142.1	60	2.267	
	Lo & Tai (2008)	50	576.6	50	17.98	0.36
	Sakane et al. (2008)	-	9.2	20	700	-
	Yang et al. (2008)	-	29.43	546	4.6E-4	-
	Edamoto et al. (2009)	-	8.5	21	12.5	-
	Naruse et al. (2009)	-	4	2	40	-
	Miki et al. (2009)	0.305	19.6	63	1	3.28
	Yang et al. (2011)	2.56	6.9	20	5.9	2.3
	Chiu & Lee (2012)	-	19.6	110	20.7	-
	Altena et al. (2013)	-	25	1187	495	-
	Bu et al. (2013*b*)	-	25	120	0.66	-
	Perez et al. (2015)	2.7	-	406	2100	777.78
	Perez et al. (2016)	12.6	-	100	1.8E3	111

Table 2.8. Comparison between common transduction mechanisms used in vibration energy harvesting.

	Piezoelectric	**Electromagnetic**	**Electrostatic**
Output voltage	High voltage (2-10 V)	Extremely low voltage (5-200 mV)	- Depend on the priming source for electret-free generators - Adequate output voltage (0.5-10 V) for electret-based generators
Output current	High output current	High output current	Low output current
Output impedance	Medium output impedance (100 kΩ to MΩ)	Low output impedance (kΩ)	High output impedance (MΩ-GΩ)
Fabrication	- Micro-scale fabrication is not compatible with standard complementary metal oxide silicon (CMOS) processes - Difficult in circuit integration	- Complicated fabrication at micro scales - Difficult to integrate into microelectronics	- Compatible with MEMS fabrication - Easy to integrate into microelectronics
Mechanical control	No mechanical stoppers required	No need for mechanical contacts between parts	- Might require mechanical stoppers to prevent shorting - Complicated packaging due to micrometer gap control
Autonomous operation	Self-operate without external voltage sources	Self-operate without external voltage sources	Electret-free generators require external priming source
Loss	Self-discharge at low frequencies	Ohmic losses in coils	Parasitic capacitance losses
Cost	High due to piezoelectric materials	Low	Possibility to build low cost systems

electrets are selected as the primary topic of this research. The next step is to investigate further the fabrication techniques to manufacture these structures and deep dive into their fundamental operating mechanisms in order to maximize the energy conversion efficiency.

Chapter 3

Electret-based energy harvesting

This chapter introduces electrets and the methods used to form the materials. The characteristic equation of electret-based microgenerators used in vibration energy harvesting is also derived and presented in this chapter. A simulation-based technique is then followed to numerically analyze the performance of the microgenerators. Finally, the formulation of analytical model for the microgenerators under constant-speed rotations is presented.

3.1 Electret

According to (Broadhurst et al. 1987, Chapter 1), an electret is a piece of a dielectric material exhibiting a quasi-permanent electrical charge. This effect means that the time constant characteristics for the decay of charge held by the material is much longer than the time period of any studies conducted on the materials.

In general, electret can be categorized into three different types depending on the formation of charges inside the materials. The first one is the excess of real charges such as the charges trapped on the top surface of a dielectric material or space charges injected into the material. The second type is the oriented polarization in which the molecules of the material is re-aligned under the effect of an electric field. The last one is the combination of the two types. These types of charges are illustrated in Figure 2.15.

Given such properties, electrets can generate internal and external electric fields if not being covered by electrodes. Thus, an electret has often been considered as an electrostatic analogue of a permanent magnet, although the electric properties are

due to either dipolar or monopolar charges, while magnetic properties are caused by only magnetic dipoles. As a result, when being implemented in energy harvesting, electret induces charges on electrodes. Under a mechanical vibration, the change of the system capacitance forces these charges to move back and forth, and hence, the generation of electricity.

3.1.1 Physical properties

Electrets are, in general, dielectrics, but not all dielectrics can become high-performance electrets. High-performance electrets are defined as the materials which can retain a high charge density for a long time (more than 5 years). Hence, it is essential to study the physical properties of electrets to select the right materials to form high-performance electrets. In general, conductivity, mobility and dipolar relaxation frequency are the three common properties used to determine a good electret.

The intrinsic conductivity of dielectric is a property which allows the transportation of an electric charge. Hence, it is mainly responsible for the decay of excess real charges within the material. In a simple case where the excess charges are located on the surfaces of an open-circuit sample with conductivity g and relative permittivity ε, the time constant of the charge decay is given by

$$\tau_1 = \frac{\varepsilon\varepsilon_0}{g}, \tag{3.1}$$

where ε_0 is the permittivity of free space.

A good electret can hold charges for a long period of time, and hence, the time constant τ_1 is very large, corresponding to a very small conductivity g. Therefore, a lower conductive dielectric may potentially become a good electret. The other way around may not be true.

Another factor attributed to the decay of excess charges is carrier mobility, μ, which characterizes how quickly a charge can move through the material under the

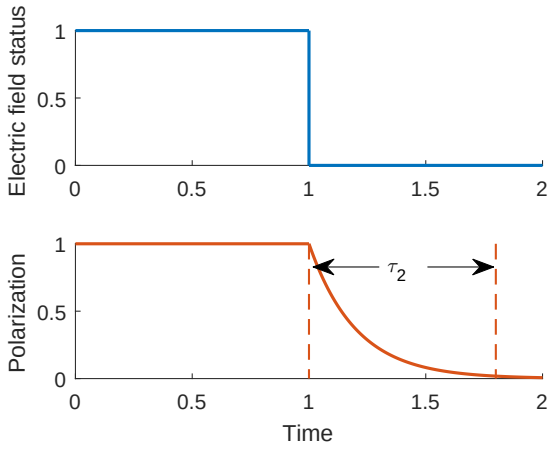

Figure 3.1. Illustration of dipole relaxation frequency or relaxation time in an electret.

effect of an electric field. For electrets, under the initial potential difference across a sample caused by excess charges, V_0, a charge located on the nonmetallized surface of a one-sided metalized sample with thickness d spreads through the dielectric sample with a time transit presented as

$$\tau_\lambda = \frac{s^2}{\mu V_0}. \tag{3.2}$$

Again, for electrets, τ_λ is expected to be as small as possible to lengthen the lifespan of electrets. Hence, dielectrics with low mobility are preferable to make good electrets.

One important factor attributed to the decay of a uniform dipole alignment when the driving force or electric field is off is dipole relaxation frequency, ω. In the time domain, this property is determined by a relaxation time $\tau_2 = 1/\omega$, as shown in Figure 3.1. A good electret is, therefore, desired to exhibit a very long decay time, corresponding to a small ω. Hence, the materials with low dipole relaxation frequencies are often preferred to fabricate high-performance electrets.

In summary, one can select appropriate materials with such properties in order to make high-performance electrets. Table 3.1 provides some of the state-of-the-art electret materials which can retain high charge density for a very long time, often more than 5 years. The readers are referred to (Sessler 1987) for further information about electrets.

Table 3.1. Properties of wellknown electret materials in the literature.

Material	**Conductivity** (S/cm)	**Dielectric constant**	**Max. charge density** (mC/m^2)
Teflon PTFE	$<10^{-18}$ [1]	2.1 [1]	-
Teflon FEP	10^{-18} [2]	2.0 [2]	0.5 - 1 [3]
Teflon AF	-	1.89 - 1.93 [4]	0.5 [5]
CYTOP-M CYTOP-A	$<10^{-17}$ [6]	2.0 - 2.1 [6]	1.37 [7] 2 [8]
Parylene-C	10^{-17} [9]	3.15 [9]	2.0 [10]
Parylene-HT	5×10^{-18} [9]	2.21 [9]	3.69 [11]
SiO_2/Si_3N_4	10^{-16}	3.9 [12]	11.51 [13]

3.1.2 Charging methods

The methods forming excess-charge electrets and dipolar electrets are quite different. Excess-charge electrets can mostly be achieved by injecting or depositing charge carriers using discharges or particle beams. In contrast, dipolar electrets are generally polarized by strong electric fields at properly selected temperatures. Both methods highly involve strong electric fields and therefore, the resultant electrets may exhibit both dipolar and excess charges. The state-of-the-art has seen many ways to form electrets using triboelectricity, penetrating radiation or photoelectrets. However, due to the ease of fabrication and the speed of forming electrets, thermal charging and isothermal charging are the two most common methods used in the literature of the electret formation ((Broadhurst et al. 1987, Section 2.2), (Suzuki 2011)).

[1] DuPont™ Teflon® PTFE fluoropolymer resin - Properties handbook
[2] DuPont™ Teflon® FEP - Fluoroplastic Film
[3] [Fig. 6](Sessler & West 1972)
[4] DuPont™ Teflon® AF Amorphous Fluoroplastic Resin - Adhesion Information
[5] (Hsieh et al. 1997)
[6] Agashi CYTOP amorphous flouropolymer catalog, AGC Chemicals, Asahi Glass Co.
[7] (Tsutsumino, Suzuki, Kasagi & Sakane 2006)
[8] CYTOP-A is doped with 3% aminosilane (Kashiwagi et al. 2011)
[9] Parylene Properties from Special Coating Systems™
[10] (Genter & Paul 2012)
[11] (Lo & Tai 2008)
[12] (Dorf 2003, Page 1-80)
[13] (Amjadi 1999)

The thermal forming method most likely results in both dipolar and excess charges. In general, to create dipolar alignment, a strong electric field is applied to a dielectric sample at an elevated temperature and subsequently, cool down while the field is still present. The elevated temperature is often selected above the glass transition point but well below the melting temperature of the sample material. Elevating temperature increases the mobility of molecules or molecular chains of the sample, and hence, under the effect of an electric field, those molecules or chains are easily aligned with respect to the direction of the applied field. If the dielectric sample is cooled in a sufficiently short time period compared to the time it is kept at the elevated temperature, the predominantly-aligned dipoles are frozen, resulting in a permanent polarization. The thermo-electret formation is, therefore, dependent on the effect of applied voltages and temperatures as follows: at voltages below the threshold for air gap breakdown (known as Paschen's curve for air gap at atmosphere pressure), the dominant effect forming an electret is the internal hetero-charge polarization. Higher applied voltages increase the occurrence of homo-charge deposition on the top surface of the dielectric material. Thus, the effect of higher voltages favors charge deposition over internal polarization, while an opposite effect is observed when increasing temperatures. In addition, the resulting charges also depend on the properties and dimensions of the materials used as well as the duration of the charging (Broadhurst et al. 1987).

The isothermal forming method is mostly dependent on the charge transfer or deposition due to the absence of a cooling or heating. The most widely used technique in isothermal-electret formation is corona-charging illustrated in Figure 3.2. The arrangement consists of a sharp needle electrode biased at a few kV against the dielectric sample and a wire mesh at a potential of at least a few hundreds of volts. The purpose of the grid electrode is to control the current to the sample to obtain a uniform distribution of deposited charges. Corona charging method is often carried out by applying negatively biased voltages on both needle and grid electrodes at at-

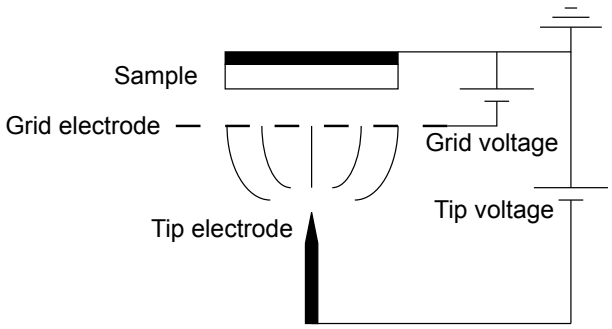

Figure 3.2. Schematic of a corona discharge to form electrets.

mospheric pressure. The electric field generated by the applied voltages ionizes the air gap and drives the induced negative carriers toward the dielectric sample. Due to their small energy, those ions are deposited in the surface layer without penetrating the material. Charge penetration mostly depends on charge polarity, charge density and the surface characteristics of the materials used. Sessler (1987) reported that negative charges do not or slightly penetrate on Teflon, while a substantial penetration is observed for positive charges. In addition, the resulting charges in PTFE is more stable using a negative charging than a positive one. As a result, a negatively biased voltage configuration is often found in corona discharge stations to form electrets.

A custom-made corona discharge station following the schematic shown in Figure 3.2 was setup in the University of Adelaide to make electrets to prototype electret-based microgenerator. The station consists of a base socket, three PTFE cylindrical insulators, a copper grid electrode and a brass needle electrode as shown in Figure 3.3. The gap distance between the needle and the grid electrodes are adjusted to be about 1 cm. A sample holder is placed 5 mm above the grid electrode and can hold a substrate with the dimension up to 3-by-3 cm^2. The detailed drawing of the corona discharge station is included in Appendix A.

Two high DC voltage supplies are employed to power the corona-discharge station. The needle electrode is connected to a custom-made voltage source which can provide up to 7.5 kV, while the gird electrode is powered by a Glassman PS/KL002R1.5-22 with a positive configuration. According to (Sessler 1987), negative voltage sup-

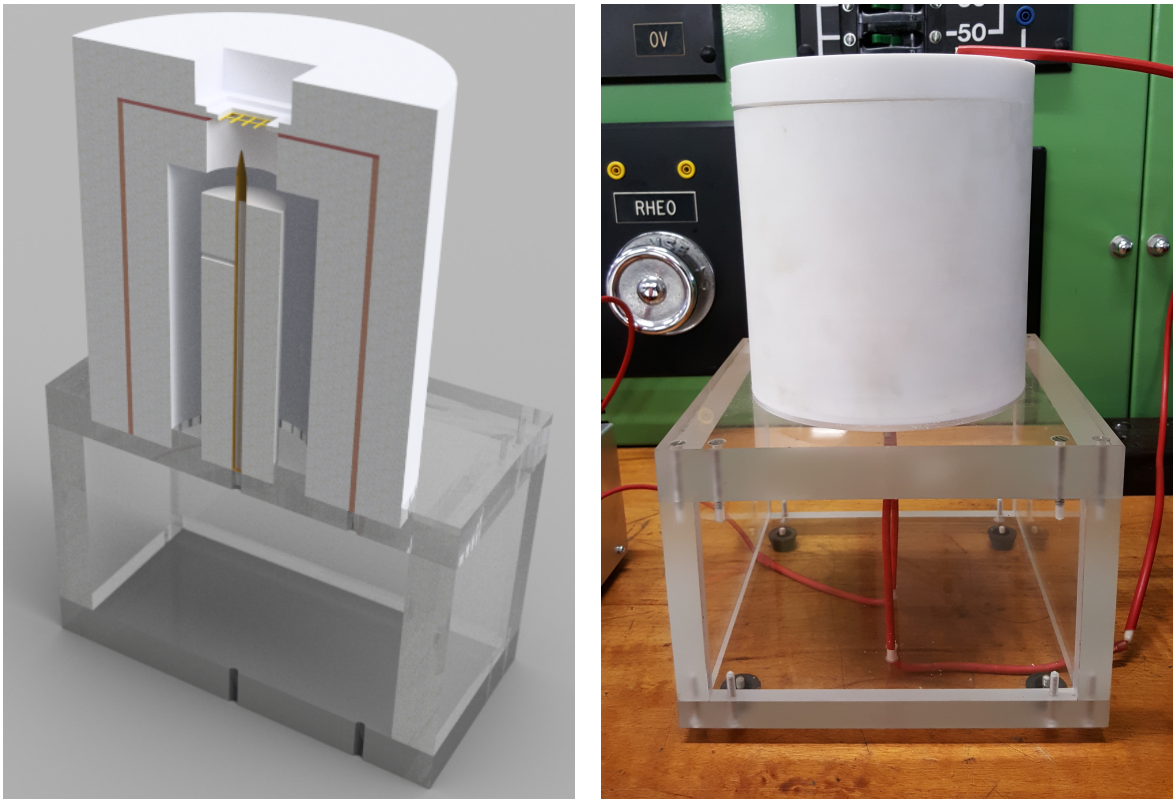

(a) (b)

Figure 3.3. A custom-made setup of a corona discharge station: (a) a 3D model, and (b) real view of the corona discharge station used to make electrets.

plies are desirable, however, due to the limited resources, these two power supplies with positive polarity are utilized to form electrets. At the time of the writing of this thesis, two negative-voltage power supplies, *LNC 10000 - 5 neg* and *LNC 1200 - 50 neg* from Heinzinger, are ordered to replace the two positive-voltage supplies for future electret fabrication.

3.2 Electret-based microgenerators

The most challenge in designing small scale power transducers, and in particularly electret-based microgenerators, is to operate in a wide range of low-frequency excitations. The development of non-resonant electret-based microgenerators is, therefore, the key focus on power generation that satisfies such requirements. This section

presents the state-of-the-art non-resonant vibration electret-based microgenerators, including their normalized power density as a parameter to compare their effectiveness. As discusses in Subsection 2.1.1, the output power of a microgenerator is proportional to the square of the input acceleration, the normalized output power is often defined as power density per the square of input acceleration. However, most experiments published in the literature often reported the testing frequencies, while the tested vibration amplitudes are sometimes not specified. Hence, in this section, the normalized power is defined as the power density generated within a cycle of external vibrations. The final part of this section will outline the derivation of the governing equation and the simulation to numerically analyze the performance of electret-based microgenerators.

3.2.1 State of the art

Small scale electret-based generators had been well studied and developed even before the era of micro- and nano-technologies. Significant early research efforts on electret-based generators were undertaken by Jefimenko & Walker (1978) and Tada (1986). Early small-scale generators used positively and negatively charged electrets embedded into a slot structure illustrated in Figure 3.4a. The downside of this configuration is the potential neutralization of the two oppositely charged electrets placed next together, leading to a reduction of power generated. To overcome this weakness, (Tada 1992) patterned only negatively charge electrets on the counter electrode in an unpackaged cross-wafer configuration shown in Figure 3.4b. Analytical models of these devices were also developed to provide an understanding of the operation mechanism of these small-scale generators as well as the optimization for a higher power conversion efficiency (Tada 1992). In spite of low practicabilities due to using non-standard fabrication and undesirable sizes, these proof-of-concept transducers demonstrated the potential of using electrets for micro power generation as well as

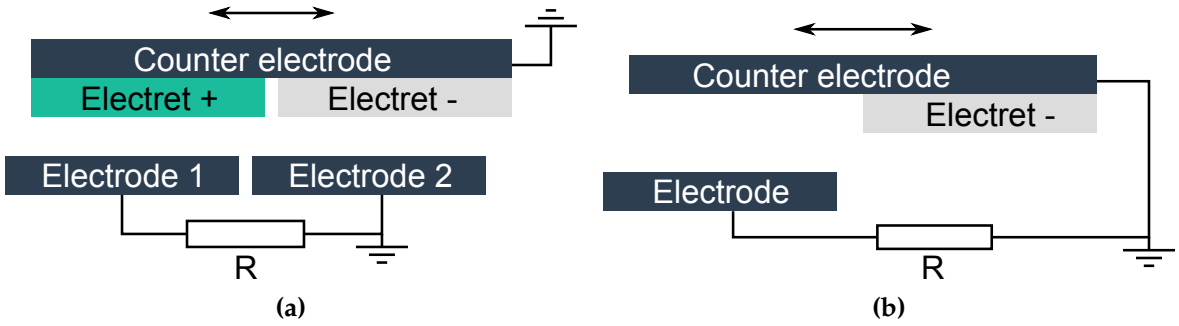

Figure 3.4. Illustrations of early electret-based generators (a) two oppositely polarized electrets (b) single negatively charged electret.

initiated a new trend in energy harvesting.

The trend in micro power generation using electret was really taken placed in the early 2000s when microfabrication processes started to be established and especially, the booming of electronic products such as cell phones, laptops, and many more portable devices. One of the very first devices developed during this period using microfabrication techniques is a rotational structure proposed by Boland et al. (2003). The device is constructed in a similar configuration as the one presented in (Tada 1992), except the non-electret part of the counter electrode is also etched to maximize the capacitance change to obtain a higher power conversion. Subsequently, several implementations using various microfabrication techniques are carried out to prototype many microgenerators that can harvest energy at low-frequency vibrations to power mobile and wearable devices.

One of the non-resonant microgenerators which can scavenge a very low-frequency vibration for power generation can be realized as a linear bearing based design proposed by Naruse et al. (2009). The device consists of two parallel plates suspended using a pair of linear micro ball bearings. Owing to this spring-less configuration, one of the two plates can easily move back and forth even under an excitation less than 10 Hz. As reported, the 0.3 cm^3 prototype illustrated in Figure 3.5a can produce 40 μW at a 2 Hz vibration, which equals to 66.67 $\mu J/cm^3$.cycle. Using the same prin-

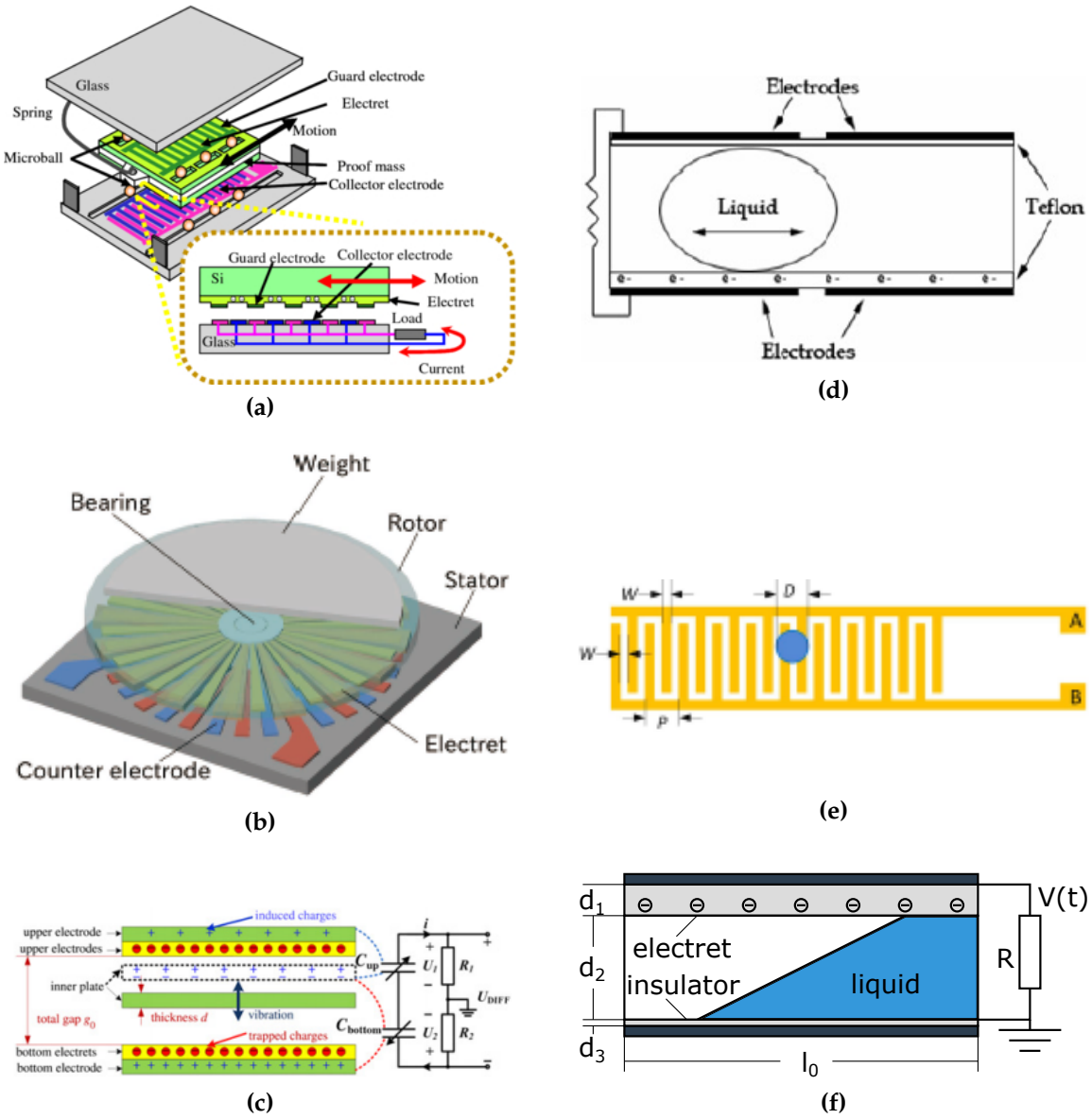

Figure 3.5. Some non-resonant electrostatic energy harvesters in the literature using: (a) linear microball bearing (Naruse et al. 2009), (b) miniatured ball bearing (Nakano et al. 2015), (c) freestanding plate (Bu et al. 2013*b*), (d) encapsulated conductive liquid (Boland et al. 2005), (e) conductive droplet and (f) water sloshing phenomenon of non-conductive liquid (Bu et al. 2013*a*).

ciple of changing overlapping area, Nakano et al. (2015) employed a miniature ball bearing in order to construct a pendulum-like prototype illustrated in Figure 3.5b. The 0.03 cm^3 device is reported to generate 3.6 μW at 1 Hz, which corresponds to 120 $\mu J/cm^3$.cycle. In another study, Bu et al. (2013*b*) adopted the vertical gap changing

method as shown in Figure 3.5c to harvest energy at low frequency. When being excited, the freestanding plate can freely move up and down, resulting in a change of the device capacitance and therefore, generate differential voltages at the output. Based on the experiment results conducted at 5 Hz, the 0.036 cm^3 prototype can produce up to 0.41 μW in total, which is equivalent to 2.28 $\mu J/cm^3$.cycle.

A major drawback of these microgenerators is the heavy dependency on mechanical movement of rigid bodies, which has a higher damping, resulting in a higher energy loss. In addition, these structures might have potential problems related to the reliability in long term operations. As a result, non-rigid body or fluid is proposed as an excellent alternative solution. Boland et al. (2005) is one of the very early researchers that employed conductive liquid encapsulated between two plates of a micro-machined prototype shown in Figure 3.5d to scavenge energy. Although the prototype was tested at a 60 Hz, which is quite high for the considered applications, the constructed device is possible to work at low frequency. In a similar study, Yang et al. (2014) used ionic liquid sliding on a planar interdigital electrode illustrated in Figure 3.5e and conducted experiments to investigate the performance of the generator. Unfortunately, the testing methods did not include the common sinusoidal translational excitations, and consequently, no normalized power density can be calculated. Recently, Bu et al. (2013*a*) took a different approach when using a non-conductive liquid to vary the dielectric media between the two plates of their capacitive microgenerator. The result of the experiment at 10 Hz showed that the 0.6 cm^3 prototype can generate 0.18 μW, which equals to 0.03 $\mu J/cm^3$.cycle.

Given the advantages of liquid-based microgenerators, a microgenerator prototype was proposed . The prototype was employed the sloshing phenomenon of a conductive liquid for power generation. The structure of the microgenerator is similar to the one presented in (Choi et al. 2011), except electret was embedded into the structure. Due to the limited resources available, a quite thick electret was fabricated, resulting in a reduction of output voltage. Preliminary test results showed that

a 1-cm^3 device can generate 1.6 V peak-to-peak open circuit voltage as shown in Figure B.8. The details of the design, simulation, fabrication and preliminary testing of this device are included in Appendix B.

Given the performance of the state-of-the-art devices, it has been demonstrated that non-resonant electret-based microgenerators are able to harvest energy at low-frequency vibrations to power microelectronics. In order to understand further the capability of electret-based microgenerators, the derivation of the governing equation which characterizes the electrodynamics of electret-based microgenerators is presented in the next subsection.

3.2.2 Governing equation of electret-based microgenerator

This section presents the formulation of a governing equation which describes the dynamic behavior of electret-based microgenerators. The section also includes a description of the simulation presented in (Boisseau et al. 2010), which employs finite element modeling and numerical methods to analyze the performance of electret-based microgenerators.

For simplification, we assume that the excess of the negative free charge $-\sigma$ on the surface of the electret film induces a 1-dimensional electric field notated as $\vec{E_d}$ and $\vec{E_g}$ shown in Figure 3.6. Applying Kirchoff's law of voltage to the loop starting from the based electrode to the load resistor R_L, the counter electrode, the electret

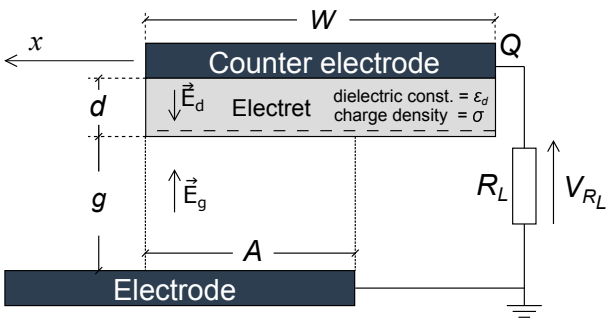

Figure 3.6. Schematic of electret-based microgenerators.

and then the air gap gives the following relation

$$V_{R_L} + E_d d - E_g g = 0. \tag{3.3}$$

Each of the parameters V_{R_L}, E_d and E_g are then correlated to the induced charge $Q(t)$ to obtain an equation describe the electrodynamic characteristics of the microgenerator. First, V_{R_L} can be calculated using Ohm's law and expressed as

$$V_{R_L} = -R_L \frac{dQ(t)}{dt}. \tag{3.4}$$

Second, the expressions of the resulting electric fields E_d and E_g can be determined by applying Gauss' law in the volumes that respectively include the electret and the counter electrode, and the electret and air gap, presented as

$$E_d = \frac{-\sigma}{\varepsilon\varepsilon_0} - \frac{Q(t)}{\varepsilon\varepsilon_0 A} \tag{3.5}$$

$$E_g = \frac{Q(t)}{\varepsilon_0 A}. \tag{3.6}$$

Finally, equations (3.4), (3.5) and (3.6) are then substituted into equation (3.3) to derive a governing equation of the microgenerator as

$$R_L \frac{dQ(t)}{dt} + \frac{d + \varepsilon g}{\varepsilon\varepsilon_0 A} Q(t) + \frac{\sigma d}{\varepsilon\varepsilon_0} = 0. \tag{3.7}$$

The differential equation can also be rewritten in a compact form expressed as

$$\frac{dQ(t)}{dt} = -\left[\frac{Q(t)}{R_L C(t)} + \frac{V_0}{R_L}\right], \tag{3.8}$$

where $C(t)$ is the instantaneous capacitance of the microgenerator and V_0 is the sur-

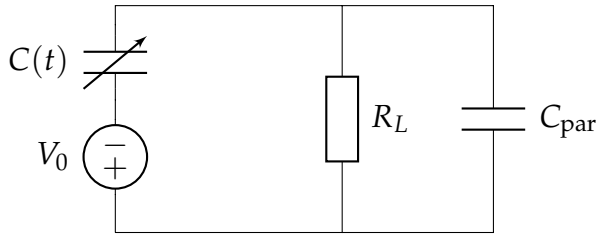

Figure 3.7. An electret-based microgenerator is generally equivalent to a variable capacitor in series with a constant voltage source. The effect of parasitic capacitances induced by external harvesting circuits and the fringe capacitance of the microgenerator itself is lumped into C_{par} connected in parallel with the microgenerator to refine the theoretical model.

face potential of the electret. Both $C(t)$ and V_0 are respectively defined as

$$C(t) = \frac{\varepsilon\varepsilon_0 A}{d + \varepsilon g}, \quad V_0 = \frac{\sigma d}{\varepsilon\varepsilon_0}.$$

Equation (3.8) is very similar to the governing equation of an RC circuit with a constant voltage source V_0 connected in series. Given this observation, (Boisseau et al. 2010) used a variable capacitance $C(t)$ connected in series with a constant voltage source V_0 as shown in Figure 3.7 to model the microgenerator.

To refine further the electrodynamic characteristics of the microgenerator taking the effect of parasitic capacitances induced by harvesting circuitry and the fringe capacitance of the microgenerator itself, Boisseau et al. (2012) proposed to include a lumped capacitor C_{par} in parallel with the microgenrator as shown in Figure 3.7. The governing equation of the microgenerator, in this case, is changed to

$$\frac{dQ(t)}{dt} = -\frac{1}{1 + \frac{C_{\text{par}}}{C(t)}} \left[\left(\frac{1}{R_L C(t)} - \frac{C_{\text{par}}}{C(t)^2} \frac{dC(t)}{dt} \right) Q(t) + \frac{V_0}{R} \right]. \tag{3.9}$$

Due to the additional capacitor C_{par}, the calculation of the voltage generated across the external load, R_L, is changed and expressed as

$$V(t) = V_0 + \frac{Q(t)}{C(t)}. \tag{3.10}$$

Here, the dielectric ε, the air gap g and the instantaneous overlapping area A are purposely left undefined to give the freedom to describe different types of excitations. As mentioned in Subsection 2.2.3, varying ε leads to a small capacitance variation, while changing g requires additional mechanical stoppers to prevent shorting. Hence, the overlapping area, A, is the favorable parameter which is varied to generate electricity. The trade-off when varying A is the occurrence of singularity in equation (3.8) when there is no overlap between the two plates of the microgenerator, and consequently, complicates the analysis. As a result, simulation-based approaches using finite element modeling and numerical methods presented in Subsection 3.2.3 are often used to analyze the performance of the microgenerator.

3.2.3 Simulation using FEM and numerical methods

This section presents a FEM computation of capacitance and numerical methods to solve equation (3.8) for the induced charge $Q(t)$. The variable parameter illustrated in this section is the instantaneous overlapping area $A(t)$. Similar approaches can be used in the cases of varying air gap g or relative permittivity ε.

The simulation is carried out as follows: The geometry of the microgenerator at each displacement instance is generated in a FEM solver to compute capacitances. These capacitances are then substituted into equation (3.11) to numerically solve for the induced charge $Q_{\text{FEM}}(t)$. Subsequently, the output voltage and power generated from the microgenerator are numerically calculated.

$$\frac{dQ_{\text{FEM}}(t)}{dt} = -\left[\frac{Q_{\text{FEM}}(t)}{R_L C_{\text{FEM}}} + \frac{V_0}{R_L}\right]. \tag{3.11}$$

The procedure starts with computing the FEM capacitance of the microgenerator, C_{FEM}, using a finite element solver, and in this case is ANSYS Maxwell. Depending on the structure of the microgenerator, a 2D or 3D geometry is generated. For simplicity, the demonstration here uses a 2D structure with its unit cell illustrated in

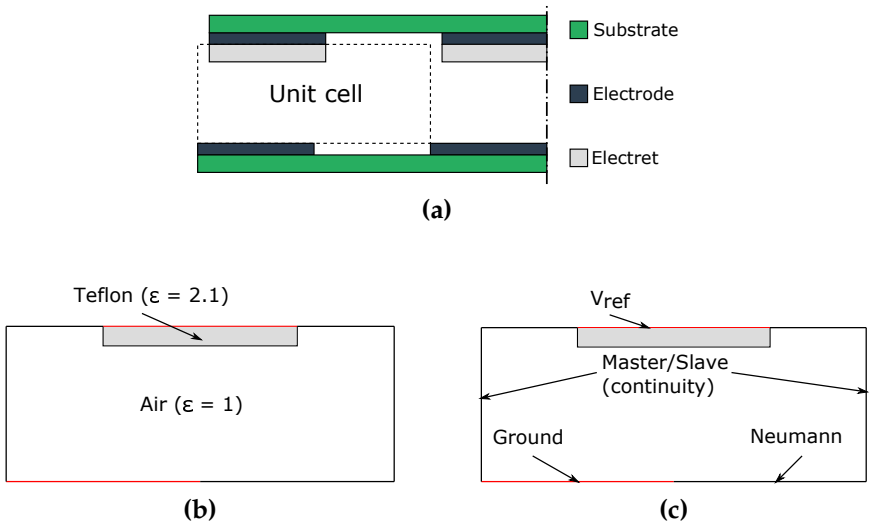

Figure 3.8. Details of a 2D FEM model to compute the capacitance of a microgenerator under a translational vibration: (a) definition of a unit celll, (b) materials used in the FEM simulation and (c) boundary condition setup.

Figure 3.8a. The materials and boundary conditions used in the FEM model are presented in Figure 3.8b and Figure 3.8c. The electrode and counter electrode, illustrated in Figure 3.6, are considered in the FEM as parts of the boundary conditions shown in Figure 3.8c. The FEM is carried out by setting a voltage V_{ref} on one of the electrodes while grounding the other electrode. The counter electrodes are then moved in steps along the horizontal axis in the case of translation vibrations or rotated around z-axis in case of rotational excitations. At each step, the FEM capacitance of the unit cell is combined with the number of poles to calculate the FEM capacitance of the whole microgenerator.

The results of C_{FEM} plotted in Figure 3.9 resemble a cosine function of the corresponding displacement, which is in a good agreement with (Boisseau et al. 2010). Therefore, under a translation excitation $x = X \sin \omega t$, C_{FEM} of a microgenerator with electrode width W can be approximated as

$$C_{\text{FEM}}(x) = \frac{C_{\text{max}} + C_{\text{min}}}{2} - \frac{C_{\text{max}} - C_{\text{min}}}{2} \cos\left(\frac{\pi x}{W}\right), \tag{3.12}$$

where C_{max} and C_{min} are the maximum and minimum capacitances calculated using

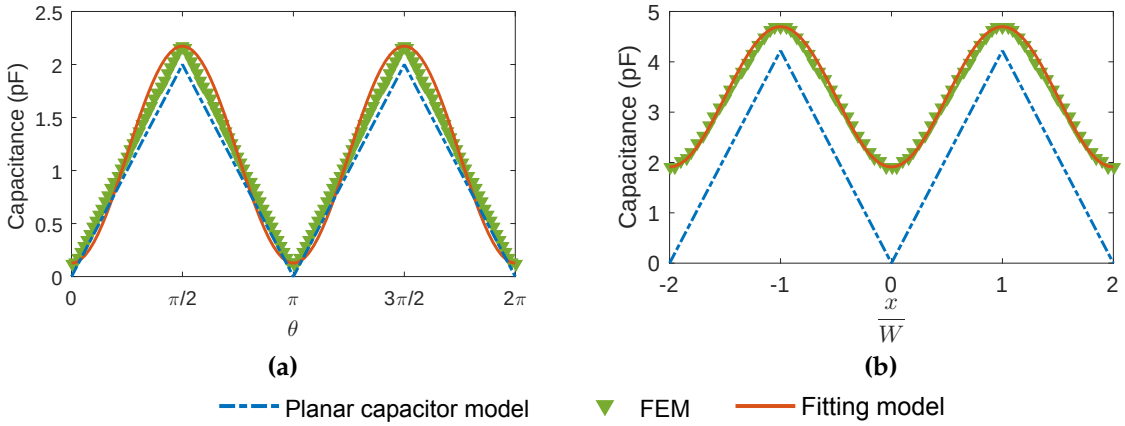

Figure 3.9. FEM capacitance results of (a) capacitance of the microgenerator in (Bartsch et al. 2009) under a constant speed rotation, and (b) the microgenerator in (Tsutsumino, Suzuki, Kasagi, Kashiwagi & Morizawa 2006) under a translational excitation resemble sinusoidal functions.

FEM, respectively, and depend on the geometry of the microgenerator.

Similarly, under a constant speed rotational excitation at frequency f, C_{FEM} can be approximated to

$$C_{\text{FEM}}(x) = \frac{C_{\max} + C_{\min}}{2} - \frac{C_{\max} - C_{\min}}{2} \cos(n\theta), \tag{3.13}$$

where n is the number of pair of poles and $\theta = 2\pi f t$ is the angular displacement.

It is important to note that the 180° out of phase between the formulas given in (3.12) or (3.13) and the expression presented in (Boisseau et al. 2010, equation (6)) is due to the difference of the initial overlapping area. Here, we define zero overlap at $x = 0$ or $\theta = 0$, while in (Boisseau et al. 2010), the theoretical overlapping area at $x = 0$ or $\theta = 0$ is 100 percent. This difference is purposely designed to ensure the consistency between the FEM based simulation and the assumption made in the analyses presented in Subsection 3.3 and Chapters 4 and 5 when formulating analytical models for the microgenerators.

Subsequently, numerical algorithms implemented into a numerical solver, such as Matlab, are used to solve equation (3.11) to calculate the output voltage and time

average power of the microgenerator. The algorithm flow is as the following. First, the input vibration is set as $x = X \sin \omega t$ for translational vibrations or $\theta = 2\pi f t$ for constant speed rotations. Second, the expression of FEM capacitance obtained in (3.12) or (3.13) is inserted into the differential equation (3.11). The equation is then solved in the time domain for the induced charge $Q(t)$ using a numerical solver. A sub-algorithm is defined to determine when the system reaches steady state. The obtained charge $Q_{\text{FEM}}(t)$ is then used to calculate the output voltage using the following formula

$$V_{\text{FEM}}(t_n) = -R_L \frac{Q_{\text{FEM}}(t_n) - Q_{\text{FEM}}(t_{n-1})}{t_n - t_{n-1}}. \tag{3.14}$$

The result of $V_{\text{FEM}}(t)$ is then employed to compute the root mean squared (RMS) voltage V_{RMS}. Finally, the time average power dissipated in the external load R_L is calculated using the formula

$$P_{\text{FEM}} = \frac{V_{\text{RMS}}^2}{R_L}. \tag{3.15}$$

The procedure is repeated for various values of the external load R_L.

For a general case where the effect of parasitic capacitances induced by external harvesting circuits is included, equation (3.11) is replaced by the corresponding form of equation (3.9). In addition, the calculation of the output voltage is also changed to

$$V_{\text{FEM}}(t_n) = V_0 + \frac{Q_{\text{FEM}}(t_n)}{C_{\text{FEM}}(t_n)}, \tag{3.16}$$

while the rest of the procedure is unchanged.

One popular application of this simulation is to numerically analyze and predict the performance of electret-based microgenerators. In addition, the method is also used in the validation of several analytical models formulated for the electret-based microgenerators in Sections 4.3 and 5.3. In this chapter, the simulation approach is demonstrated in Section 3.3 to validate an analytical model under a constant-speed

rotation - the simplest form of external excitations.

3.3 Analytical model under constant speed motions

Although the simulation presented in Subsection 3.2.3 provides a convenient way to analyze the performance of electret-based microgenerators, the method lacks insights and useful approximations to understand the operation mechanism of the microgenerators and the design trade-off involved. This section, therefore, presents a formulation of an analytical model for the microgenerators under the simplest type of excitation which is constant-speed rotational.

3.3.1 Theoretical model

For a rotational motion with constant frequency f, the overlapping area of a n-pair pole microgenerator is defined as

$$A(t) = \begin{cases} 2A_0 \dfrac{t}{T} & \text{for} \quad 0 \leq t < \dfrac{T}{2} \\ 2A_0(1 - \dfrac{t}{T}) & \text{for} \quad \dfrac{T}{2} \leq t < T \end{cases}, \tag{3.17}$$

where $T = 1/(nf)$ is the cycle of the rotation. Hence, in the time domain, the overlapping area $A(t)$ is a triangular function.

Owing to the symmetry of the microgenerator structure and the periodic nature of the excitation, only a first half cycle is analyzed. The behavior in the second half cycle can be found by reversing the sign of solution in the first half cycle. Given these assumptions, the equation describe the electrodynamic characteristics of the microgenerator given in (3.8) can be rewritten as

$$\frac{dQ(t)}{dt} = -\left[\frac{Q(t)}{\frac{2R_L C_0 t}{T}} + \frac{V_0}{R_L}\right]. \tag{3.18}$$

The solution of equation (3.18) can easily be obtained using integrating factor

method and presented as

$$Q(t) = c_1 t^{-\frac{T}{2R_L C_0}} - \frac{2C_0 V_0 t}{2R_L C_0 + T}, \tag{3.19}$$

where c_1 is an arbitrary constant. The "arbitrary" in this context means time-invariant.

At time $t = 0$, there is no overlap between the two plates of the microgenerator, the induced charge $Q(0) = 0$, and therefore $c_1 = 0$. We can also employ Ohm's law presented in (3.4) to calculate the theoretical output voltage of the microgenerator as

$$V_{R_L} = -R_L \frac{dQ(t)}{dt} = \frac{1}{1 + \frac{T}{2R_L C_0}} V_0. \tag{3.20}$$

Here, it is more convenient to use linear circuit elements, such as resistors, capacitors or inductors, to model the microgenerator using the derived results in (3.20). The modeling approach, in this case, is analogous to Thevenin's theorem, which defines a correlation between the open circuit voltage and short circuit current. The open circuit voltage can be determined when the external load resistor, R_L, approaches infinity, while the short circuit current is calculated by setting zero load resistance at the output as given in (3.21) and (3.22), respectively.

$$V_{\text{oc}} = \lim_{R_L \to \infty} V_{R_L} = V_0 \tag{3.21}$$

$$I_{\text{sc}} = \lim_{R_L \to 0} \frac{V_{R_L}}{R_L} = \frac{2C_0}{T} V_0. \tag{3.22}$$

The results in (3.21) and (3.22) shows a direct time-invariant relation between the open circuit voltage, V_{oc}, and the short circuit current, I_{sc}, which is indeed a characteristic of a resistor. Therefore, the microgenerator can be modeled as a constant voltage source V_{oc} in series with an internal resistance R_i defined as

$$R_i = \frac{V_{\text{oc}}}{I_{\text{sc}}} = \frac{T}{2C_0} = \frac{R_0}{2n}, \tag{3.23}$$

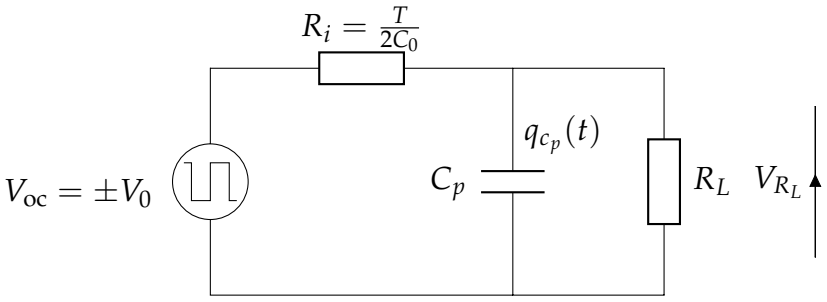

Figure 3.10. Under a rotational excitation, a microgenerator is equivalent to a squared-signal voltage source in series with a constant internal resistance. Parasitic capacitances induced by external harvesting circuitry and the generator itself are lumped into C_p to refine the model for a more accurate prediction of output voltage and power.

where R_0 is defined as

$$R_0 = \frac{1}{fC_0}. \tag{3.24}$$

Remark. *R_0 is directly analogous to the equivalent resistance of a switched capacitor C_0 at a switching frequency f as presented in (Franco 2002). Hence, a switched capacitor circuit can be used as an analogy to illustrate the operating mechanism of capacitive microgenerators.*

Although the theoretical model, particularly the equivalent circuit shown in Figure 3.10, is convenient to be used in the design and performance optimization of electret-based microgenerators, this model does not take into account the unavoidable parasitic capacitances which are the main error attribution in the predictions of the output voltage and power. The next subsection refines the model by taking stray capacitances into account and formulating a complete analytical model for a more accurate prediction.

3.3.2 Effect of parasitic capacitance

To practically model the microgenerator, Bartsch et al. (2009) proposed to lump parasitic capacitances to model the capacitive losses as a single stray capacitor C_p connected in parallel with the external load R_L as shown in Figure 3.10. The electrodynamics of the equivalent circuit in Figure 3.10, including C_p, can be described by the differential equation for the current flowing through C_p in term of the charge $q_{c_p}(t)$

stored in C_p and presented as

$$\frac{dq_{c_p}(t)}{dt} = -\frac{q_{c_p}(t)}{R_p C_p} + \frac{V_0}{R_i} \tag{3.25}$$

where $R_p = R_i \| R_L$.

It is also worthy to note that $q_{c_p}(t)$ is the charged induced in the lumped parasitic capacitance C_p, while $Q(t)$ presented in equation (3.8) is the charge generated on the electrodes of the microgenerator.

The boundary condition of equation (3.25) is the continuity of the charge induced in C_p, which requires the charge induced at the beginning equal to the one at the end of the output cycle, expressed as

$$q_{c_p}(0) = -q_{c_p}\left(\frac{T}{2}\right). \tag{3.26}$$

The output voltage across the external load, R_L, can be calculated as

$$V_{R_L}(t) = \frac{q_{c_p}(t)}{C_p} = \left[1 - \underbrace{\frac{2\exp\left(-\frac{t}{R_p C_p}\right)}{1+\exp\left(-\frac{T}{2R_p C_p}\right)}}_{\text{effect of parasitic capacitances}}\right]\frac{R_p V_0}{R_i}. \tag{3.27}$$

The effective power of the microgenerator can be calculated as the time average power within the first half cycle of the rotational excitation and presented as

$$\begin{aligned} P_{\text{avg}} &= \frac{2}{T}\int_0^{\frac{T}{2}} \frac{V_{R_L}^2(t)}{R_L} dt \\ &= \left[1 - \underbrace{\frac{4R_p C_p}{T}\tanh\left(\frac{T}{4R_p C_p}\right)}_{\text{effect of parasitic capacitances}}\right]\left(\frac{R_p}{R_i}\right)^2 \frac{V_0^2}{R_L}. \end{aligned} \tag{3.28}$$

The exponential and hyperbolic functions in (3.27) and (3.28) represents the effect of the lumped parasitic capacitance C_p. If C_p is neglected, the responses given in

Table 3.2. The parameters of the device published in (Bartsch et al. 2009).

Parameter	Description	Value
ε	Dielectric constant of CYTOP	2.1
σ	Charge density (mC/m^2)	0.93
A_0	Maximum overlapping area (cm^2)	0.37
d	CYTOP film thickness (μm)	9.5
g	Air gap spacing (μm)	155
n	Number of poles	2
f	Rotational frequency (Hz)	20

(3.27) and (3.28) will resemble the voltage divider model presented in Subsection 3.3.1.

3.3.3 Comparison between theory, simulation and experiment

The device used in this comparison is the prototype published in (Bartsch et al. 2009). The microgenerator consists of a two 2-pole parallel plates with the maximum overlapping area $A_0 = 0.37$ cm^2. A 9.5 μm thick CYTOP material with dielectric constant $\varepsilon = 2.1$ is negatively corona-charged to form an electret with a charge density $\sigma = -0.93$ mC/m^2. The two plates are separated by an air gap $g = 155$ μm. The experiment is then carried out by rotating one plate at a constant frequency f = 20 Hz. Table 3.2 summarizes the set of the parameters used in the experiment.

A finite element modeling and numerical methods are also conducted to simulate the performance of the microgenerator. The FEM capacitance of the microgenerator geometry is obtained and shown in Figure 3.9a. The maximum and minimum FEM capacitances are 0.14 pF and 2.18 pF, respectively. In this case, the parasitic capacitance induced by the microgenerator itself is very small. As reported in (Bartsch et al. 2009), an intrinsic capacitance is measured across the microgenerator and reported to be 15 pF. Hence, in the numerical simulation, this amount of stray capacitance is added to C_{par}.

The time average powers calculated using the analytical model presented in Section

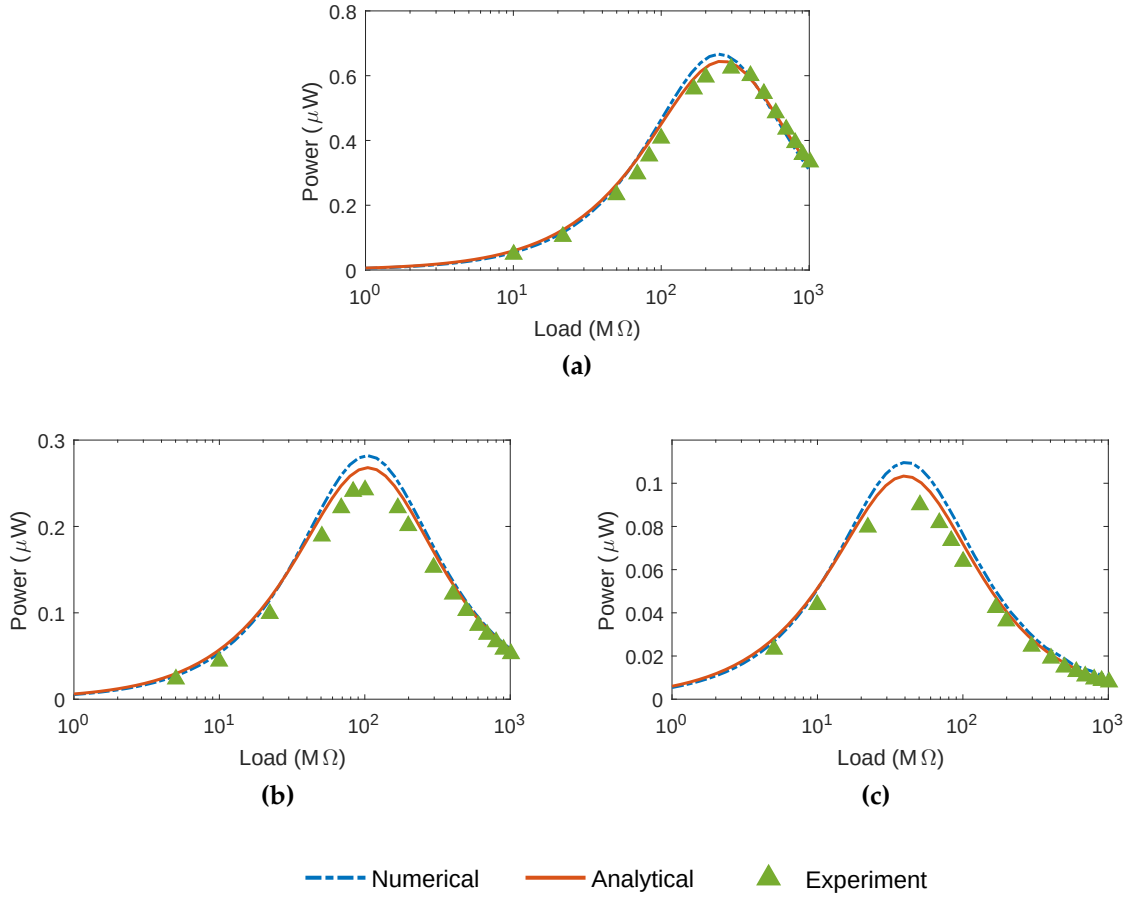

Figure 3.11. The output power of the analytical model is in good agreement with the simulated results and experimental data at various values of parasitic capacitances (a) 15 pF (b) 37 pF and (c) 97 pF.

3.3, the simulation and the experimental data extracted from (Bartsch et al. 2009) are plotted in Figure 3.11. The results show a good match between the calculated and the experimental performances of the microgenerator. The difference of the numerical simulation from the analytical model and experimental data is due to the approximation of FEM capacitances made in Subsection 3.2.3. Nevertheless, both the analytical model and numerical simulation can provide accurate prediction and hence, can be employed further to design and optimize the performance of the electret-based microgenerator.

The output voltage of the microgenerator is also essential in this validation. Figure 3.12 shows a good agreement between the analytical mode, numerical simula-

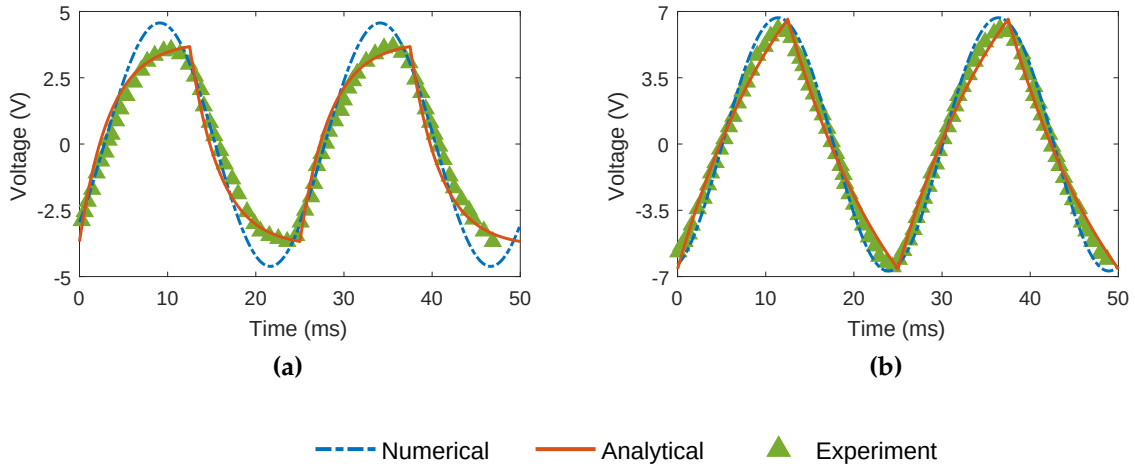

Figure 3.12. The output voltage generated from the microgenerator shows a good match between the analytical model, simulated results and experimental data at different values of load resistors (a) 50 MΩ and (b) 200 MΩ. Parasisitic capacitance used in the analytical model and simulation is 69 pF.

tion and experimental data at two different loads, 50 and 200 MΩ, using the same lumped parasitic capacitance $C_p = 69$ pF as in the experiment. One notable discrepancy is the degradation of the sharp peaks of the analytical model comparing with the rounded peaks of the numerical simulation and experimental data. This disagreement is due to the non-differentiation of the theoretical overlapping area at $t = \lambda T/2$, where λ is an integer, due to the definition of a triangle function presented in (3.17), while the numerical simulation with the approximation of C_{FEM} as a sinusoidal function is differentiable everywhere.

In summary, the developed analytical model provides good predictions compared to experimental data and simulated results. The simplicity of the model also provides insights into the microgenerator operating mechanism, making the model widely adopted as a general guidance in several studies and designs of electret-based microgenerators.

3.4 Conclusions

Based on the discussion presented in this chapter, high-performance electrets can be fabricated by selecting appropriate materials and forming methods. The state-of-the-art has shown that electrets, when being implemented into microgenerators, can efficiently harvest energy and produce an adequate amount of energy to power microelectronics. To understand the principle of operation for further analyses and optimizations, the electrodynamics of electret-based microgenerators that correlates the relative motion of the electrodes to the induced charges is derived. The performance of these small-scale devices can, therefore, be examined numerically by employing a simulation which uses FEM combined with numerical methods. However, the simulation-based approach requires an extensive FEM and numerical computation. More importantly, the numeric results at the output of these numerical solvers lack a fundamental understanding. As a result, an analytical modeling is more favorable. The last part of the chapter, therefore, presents an example of an analytical model formulation for a microgenerator under a constant-speed rotation which is the simplest form of external vibrations. More complicated types of excitations will be investigated and formulated in Chapters 4 and 5.

Chapter 4

Microgenerator modeling and optimization: small sinusoidal excitations

The analytical model presented in Section 3.3 has been employed in designing and optimizing the performance of several electret-based microgenerators to power microelectronic devices (Tsutsumino, Suzuki, Kasagi & Sakane 2006, Naruse et al. 2009, Masaki et al. 2011, Chen & Suzuki 2013, Nakano et al. 2015). However, the analytical model is applicable for constant-speed rotations only, while in practice, mechanical stimuli resemble sinusoidal vibrations. Consequently, a combination of finite element modeling and numerical methods presented in Subsection 3.2.3 has been the primary approach to analyze and optimize the performance of electret-based microgenerators. Both approaches are time-consuming, costly and more importantly, limit the understanding of design trade-offs involved.

In this chapter, a practical analytical model that accurately predicts the output voltage and effective power generated by electret-based microgenerators under small sinusoidal excitations is formulated. The proposed model is validated using numerical simulations that show a good agreement with measured results published in the literature. In addition, the effects of electret thickness, air gap spacing between the two plates of the microgenerator, and electret surface potential with respect to material properties are investigated using the proposed model to optimize the performance of the electret-based microgenerator.

The content of this chapter was reviewed and accepted for publication in the Journal of Microsystem Technologies.

4.1 Theoretical model

The governing equation of the microgenerators derived in Subsection 3.2.2 is repeated here for convenience

$$\frac{dQ(t)}{dt} = -\left[\frac{Q(t)}{R_L C_0}\frac{A_0}{A(t)} + \frac{V_0}{R_L}\right], \tag{3.8}$$

The induced charge $Q(t)$ in equation (3.8) relies on the instantaneous overlapping area $A(t)$, which depends on the type of the excitation. For a constant-speed rotation, within a half of a cycle, $A(t)$ is a linear function of time as defined in (3.17). Equation (3.8) can, therefore, be solved easily for a closed-form solution, while the situation is different for a sinusoidal function. Under a small sinusoidal excitation $x = X\sin\omega t$, where the amplitude X is smaller than the electrode width, W, the overlapping area is defined as

$$A(t) = kA_0|\sin\omega t| \qquad \text{where } k = \frac{X}{W} \leq 1. \tag{4.1}$$

The harmonic non-linear term associated with the overlapping $A(t)$ complicates the integration of the equation (3.8) and consequently, places a roadblock that prevents obtaining an analytical solution of the induced charge $Q(t)$. To overcome this difficulty, an approximation of the sinusoidal function in (4.1) using a parabolic function is utilised and can be expressed as

$$A(t) \approx kA_0\frac{4\omega t}{\pi}\left(1 - \frac{\omega t}{\pi}\right). \tag{4.2}$$

The dimensionless comparison between the two functions plotted in Figure 4.1 shows that the parabolic function can accurately approximate the sinusoidal variation of the overlapping area. In addition to simplify the analysis, the symmetry of the structure and the periodic nature of the excitation are utilized, so that, only the first half cycle of the vibration is investigated. Within this period, equation (3.8) is

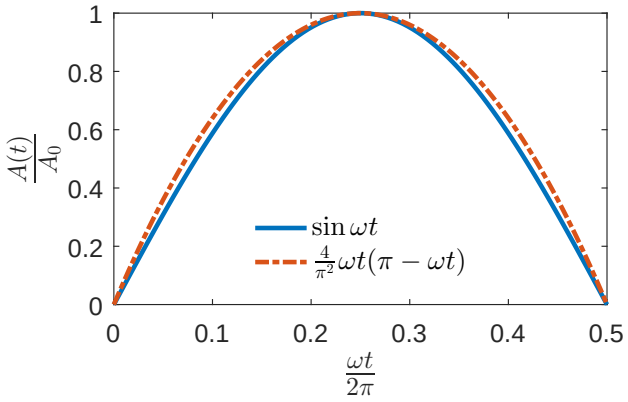

Figure 4.1. The sinusoidal variation of overlapping area can be well approximated by a parabolic function.

rewritten as

$$\frac{dQ(t)}{dt} = -\left[\frac{Q(t)}{4kR_LC_0\frac{\omega t}{\pi}\left(1-\frac{\omega t}{\pi}\right)} + \frac{V_0}{R_L}\right]. \tag{4.3}$$

We employ the integrating factor method to solve equation (4.3). Let $M(t)$ be a function such that

$$M(t) = \int_{\frac{\pi}{2\omega}}^{t} \frac{d\tau}{4kR_LC_0\frac{\omega\tau}{\pi}\left(1-\frac{\omega\tau}{\pi}\right)} = \frac{\pi}{4k\omega R_LC_0}\ln\left(\frac{\omega t}{\pi-\omega t}\right). \tag{4.4}$$

The integrating factor is then defined as

$$\exp\left[M(t)\right] = \exp\left[\frac{\pi}{4k\omega R_LC_0}\ln\left(\frac{\omega t}{\pi-\omega t}\right)\right] = \left(\frac{\omega t}{\pi-\omega t}\right)^{\frac{\pi}{4k\omega R_LC_0}}. \tag{4.5}$$

The solution of charge $Q(t)$ induced in the counter electrode of the microgenerator can be expressed by

$$\begin{aligned} Q(t) &= c_1\exp\left[-M(t)\right] + \exp\left[-M(t)\right]\int_0^t \exp\left[M(\tau)\right]\left(-\frac{V_0}{R_L}\right)d\tau \\ &= c_1\left(\frac{\pi-\omega t}{\omega t}\right)^{\frac{\pi}{4k\omega R_LC_0}} - \frac{V_0}{R_L}\left(\frac{\pi-\omega t}{\omega t}\right)^{\frac{\pi}{4k\omega R_LC_0}}\underbrace{\int_0^t\left(\frac{\omega\tau}{\pi-\omega\tau}\right)^{\frac{\pi}{4k\omega R_LC_0}}d\tau}_{N(t)}. \end{aligned} \tag{4.6}$$

Comparing with the results derived for a constant-speed rotation, the nonlinearity

of the parabolic-profile overlapping area leads to the complicated integral $N(t)$ presented in (4.6). According to the result (3.194-1) given in (Gradshteyn & Ryzhik 2014), $N(t)$ can be presented using a hypergeometric function ${}_2\mathrm{F}_1(a,b;c;z)$. Hypergeometric functions are a generalization of exponential functions that cannot be explicitly presented using elementary mathematical functions. However, the functions are well studied in the literature and can also be manipulated analytically. Here, we employ some derived properties of the functions to simplify and linearize the solution of equation (4.3) for further analysis.

We employ the result (3.194-1) in (Gradshteyn & Ryzhik 2014) to rewrite $N(t)$ as

$$N(t) = \frac{\pi}{\omega\left(1+\frac{\pi}{4k\omega R_L C_0}\right)}\left(\frac{\omega t}{\pi}\right)^{1+\frac{\pi}{4k\omega R_L C_0}} \times {}_2\mathrm{F}_1\left(\frac{\pi}{4k\omega R_L C_0}, 1+\frac{\pi}{4k\omega R_L C_0}; 2+\frac{\pi}{4k\omega R_L C_0}; \frac{\omega t}{\pi}\right). \tag{4.7}$$

We then use the Euler's transform of the hypergeometric function presented in (Weisstein 2002) to simplify further $N(t)$

$$N(t) = \frac{\pi}{\omega\left(1+\frac{\pi}{4k\omega R_L C_0}\right)}\left(\frac{\omega t}{\pi}\right)^{1+\frac{\pi}{4k\omega R_L C_0}}\left(1-\frac{\omega t}{\pi}\right)^{1-\frac{\pi}{4k\omega R_L C_0}} \times {}_2\mathrm{F}_1\left(1,2;2+\frac{\pi}{4k\omega R_L C_0}; \frac{\omega t}{\pi}\right). \tag{4.8}$$

Given $N(t)$ in (4.8), the solution of the charge $Q(t)$ in (4.6) can be expressed by

$$Q(t) = c_1\left(\frac{\pi-\omega t}{\omega t}\right)^{\frac{\pi}{4k\omega R_L C_0}} - \frac{4k\omega C_0 V_0 t}{4k\omega R_L C_0+\pi}\left(1-\frac{\omega t}{\pi}\right) \times {}_2\mathrm{F}_1\left(1,2;2+\frac{\pi}{4k\omega R_L C_0}; \frac{\omega t}{\pi}\right). \tag{4.9}$$

At time $t = 0$, there is no overlap between the two plates of the microgenerator, the induced charge $Q(0) = 0$, and therefore $c_1 = 0$. Here, it is more useful to consider the series expansion of the hypergeometric function specified in (Weisstein 2002) and

express $Q(t)$ as

$$\begin{aligned} Q(t) &= -\frac{4k\omega C_0 V_0 t}{4k\omega R_L C_0 + \pi}\left(1 - \frac{\omega t}{\pi}\right) \times {}_2\mathrm{F}_1\left(1, 2; 2 + \frac{\pi}{4k\omega R_L C_0}; \frac{\omega t}{\pi}\right) \\ &= -\frac{4k\omega C_0 V_0 t}{4k\omega R_L C_0 + \pi}\left(1 - \frac{\omega t}{\pi}\right) \times \left(1 + \frac{8k\omega R_L C_0}{8k\omega R_L C_0 + \pi}\frac{\omega t}{\pi} + \dots\right). \end{aligned} \tag{4.10}$$

For practical microgenerators, the maximum capacitance C_0 is only a few pF due to the micro scale of the generators, and the external load R_L varies in the range of MΩ. As a result, the value of $R_L C_0$ is very small (less than 10^{-5} s). In addition, the target of vibration energy harvesting is at low frequencies such as electrical powered machines (60 - 120 Hz (Roundy et al. 2003*a*)), human (less than 2.5 Hz (Hirasaki et al. 1999)) or animal motions (less than 3 Hz for sharks (Graham et al. 1990)). It is also worthy to note that k is less than or equals to 1. We can, therefore, employ the assumption of a very small $k\omega R_L C_0$ to approximate the hypergeometric function to the lowest order term and obtain the closed-form solution

$$Q(t) \approx -\frac{4k\omega C_0 V_0 t}{4k\omega R_L C_0 + \pi}\left(1 - \frac{\omega t}{\pi}\right). \tag{4.11}$$

The current $I(t)$ passing through the external load R_L can be calculated by employing the result obtained in (4.11) and expressed as

$$I(t) = -\frac{dQ(t)}{dt} = \frac{4k\omega C_0 V_0}{4k\omega R_L C_0 + \pi}\left(1 - \frac{2\omega t}{\pi}\right). \tag{4.12}$$

The output voltage $V(t)$ generated across the external load R_L between the two terminals of the microgenerator follows Ohm's law and therefore

$$V(t) = R_L\, I(t) = \frac{4k\omega R_L C_0 V_0}{4k\omega R_L C_0 + \pi}\left(1 - \frac{2\omega t}{\pi}\right). \tag{4.13}$$

We can now employ the results obtained in the formulations of current $I(t)$ and voltage $V(t)$ to model the generator using linear circuit elements. First, we investigate

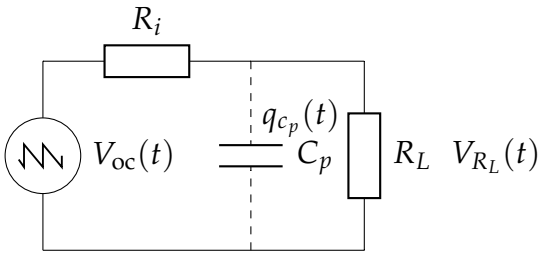

Figure 4.2. A cross-wafer microgenerator is modeled as a saw-tooth voltage source V_{oc} in series with an internal resistance R_i. Parasitic capacitance C_p is included to refine the model for practical microgenerators.

the two important characteristics of a generator: short circuit current and open circuit voltage. The short circuit current is determined as the external load is set to zero

$$I_{sc}(t) = \lim_{R \to 0} I(t) = \left(1 - \frac{2\omega t}{\pi}\right) \frac{4k\omega C_0 V_0}{\pi}. \tag{4.14}$$

The open circuit voltage is calculated as the external load R_L approaches infinity, which results in

$$V_{oc}(t) = \lim_{R \to \infty} V(t) = \left(1 - \frac{2\omega t}{\pi}\right) V_0. \tag{4.15}$$

The derivations in (4.14) and (4.15) results in a time independent ratio between the open circuit voltage and short circuit current, which is indeed the characteristic of a resistor. The microgenerator can, therefore, be modeled as a voltage source $V_{oc}(t)$ in series with an equivalent internal resistor R_i defined as

$$R_i = \frac{V_{oc}(t)}{I_{sc}(t)} = \frac{R_0}{8k}, \tag{4.16}$$

where R_0 is defined as

$$R_0 = \frac{1}{fC_0}, \tag{3.24}$$

and f is the frequency of the excitation.

Remark. *Under constant-speed rotations, a similar internal resistance for electret-based microgenerators is also observed in equation* (3.23)*. The two equivalent resistances are different*

Table 4.1. Analytical model of electret-based microgenerators under rotational and sinusoidal motions.

Excitation type	Analytical model	
	Voltage source	Internal resistance
Rotational	V_0	$\frac{R_0}{2n}$
Sinusoidal	$\left(1 - \frac{2\omega t}{\pi}\right) V_0$	$\frac{R_0}{8k}$

by a time-invariant factor which depends on the characteristics of excitations. Here, R_0 is directly analogous to the equivalent resistance of a switched capacitor C_0 at a switching frequency f as presented in (Franco 2002). Hence, a switched capacitor circuit can be used as an analogy to illustrate the operation mechanism of capacitive microgenerators.

Under constant-speed rotations, Bartsch et al. (2009) employed the result derived by Boland et al. (2003) to model the microgenerator as a constant voltage source in series with an internal resistor. In contrast, we modeled the microgenerator under a small sinusoidal excitation as a saw-tooth voltage source in series with an internal resistor, illustrated in Figure 4.2. Therefore, the dynamic behaviors of the microgenerator can be presented under the two different forms of excitations as shown in Table 4.1.

4.2 Influence of parasitic capacitance

Although the theoretical model can be used to guide the designs of electret-based microgenerators, Bartsch et al. (2009) highlight that unavoidable parasitic capacitances affects the performance of the microgenerator, causing discrepancy between modeled and measured performance. To take this capacitance into account, all load capacitances are absorbed into C_p connected in parallel to the external load R_L as shown in Figure 4.2.

The governing equation of the equivalent circuit in Figure 4.2, including C_p, des-

cribes the current flowing through C_p in term of the charge $q_{c_p}(t)$ stored in C_p

$$\frac{dq_{c_p}(t)}{dt} = \frac{1}{R_i}\left[V_{\text{oc}}(t) - \frac{q_{c_p}(t)}{C_p}\right] - \frac{q_{c_p}(t)}{R_L C_p}. \tag{4.17}$$

The boundary conditions are based on the periodic nature of the overlapping area in which the induced charge at the beginning of the cycle, $q_{c_p}(0)$, equals to the induced charged at the half of the excitation cycle, $q_{c_p}(\pi/\omega)$, expressed as

$$q_{c_p}(0) = q_{c_p}\left(\frac{\pi}{\omega}\right). \tag{4.18}$$

The solution of equation (4.17) can be obtained analytically in the first half cycle of the excitation. The output voltage across R_L equals to the voltage across C_p and is calculated as

$$V_{R_L}(t) = \frac{q_{c_p}(t)}{C_p} = \left[1 - \frac{2\omega t}{\pi} + \underbrace{\frac{2\omega R_p C_p}{\pi} + \frac{2e^{\frac{-t}{R_p C_p}}}{e^{\frac{-\pi}{\omega R_p C_p}} - 1}}_{\text{parasitic capacitance effect}}\right]\frac{R_L}{R_L + R_i}V_0, \tag{4.19}$$

where $R_p = R_L \| R_i$.

The effective power of the microgenerator can also be calculated as the average of instantaneous power

$$\begin{aligned} P &= \frac{\omega}{\pi R_L}\int_0^{\frac{\pi}{\omega}} V_{R_L}^2(t)\,dt \\ &= \frac{V_0^2 R_L}{(R_L + R_i)^2}\left[\frac{1}{3} + \frac{2\omega R_p C_p}{\pi}\left(\frac{2\omega R_p C_p}{\pi} - \frac{2}{e^{\frac{\pi}{\omega R_p C_p}} - 1}\right)\right]. \end{aligned} \tag{4.20}$$

4.3 Comparison between theory and simulation

The microgenerator reported in (Tsutsumino, Suzuki, Kasagi & Sakane 2006) is employed in this comparison. The device consists of two 20-by-10 mm^2 plates separated

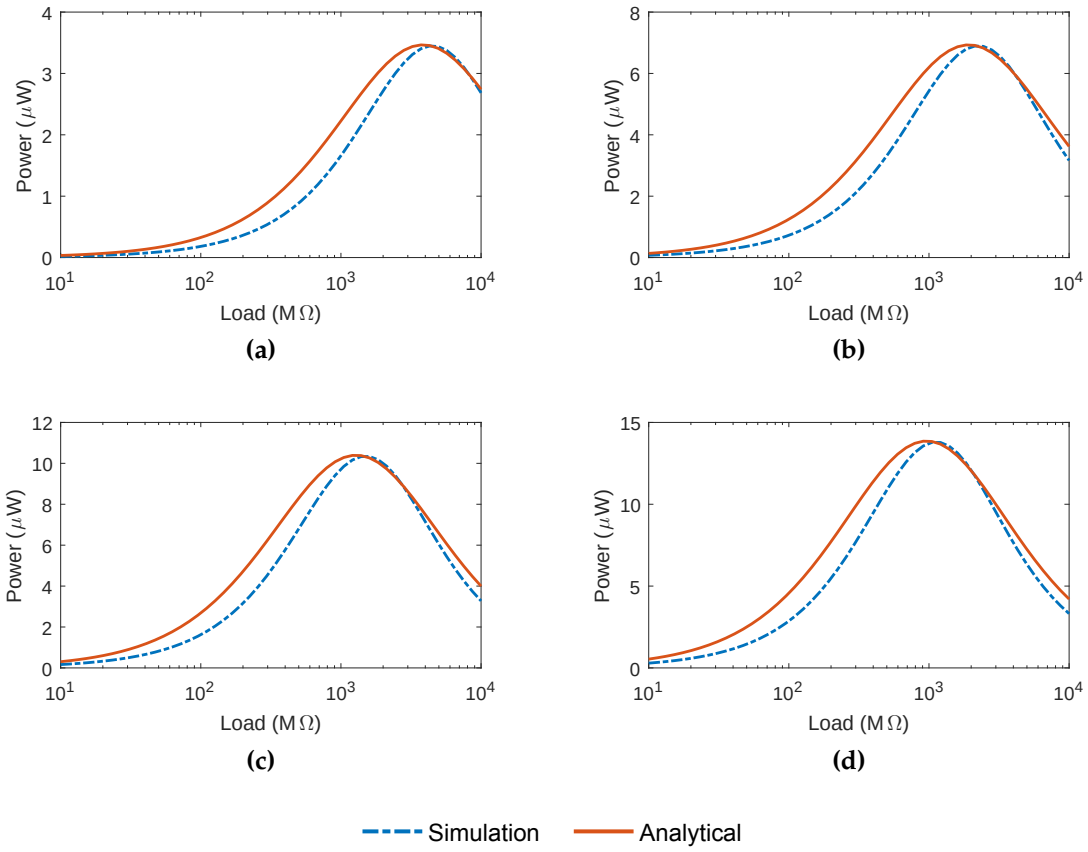

Figure 4.3. The effective power of the microgenerator predicted by the analytical model and the simulation at four different frequencies: (a) 5 Hz, (b) 10 Hz, (c) 15 Hz and (d) 20 Hz. C_p is evaluated as 2.27 pF.

by a 200 μm air gap. A 20 μm thick CYTOP with a total area of 100 mm^2 is deposited on 1 mm wide electrodes and then charged to -600 V. The microgenerator is tested under a 2 mm peak-to-peak excitation with several different frequencies. All parameters related to this microgenerator are summarized in Table 5.2. The output voltage and effective power of the microgenerator calculated employing our formulated solution presented in Section 4.2 is compared with the simulation based method described in Subsection 3.2.3.

In order to evaluate the analytical model, lumped parasitic capacitance C_p of the analytical solution must be determined. C_p can be obtained either by measuring physical devices and harvesting circuits, or fitting the analytical model to numerical simulations or experimental data. In this section,the latter approach is employed

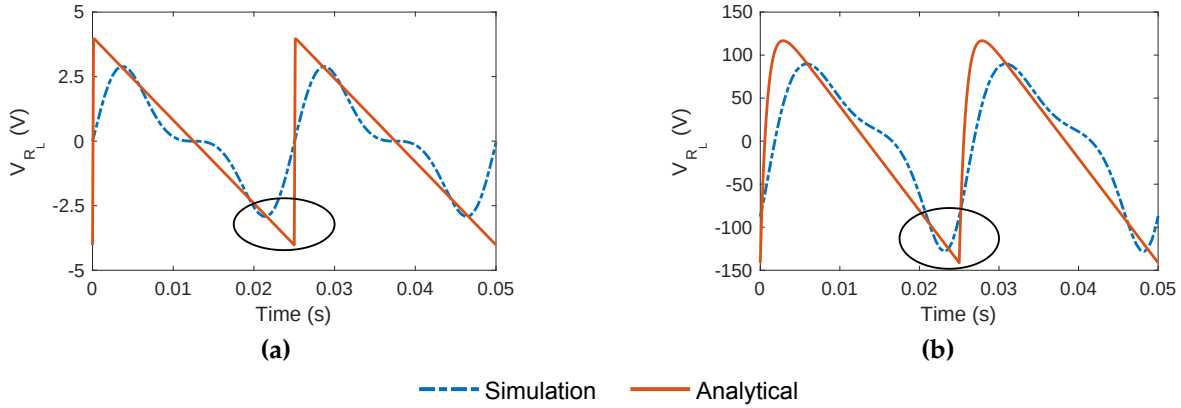

Figure 4.4. The output voltage of the microgenerator predicted by the analytical model and the simulation under two different loads: (a) 10 MΩ and (b) 500 MΩ at 20 Hz excitation. The shapes of the calculated and simulated signals are different due to the approximation of instantaneous overlapping area from a sinusoid to a parabolic function.

and a value of the lumped parasitic capacitance C_p is found to be 2.27 pF. For the numerical simulation, $C_{\max}$ and $C_{\min}$ are computed as 4.7 pF and 1.9 pF, respectively.

The generated powers of the microgenerator calculated using the closed-form expression given in equation (4.20) and the numerical simulation are shown in Figure 4.3. The analytical solutions are in good agreement with the simulation results and in particular the ability to predict the peak power. The discrepancy between the analytical model and numerical simulation is due to the approximation from a pure sinusoid to a parabolic function made in (4.2). Nevertheless, the analytical model can well predict the effective power and can facilitate the needed understanding for the

Table 4.2. Parameters used to compare the analytical model and simulation

Parameter	Description	Value
ε_d	Dielectric constant of CYTOP	2.1
n	Number of electrodes	10
W	Width of one electrode	1 mm
L	Out-of-plane length of one electrode	10 mm
d	Electret thickness	20 μm
g	Air gap between two plates	200 μm
V_0	Electret surface potential	600 V
X	Amplitude of excitation	1 mm
f	Forcing frequency	5, 10, 15 and 20 Hz

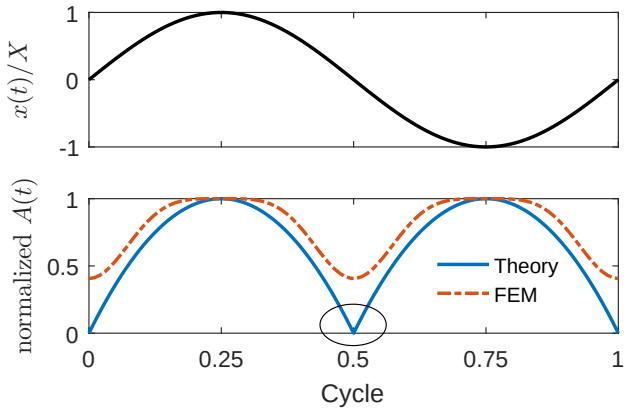

Figure 4.5. Theoretical overlapping area is non-differentiable when the counter electrode crosses origin, while the FEM overlapping area derived from C_{FEM} is a smooth curve. This factor attributes to the sharp peaks observed in the analytical output voltage presented in Figure 4.4.

design trade-offs and ideally optimization, due to the low computational overhead when compared to a full FEM approach.

To further evaluate the proposed model, its output voltage is compared with the numerical simulation. The output voltages plotted in Figure 4.4 at 10 MΩ and 500 MΩ shows an adequate prediction of the peak-to-peak voltages. The difference between the cotangent-like shape of simulated signal and the straightline response of the proposed model is due to the approximation made in (4.2). Another discrepancy is the sharp peaks of the analytical model as highlighted in both sub figures of Figure 4.4. This error is due to the non-differentiation of the theoretical overlapping area that occurs at every half cycle. As highlighted in Figure 4.5, the overlapping area defined in (4.2) is non-differentiable when the counter electrode crosses the origin point ($x = 0$), while the FEM overlapping area derived from C_{FEM} is differentiable everywhere in the time domain. The consequence of that non-differentiation causes spike shapes between the two half cycles in the proposed model, compared with rounded peaks in the FEM simulation.

Even though the non-linear electrodynamics of cross-wafer microgenerators under sinusoidal vibration complicates the analysis and prevents obtaining precise results, the presented model allows the prediction of the microgenerator performance

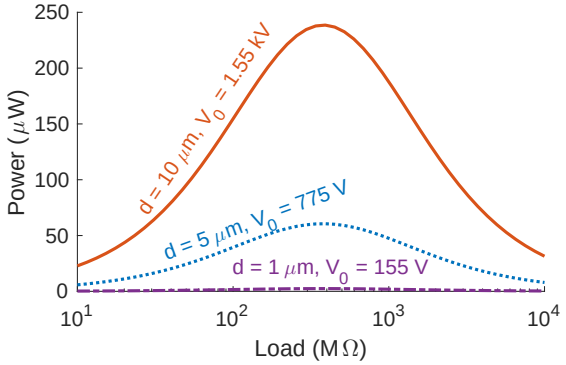

Figure 4.6. Various thicknesses of the electret and surface potentials corresponding to the dielectric strength are used to calculate the output power of the microgenerator. Owing to the limitation of internal breakdown effect, reducing the thickness of electret does not always improve the output power.

with reasonable accuracy, especially output power estimation. In the next section, we employ the proposed model to investigate design parameter influence on the performance of the electret-based microgenerators.

4.4 Optimization strategy

The common approaches to improve electret-based microgenerator performance are to: (*i*) increase the overlapping area A_0; (*ii*) decrease the thickness d of the electret; and/or (*iii*) reduce the air gap distance g between the two plates of the microgenerator. While a larger A_0 results in a larger device, reducing d or g is desirable since that can further shrink down the microgenerator volume. However, excessive reduction of d or g can be problematic due to the limitation of material breakdown caused by the electret's high surface potential voltage, V_0.

In this section, the analytical model developed in Section 4.2 is employed to optimize the performance of the electret-based microgenerator described in Table 4.2 with respect to the electret thickness d, the air gap spacing g, and the electret surface potential V_0 under practical limitations imposed by material properties.

Depending on the dielectric strength of electret material, reducing d can lead to the occurrences of internal breakdown. For example, the dielectric strength of Tef-

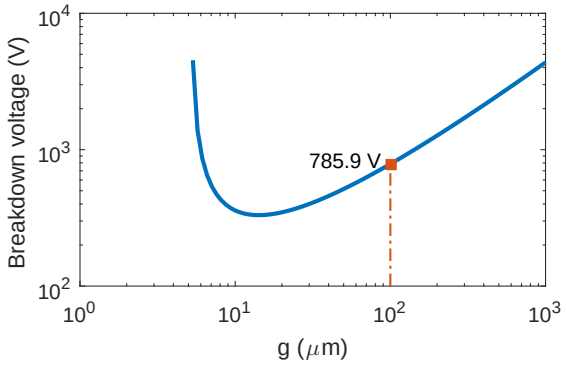

Figure 4.7. Breakdown voltage of air at atmospheric pressure. Data is taken from (Husain & Nema 1982).

lon PTFE, a widely used material to make electret, is about 155-200 MV/m (Smith 2013) which imposes a 155 V limit when using a 1-μm-thick film. Figure 4.6 plots the output power with various values of Teflon PTFE thickness and the corresponding breakdown voltage. Based on the result, decreasing the thickness d of the electret beyond a specific value might not result in an increase of the energy harvested. However, using a too thick electret film is also unfavorable since it would bring down the performance of the microgenerator. For a thin electret, Genter & Paul (2012) reported that a smaller d exacerbates charge decay. Based on their experimental result, a thickness between 11 - 23 μm was recommended to ensure charge stability while still obtaining a decent surface potential.

Reducing g also leads to another breakdown as described in Paschen's law. One example of external voltage breakdown in electret-based microgenerators was observed in (Tsutsumino, Suzuki, Kasagi & Sakane 2006) when a -950V pre-charged electret was employed to assemble a microgenerator with 100 μm air gap. According to Paschen's law for air at atmospheric pressure as presented in Figure 4.7, a maximum voltage difference of 785.9 V can be used at g = 100 μm to avoid the external breakdown (Husain & Nema 1982). Consequently, the surface potential of the electret in (Tsutsumino, Suzuki, Kasagi & Sakane 2006) was reported to drop to -400 V. One solution is to fill the gap with different dielectric media that has higher Paschen's dis-

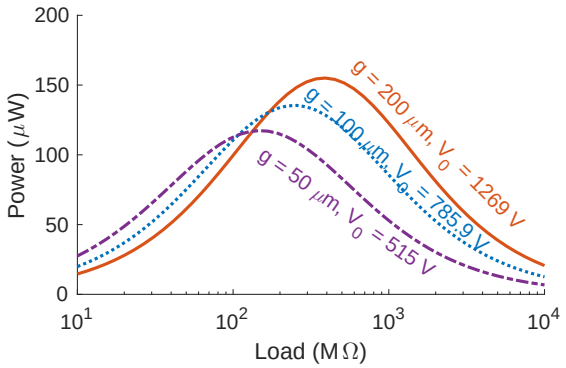

Figure 4.8. Various air gap distances and their corresponding Paschen's breakdown voltage are used to calculate the output power of the microgenerator. By including the effect of voltage breakdown, reducing g does not always result in a better performance.

charge voltage such as vacuum or insulating gas (SF_6 in (Tsutsumino, Suzuki, Kasagi, Kashiwagi & Morizawa 2006)). The downside of this method is the complication of the packaging process, resulting in a higher cost and lower yield. Nevertheless, air is still a preferable dielectric media due to the simplicity and economy of the packaging process.

Considering the effect of voltage breakdown on the microgenerator performance, the output power generated by the electret-based microgenerator with different values of g and the corresponding maximum allowable voltage according to Paschen's law is calculated and shown in Figure 4.8. The results show that a smaller g does not lead to a higher power harvesting. Hence, voltage breakdown effects should be considered carefully when designing and optimizing electret-based microgenerators.

By considering the dielectric strength of materials and voltage breakdown effects, the optimization of an electret-based microgenerator becomes a constrained

non-linear multi-variable problem expressed as

$$\max P \text{ such that } \begin{cases} 0 < V_0 \leq V_{\max} \\ d_{\min} \leq d \leq d_{\max} \\ g_{\min} \leq g \leq g_{\max} \\ R_{\min} \leq R_L \leq R_{\max} \\ V_0 \leq E_0\, d \\ V_0 \leq V_p(g) \\ f = f_0 \end{cases}, \tag{4.21}$$

where $V_{\max}$ is the maximum voltage that can be used to charge the electret, $d_{\min}$, $d_{\max}$, $g_{\min}$, $g_{\max}$, $R_{\min}$ and $R_{\max}$ are the lower and upper limits of electret thichkness, air gap spacing between the two plates of the microgenerator and the external load, respectively, E_0 is the dielectric strength of the electret material and $V_p(g)$ is a function that describes the correlation between the external breakdown voltage and the air gap g according to Paschen's law (Husain & Nema 1982).

For practical applications of electret-based microgenerators, $d_{\min}$ and $d_{\max}$ can be set to 1 μm and 100 μm, respectively. The lower and upper limits of air gap depends mostly on the standard processes used to assemble the microgenerator. For a practical MEMS process, $g_{\min}$ and $g_{\max}$ are set to 50 and 500 μm, respectively. $V_{\max}$ is assumed to be 1000 V which is achievable if employing corona discharge method. Teflon PTFE is assumed to be the electret material used in this study, and hence, the dielectric strength is $E_0 = 155$ MV/m. The external load is assumed to vary from $R_{\min} = 1$ MΩ to $R_{\max} = 1$ GΩ. The frequency of interest, f_0, is assumed to be 20 Hz in this optimization. In addition, there is a need to evaluate C_p to include in the optimization. Given that C_p is due to fringing effects at the edges of electrodes which is directly proportional to the FEM capacitance at zero overlapping $C_{\min}$, a numerical

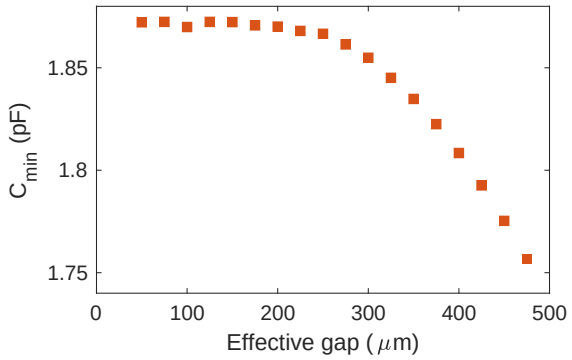

Figure 4.9. The variation of the minumum FEM capacitance C_{min} is insignificant (less than 0.15 pF) for various values of effective gap spacing $d/\varepsilon_d + g$.

study for C_{min} at various effective gap spacing $d/\varepsilon_d + g$ is performed and plotted in Figure 4.9. The results show only a slight variation of C_{min}, especially at gap spacing below 250 μm. As a result, the variation of C_p is neglected in this optimization.

Figure 4.10 shows the output power generated by the microgenerator as the volume constrained by the dielectric and Paschen's breakdown voltages. The result of the optimization using a non-linear program solver shows that an optimal output power of 61.7 μW can be obtained when

$$\begin{cases} d & = 6.5\ \mu m \\ g & = 143\ \mu m \\ V_0 & = 1000\ V \\ R_L & = 765\ \text{M}\Omega \end{cases}. \tag{4.22}$$

This results in 4 times higher power harvested when compared to the non-optimal structure described in Table 5.2.

As expected, the optimal power generated by the microgenerator requires a balance between the electret thickness d, the air gap g and the potential V_0 to ensure no material failure or discharging of the electret occur. In this case, $d = 6.5$ μm, $g = 143$ μm and $V_0 = 1000$ V satisfy all the requirements and result in the highest

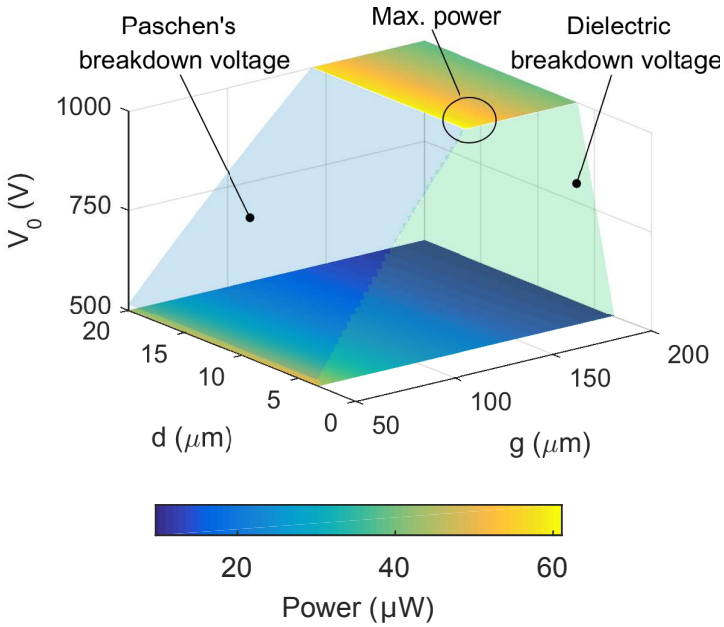

Figure 4.10. Output power generated by the electret-based microgenerator is plotted with respect to electret thickness d, air gap g and electret surface potential V_0 under a 2 mm peak-to-peak excitation at $f = 20$ Hz. Due to the Paschen's breakdown voltage presented as the transparent blue surface on the left and dielectric breakdown voltage presented as the transparent green surface on the right, a smaller d and g do not result in the highest output power. In this case, the maximum power is determined as 61.7 μW when d =6.5 μm, $g = 143$ μm and $V_0 = 1000$ V and $R_L = 765$ MΩ.

output power. This, again, emphasizes the importances of breakdown effects when optimizing electret-based microgenerator performance.

4.5 Conclusions

In summary, this chapter presents the formulation and development an analytical model for electret-based microgenerators excited under small sinusoidal vibrations. The effect of parasitic capacitances is also included into the model to accurately predict the performance of practical microgenerators. Under a considered condition, the electrodynamics of the microgenerators is equivalent to a sawtooth-signal voltage in series with an internal resistance. The developed model is validated using a simulation which combines FEM and numerical methods and shows a good agreement. In addition, the analytical model combined with voltage breakdown effects is employed

to demonstrate the importance of material properties when designing and optimizing electret-based microgenerators. Future work will focus on extending the capability of the model that can be used for an arbitrary sinusoidal excitation compared with a very limited assumption of small excitation amplitudes.

Chapter 5

Microgenerator modeling: general sinusoidal excitations

Chapter 4 presented the analytical model that described the dynamic behavior of electret-based microgenerators under sinusoidal excitations with small excitation amplitudes; however, in practice, large excitation amplitudes do also exist (Tsutsumino, Suzuki, Kasagi & Sakane 2006, Naruse et al. 2009, Chen & Suzuki 2013). The effect of multiple electrode crossing has been numerically investigated in the literature, however, with little in-depth insight into the operation mechanism of such devices (Renaud et al. 2015). As a result, this opens an interesting opportunity if the initially developed model can be extended further to take into consideration a general excitation amplitude and provide an accurate prediction of power and voltage generated by the microgenerator. Hence, in this chapter, a generalization of the model presented in Chapter 4 is formulated to highlight the stated opportunity.

This chapter is presented in a similar layout as Chapter 4. First, the theoretical model of the microgenerator under a general sinusoidal excitation is developed. The formulation also includes the linearization in order to model the microgenerator using circuit elements. Second, the effect of parasitic capacitances induced by harvesting circuitry and the microgenerator itself are included to provide an accurate prediction of the voltage and power generated at the output. Finally, the proposed model is validated using the numerical simulation presented in Subsection 3.2.3.

The content of this chapter was submitted for a journal publication.

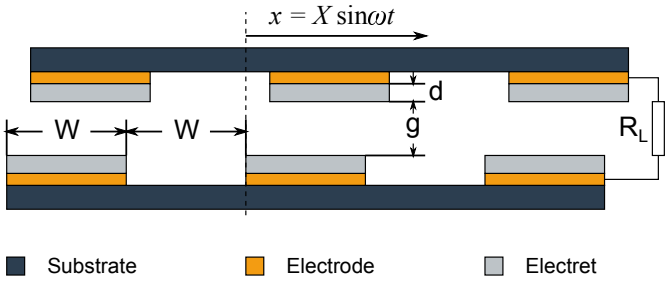

Figure 5.1. Schematic of an electret-based cross-wafer microgenerator.

5.1 Theoretical model

The electret-based microgenerator considered is a non-parametric structure in which the electrode width equals to the gap spacing between the two electrodes as illustrated in Figure 5.1. The governing equation of the microgenerator which correlates the relative movement of the counter electrodes to the charge induced was derived by Boland et al. (2003) is, again, repeated as

$$\frac{dQ(t)}{dt} = -\left[\frac{Q(t)}{R_L C_0}\frac{A_0}{A(t)} + \frac{V_0}{R_L}\right]. \tag{3.8}$$

Equation (3.8) shows a dependency of the induced charge $Q(t)$ on the instantaneous overlapping area $A(t)$, which is directly related to the type of external excitations. Therefore, to investigate the performance of the electret-based microgenerator, it is

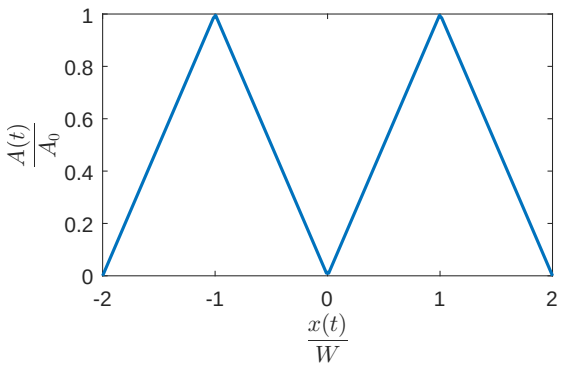

Figure 5.2. Instantaneous overlapping area $A(t)$ is a triangle wave with respect to the displacement $x(t)$.

essential to determine the correlation between the excitation $x(t)$ and instantaneous overlapping area $A(t)$. For the simplest case, which is a constant-speed rotation, the overlapping area is directly proportional to time and therefore, the solution of equation (3.8) can be easily obtained (Boland et al. 2003). For sinusoidal translations $x(t) = X \sin \omega t$, the correlation between $A(t)$ and $x(t)$ is a triangle wave shown in Figure 5.2, which is formulated as

$$A(t) = \frac{2A_0}{\pi} \left| \arcsin \left[\sin \left(\frac{\pi x(t)}{2W} \right) \right] \right|, \tag{5.1}$$

where W is the electrode width of the electret-based microgenerator. The absolute function is included in equation (5.1) to represent both the symmetry of the excitation and the non-negativity of instantaneous overlapping area $A(t)$. To investigate the performance of the electret-based microgenerator for a general value of k, a similar approach to the one considered in Section 4.1 is employed. The assumptions of periodic nature of the excitation and symmetry of the microgenerator are utilized, so that only a first half cycle of the excitation is analyzed. Within this time period, equation (5.1) can be represented using a piecewise function as follow

$$\frac{A(t)}{A_0} = \begin{cases} \dfrac{x(t)}{W} - 2m & \text{if} \quad 2m < \dfrac{x(t)}{W} \leq 2m+1 \\ 2m + 2 - \dfrac{x(t)}{W} & \text{if} \quad 2m+1 < \dfrac{x(t)}{W} \leq 2m+2, \end{cases} \tag{5.2}$$

where m is a natural number within $[0, k/2)$ and $k = X/W$ is the ratio between the maximum excitation amplitude and the electrode width.

For example, when $k \in (0, 1]$, which corresponds to the small amplitude excitation case, only one value of $m = 0$ is satisfied and the overlapping area can be expressed as

$$\frac{A(t)}{A_0} = \frac{x(t)}{W} = k \sin \omega t, \tag{5.3}$$

which is consistent with the result in equation (4.1). It is important to note that the

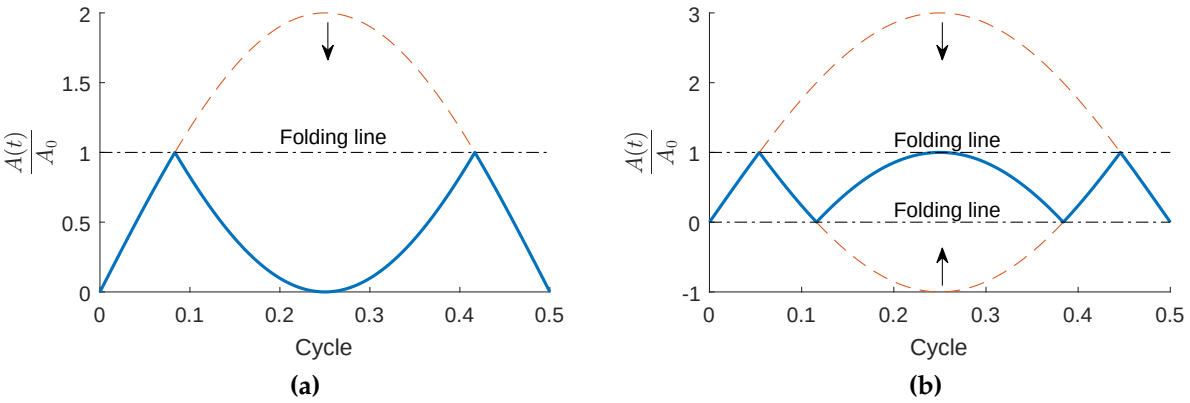

Figure 5.3. Instantaneous overlapping area is represented by a piecewise function which is analogous to a sinusoidal function folded into $(k-1)$ segments between 0 and 1 in the y-axis.

expression in (5.3) is not associated with an absolute operator as the one presented in equation (4.1) due to the assumption which considers only a first half cycle of the vibration. When $k \in (1,2]$, there is also one value of $m = 0$, but the overlapping area is a combination of two subfunctions given by

$$\frac{A(t)}{A_0} = \begin{cases} k \sin \omega t & \text{if} \quad 0 < \dfrac{x(t)}{W} \leq 1 \\ 2 - k \sin \omega t & \text{if} \quad 1 < \dfrac{x(t)}{W} \leq 2. \end{cases} \tag{5.4}$$

Table 5.1 provides a list of values of m and the number of subfunctions used to describe $A(t)$ under different values of k. In general, the shape of the overlapping area, in the time domain, is analogous to a sinusoidal function that is folded $(k-1)$ times between 0 and 1 as illustrated in Figure 5.3. As a result, $A(t)$ is a combination

Table 5.1. Example of range of m and the number of segments expressed the overlapping area $A(t)$ with different values of k.

k	Values of m	Number of subfunctions
1	0	1
2	0	2
3	0 and 1	3
4	0 and 1	4
5	0, 1 and 2	5

of $(2k-1)$ subfunctions.

For simplicity, the following analysis is carried out with integer values of k. Nonetheless, a non-integer k can also be analyzed by replacing the value k only in the superscript index notation presented in the following by the ceiling value of k, while all the calculations relate to k are unchanged.

The expression of $A(t)$ given in (5.2) is substituted into equation (3.8) to solve for the induced charge $Q(t)$. However, the non-linearity of the sinusoidal function associated with the overlapping area $A(t)$ complicates the solution and places a roadblock for a further analysis. To reduce the non-linearity and ease the analysis, one common approach is to approximate the sinusoidal function using a polynomial. The higher the order of the polynomial used, the more accurate the approximation. However, a too high order polynomial also accompanies a sophisticated solution and consequently, undesirable. As shown in Figure 4.1, within the first half cycle of the excitation, a sinusoidal function can be approximated using a second order polynomial, also known as a parabolic function presented as

$$\sin \omega t \approx \frac{4\omega t}{\pi}\left(1-\frac{\omega t}{\pi}\right). \tag{5.5}$$

Hence, equation (5.2) can be rewritten by replacing $x(t)$ by the parabolic function given in (5.5). The interval defining each subfunction of the piecewise function presented in (5.2) is also rewritten by solving the corresponding inequalities given in (5.2) and expressed in term of time instance t_j. The resulting overlapping area $A(t)$ is then given by

$$\frac{A(t)}{A_0} = \begin{cases} 4k\dfrac{\omega t}{\pi}\left(1-\dfrac{\omega t}{\pi}\right) - 2m & \text{if} \quad t_{2m} \le t < t_{2m+1} \quad \text{or} \quad t_{2k-2m} \le t < t_{2k+1-2m} \\ 2m+2-4k\dfrac{\omega t}{\pi}\left(1-\dfrac{\omega t}{\pi}\right) & \text{if} \quad t_{2m+1} \le t < t_{2m+2} \quad \text{or} \quad t_{2k-2m-1} \le t < t_{2k-2m}, \end{cases} \tag{5.6}$$

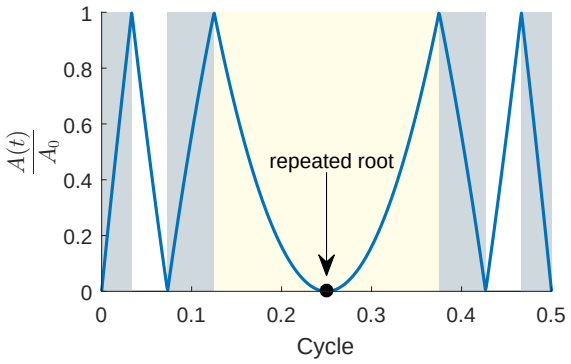

Figure 5.4. Illustration of different time intervals corresponding to different electrodynamic responses of the electret-based microgenerator.

where

$$t_j = \begin{cases} \tau_j & \text{if} \quad 0 \leq j \leq k \\ \dfrac{\pi}{\omega} - \tau_{2k+1-j} & \text{if} \quad (k+1) \leq j \leq (2k+1), \end{cases} \tag{5.7}$$

and τ_j is defined as

$$\tau_j = \left(1 - \sqrt{1 - \frac{j}{k}}\right) \frac{\pi}{2\omega}. \tag{5.8}$$

Here, t_j can also be understood as the time instance that satisfies $A(t_j) = 0$ or $A(t_j) = A_0$. The purpose of using the notation τ_j is to simplify the representation of the time instance t_j. Within each time interval $[t_j, t_{j+1}]$, $A(t)$ can be presented by one continuous subfunction. However, with such definition of the time instance t_j given in (5.7), there is a special case in which

$$t_k = t_{k+1} = \frac{\pi}{2\omega}. \tag{5.9}$$

This corresponds to the time instance at the middle cycle of the excitation and the duration of the time interval $[t_k, t_{k+1}]$ is, therefore, zero. As a result, the two time instances t_k and t_{k+1} are excluded from the following analysis. Thus, all of the notation indexes discussed later also exclude these two values.

The dynamic behavior of the microgenerator on each time interval as part of the overlapping area given in (5.6) is analyzed in the following sub-sections.

5.1.1 Time interval $t_{2m} \leq t < t_{2m+1}$ or $t_{2k-2m} \leq t < t_{2k+1-2m}$

Within this time interval, the overlapping area is defined according to equation (5.6). Equation (3.8) can, therefore, be written as

$$\frac{dQ_1(t)}{dt} = -\left[\frac{Q_1(t)}{kR_LC_0\left[\frac{4\omega t}{\pi}\left(1-\frac{\omega t}{\pi}\right)-\frac{2m}{k}\right]}+\frac{V_0}{R_L}\right]. \tag{5.10}$$

The induced charge $Q_1(t)$ can be solved by employing integrating factor method combined with the result 3.194-1 in (Gradshteyn & Ryzhik 2014) and the Euler's transform of hypergeometric functions in (Weisstein 2002). Further details of the solution are included in Appendix C.1. The solution of equation (5.10) can then be expressed as

$$\begin{aligned} Q_1(t) = \beta_1\left(\frac{t_{2k+1-2m}-t}{t-t_{2m}}\right)^{\gamma_{2m}} - \frac{V_0\,(t-t_{2m})\,(t_{2k+1-2m}-t)}{R_L(1+\gamma_{2m})(t_{2k+1-2m}-t_{2m})}\times \\ {}_2\mathrm{F}_1\left(1,2;2+\gamma_{2m};\frac{t-t_{2m}}{t_{2k+1-2m}-t_{2m}}\right), \end{aligned} \tag{5.11}$$

where β_1 is an arbitrary constant, ${}_2\mathrm{F}_1(a,b;c;z)$ is a hypergeometric function and

$$\gamma_j = \frac{\pi}{4k\omega R_LC_0\sqrt{1-\frac{j}{k}}}. \tag{5.12}$$

At time $t = t_{2m}$, there is no overlap between the two plates of the electret-based microgenerator and therefore, no charge is induced or $Q_1(t_{2m}) = 0$. This results in $\beta_1 = 0$ and a simpler solution is obtained. In spite of that, the non-linearity of the hypergeometric function in equation (5.11) is quite complicated and consequently, does not allow to model the microgenerator using linear circuit elements. Therefore, the series expansion of hypergeometric functions is utilized to linearize the solution for further analysis. By expanding the hypergeometric function in (5.11), the solution

of charge $Q_1(t)$ can be written as

$$\begin{aligned} Q_1(t) &= -\frac{V_0\,(t-t_{2m})\,(t_{2k+1-2m}-t)}{R_L(1+\gamma_{2m})(t_{2k+1-2m}-t_{2m})}\,{}_2\mathrm{F}_1\left(1,2;2+\gamma_{2m};\frac{t-t_{2m}}{t_{2k+1-2m}-t_{2m}}\right) \\ &= -\frac{V_0\,(t-t_{2m})\,(t_{2k+1-2m}-t)}{R_L(1+\gamma_{2m})(t_{2k+1-2m}-t_{2m})}\left[1+\frac{2}{2+\gamma_{2m}}\frac{t-t_{2m}}{t_{2k+1-2m}-t_{2m}}+\ldots\right]. \end{aligned} \tag{5.13}$$

Owing to the micro scale of the microgenerator, the system capacitance C_0 is small and often less than 10 pF. The external load R_L can vary from a few kΩ to a few hundred MΩ. In addition, the targeted vibration frequency from the application point of view is very low, which is in the order of 2 Hz for human motion (Yun et al. 2011). As a result, $\omega R_L C_0$ is very small, making the lowest order term in the series expansion become the dominant term. We can, therefore, approximate the hypergeometric function to the lowest order term to obtain a closed-form solution of induced charge $Q_1(t)$ as

$$Q_1(t) = -\frac{V_0\,(t-t_{2m})\,(t_{2k+1-2m}-t)}{R_L(1+\gamma_{2m})(t_{2k+1-2m}-t_{2m})}. \tag{5.14}$$

Given the induced charge in equation (5.14), the current passing through the external load and the output voltage can respectively be calculated as

$$I_1(t) = -\frac{dQ(t)}{dt} = \frac{\pi V_0}{\omega R_L(1+\gamma_{2m})(t_{2k+1-2m}-t_{2m})}\left(1-\frac{2\omega t}{\pi}\right) \tag{5.15}$$

$$V_1(t) = R_L I(t) = \frac{\pi V_0}{\omega(1+\gamma_{2m})(t_{2k+1-2m}-t_{2m})}\left(1-\frac{2\omega t}{\pi}\right). \tag{5.16}$$

We then investigate the two important characteristics of the microgenerator: short circuit current and open circuit voltage in order to utilize linear circuit elements to model the microgenerator. The short circuit current can be determined as the external load is set to zero, while the open circuit voltage is obtained when the load approaches infinity

$$I_{\mathrm{sc}_1}(t) = \lim_{R_L \to 0} I(t) = \frac{4k\omega C_0 V_0}{\pi}\left(1 - \frac{2\omega t}{\pi}\right) \tag{5.17}$$

$$V_{\mathrm{oc}_1}(t) = \lim_{R_L \to \infty} V(t) = \frac{V_0}{\sqrt{1 - \frac{2m}{k}}}\left(1 - \frac{2\omega t}{\pi}\right). \tag{5.18}$$

The results in (5.17) and (5.18) show that the short circuit current is directly proportional to the open circuit voltage, which represents the characteristic of a resistor. The microgenerator can, therefore, be modeled as a reverse-sawtooth voltage source $V_{\mathrm{oc}_1}(t)$ in series with an equivalent internal resistance R_{i_1} defined as

$$R_{\mathrm{i}_1} = \frac{V_{\mathrm{oc}_1}(t)}{I_{\mathrm{sc}_1}(t)} = \frac{\pi}{4k\omega C_0\sqrt{1 - \frac{2m}{k}}} = \frac{R_0}{8k\sqrt{1 - \frac{2m}{k}}}, \tag{5.19}$$

where $R_0 = 1/(fC_0)$.

Remark. *Again, as stated in Subsection 3.3.1 and Section 4.1, R_0 is a direct analogy to the equivalent resistance of a switch capacitor C_0 at a switching frequency f as presented in (Franco 2002). Therefore, the dynamic behavior of the electret-based microgenerator in this case is analogous to the operation mechanism of a switch capacitor.*

The equivalent circuit of the electret-based microgenerator is presented in Figure 5.5a. In addition, as $k \leq 1$ for the case of small amplitude excitations, m can only equal to 0, the open circuit voltage and the equivalent internal resistance reduce to

$$\begin{cases} V_{\mathrm{oc}_1}(t) = V_0\left(1 - \dfrac{2\omega t}{\pi}\right) \\ R_i = \dfrac{R_0}{8k}, \end{cases} \tag{5.20}$$

which is consistent with the results formulated in (4.15) and (4.16).

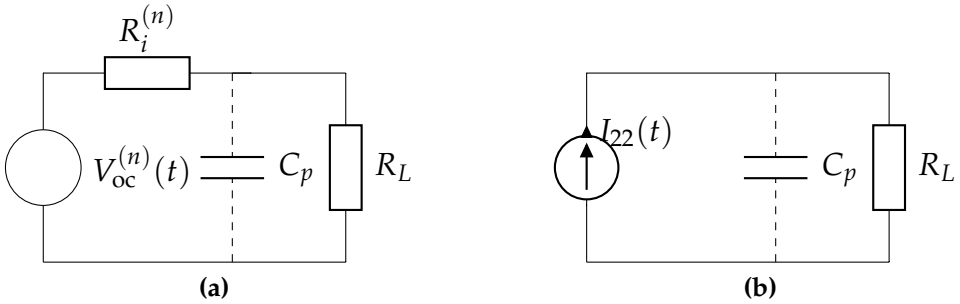

Figure 5.5. Under a sinusoidal excitation with angular frequency ω, an electret-based micro-generator can be modeled as (a) a voltage source in series with an internal resistance, or (b) a current source, depending on the analyzed time interval. Lumped parasitic capacitance C_p is added to refine the model for an accurate prediction.

5.1.2 Time interval $t_{2m+1} \leq t < t_{2m+2}$ or $t_{2k-2m-1} \leq t < t_{2k-2m}$

There is also a special case in the second subfunction of equation (5.6), which occurs when the ratio k is an even number. In this case, the overlapping area has a repeated time instances t_k and t_{k+1}, which is illustrated in Figure 5.4. As stated in the paragraph right after (5.9), these two time instances are excluded and the time interval considered will be $[t_{k-1}, t_{k+2}]$. In addition to these repeated time instances when k is an even number, the integration in the time interval $[t_{k-1}, t_{k+2}]$ illustrated as the yellow-shaded region in Figure 5.4 is different and therefore, is presented separately. In the following sections, the term "special case" indicates the time interval $[t_{k-1}, t_{k+2}]$ when k is even, while the "general case" will cover the rest.

General case

The overlapping area in this case corresponds to the non-highlighted regions shown in Figure 5.4. Within this time interval, the overlapping area is defined according to (5.6) and hence, equation (3.8) can be rewritten as

$$\frac{dQ_{21}(t)}{dt} = -\left[\frac{Q_{21}(t)}{kR_LC_0\left[\frac{2m+2}{k} - \frac{4\omega t}{\pi}\left(1 - \frac{\omega t}{\pi}\right)\right]} + \frac{V_0}{R_L}\right]. \tag{5.21}$$

Equation (5.21) can be solved using integrating factor method and the solution

can be expressed as

$$Q_{21}(t) = \beta_{21}\left(\frac{t - t_{2m+2}}{t - t_{2k-2m-1}}\right)^{\gamma_{2m+2}} - \frac{V_0\,(t - t_{2m+2})\,(t - t_{2k-2m-1})}{R_L(1+\gamma_{2m+2})(t_{2k-2m-1} - t_{2m+2})} \times {}_2F_1\left(1, 2; 2+\gamma_{2m+2}; \frac{t - t_{2k-2m-1}}{t_{2m+2} - t_{2k-2m-1}}\right). \tag{5.22}$$

The details of solving equation (5.21) can be found in Appendix C.2.

At time $t = t_{2k-2m-1}$, there is no area overlap, resulting in no charge induced and therefore, $\beta_{21} = 0$. Similar to the approach presented in Subsection 5.1.1, the hypergeometric function in equation (5.22) is approximated to the lowest order term for the given reasons to obtain the closed-form solution as

$$Q_{21}(t) = -\frac{V_0\,(t - t_{2m+2})\,(t - t_{2k-2m-1})}{R_L(1+\gamma_{2m+2})(t_{2k-2m-1} - t_{2m+2})}. \tag{5.23}$$

Given the closed-form solution of the induced charge $Q_{21}(t)$ in equation (5.23), the output current and voltage are respectively calculated as

$$I_{21}(t) = -\frac{dQ_{21}(t)}{dt} = \frac{-\pi V_0}{\omega R_L(1+\gamma_{2m+2})(t_{2k-2m-1} - t_{2m+2})}\left(1 - \frac{2\omega t}{\pi}\right) \tag{5.24}$$

$$V_{21}(t) = R_L I_{21}(t) = \frac{-\pi V_0}{\omega(1+\gamma_{2m+2})(t_{2k-2m-1} - t_{2m+2})}\left(1 - \frac{2\omega t}{\pi}\right). \tag{5.25}$$

The short circuit current and open circuit voltage of the electret-based microgenerator in this case can be written respectively as

$$I_{\mathrm{sc}_{21}}(t) = \lim_{R_L \to 0} I_{21}(t) = -\frac{4k\omega C_0 V_0}{\pi}\left(1 - \frac{2\omega t}{\pi}\right) \tag{5.26}$$

$$V_{\mathrm{oc}_{21}}(t) = \lim_{R_L \to \infty} V_{21}(t) = \frac{-V_0}{\sqrt{1 - \frac{2m+2}{k}}}\left(1 - \frac{2\omega t}{\pi}\right). \tag{5.27}$$

Similar to the result obtained in Subsection 5.1.1, the short circuit current given in (5.26) is directly proportional to the open circuit voltage given in (5.27), which is, again, the characteristic of a resistor. Hence, the microgenerator can be modeled as

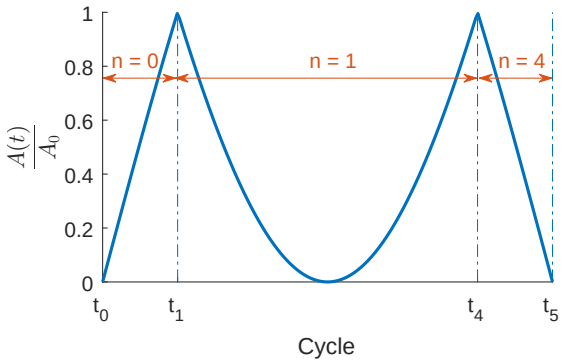

Figure 5.6. An illustration of the superscript n which corresponds to the time interval $[t_n, t_{n+1}]$ when $k = 2$. The indexes k and $(k+1)$ are excluded from the analysis.

a sawtooth voltage source $V_{\mathrm{oc}_{21}}(t)$ in series with an equivalent internal resistance R_{i_2} illustrated in Figure 5.5a, where

$$R_{\mathrm{i}_2} = \frac{R_0}{8k\sqrt{1 - \frac{2m+2}{k}}}. \tag{5.28}$$

To employ index-based notations to ease the further analysis, the internal resistances given in (5.19) and (5.28) can be rewritten as

$$R_i^{(n)} = \begin{cases} \dfrac{R_0}{8k\sqrt{1 - \frac{n+(n \bmod 2)}{k}}} & \text{when } 0 \leq n \leq k-1 \\ \dfrac{R_0}{8k\sqrt{1 - \frac{(2k-n)+[(2k-n) \bmod 2]}{k}}} & \text{when } (k+2) \leq n \leq 2k, \end{cases} \tag{5.29}$$

where mod is the modulo operator and the superscript (n) indicates that the variables are applicable in the time interval $[t_n, t_{n+1}]$ as illustrated in Figure 5.6. Here, the values k and $k+1$ are excluded from the superscript index (n). The voltage sources specified in (5.18) and (5.27) can be rewritten in a single form as

$$V_{\mathrm{oc}}^{(n)}(t) = (-1)^n \frac{8kR_i^{(n)}}{R_0} V_0 \left(1 - \frac{2\omega t}{\pi}\right). \tag{5.30}$$

Special case

In this case, k is an even number and therefore, there is an existing value of m such that $k = 2m + 2$, resulting in a repeated or double time instance that causes the overlapping area to be zero, illustrated as the yellow-shaded region shown in Figure 5.4. The time interval considered for this case is presented as

$$t_{k-1} \leq t \leq t_{k+2}. \tag{5.31}$$

Equation (3.8) is, therefore, simplified to

$$\frac{dQ_{22}(t)}{dt} = -\left[\frac{Q_{22}(t)}{kR_LC_0\left(1-\frac{2\omega t}{\pi}\right)^2} + \frac{V_0}{R_L}\right]. \tag{5.32}$$

The solution of induced charge $Q_{22}(t)$ can be expressed as

$$Q_{22}(t) = \beta_{22}e^{\frac{-\pi}{2k\omega R_LC_0\left(1-\frac{2\omega t}{\pi}\right)}} + \frac{\pi V_0}{2\omega R_L}\left(1-\frac{2\omega t}{\pi}\right) - \frac{V_0}{R_L}\frac{\pi^2 e^{\frac{-\pi}{2k\omega R_LC_0\left(1-\frac{2\omega t}{\pi}\right)}}}{4k\omega^2 R_LC_0}\mathrm{Ei}\left[\frac{\pi}{2k\omega R_LC_0\left(1-\frac{2\omega t}{\pi}\right)}\right], \tag{5.33}$$

where β_{22} is an arbitrary constant and $\mathrm{Ei}(z)$ is an exponential integral function. Appendix C.3 presents the detailed formulation of the solution of equation (5.32).

Owing to the continuity of the overlapping area in this time interval, the induced charge $Q_{22}(t)$ is also continuous. This continuity requires the equality of the left-handed limit to the right-handed limit, which can be expressed as

$$\lim_{t\to\left(\frac{\pi}{2\omega}\right)^-} Q_{22}(t) = \lim_{t\to\left(\frac{\pi}{2\omega}\right)^+} Q_{22}(t). \tag{5.34}$$

As a result of this continuity condition, $\beta_{22} = 0$.

The assumption of a very small ωR_LC_0 for practical microgenerator combined with the asymptotic representation of exponential integral function (Gradshteyn &

Ryzhik 2014, result 8.215) is utilized to present the solution of induced charge $Q_{22}(t)$ as

$$\begin{aligned} Q_{22}(t) &= \frac{\pi V_0}{2\omega R_L}\left(1-\frac{2\omega t}{\pi}\right) - \frac{V_0}{R_L}\frac{\pi^2}{4k\omega^2 R_L C_0}\frac{2k\omega R_L C_0\left(1-\frac{2\omega t}{\pi}\right)}{\pi}\times \\ &\quad \left[1+\frac{2k\omega R_L C_0\left(1-\frac{2\omega t}{\pi}\right)}{\pi}+2!\left(\frac{2k\omega R_L C_0\left(1-\frac{2\omega t}{\pi}\right)}{\pi}\right)^2+\dots\right] \\ &= -\frac{V_0}{R_L}\frac{\pi}{2\omega}\left(1-\frac{2\omega t}{\pi}\right)\left[\frac{2k\omega R_L C_0\left(1-\frac{2\omega t}{\pi}\right)}{\pi}+2!\left(\frac{2k\omega R_L C_0\left(1-\frac{2\omega t}{\pi}\right)}{\pi}\right)^2+\dots\right] \\ &\approx -2kC_0V_0\left(1-\frac{2\omega t}{\pi}\right)^2. \end{aligned} \tag{5.35}$$

Given the linearized solution give in (5.35), the electrical current passing through the external load, R_L, can be calculated and presented as

$$I_{22}(t) = -\frac{dQ_{22}(t)}{dt} = -\frac{4k\omega C_0 V_0}{\pi}\left(1-\frac{2\omega t}{\pi}\right). \tag{5.36}$$

The result in (5.36) shows that the output current is independent of the load resistance R_L, which is the characteristic of a current source. Therefore, the microgenerator, in this case, can be modeled as a current source $I_{22}(t)$ as shown in Figure 5.5b.

In summary, an electret-based microgenerator excited by a sinusoidal vibration can be modeled as a voltage source in series with an internal resistance as shown in Figure 5.5a. There is only one special case when k is an even number, the microgenerator can be modeled as a pure current source within the time interval $[t_{k-1}, t_{k+2}]$ as shown in Figure 5.5b.

5.2 Effect of parasitic capacitances

The theoretical model developed in Section 5.1 neglects the effect of parasitic capacitances due to harvesting circuit wiring and fringe capacitance within the micro-

generator itself. Those unavoidable capacitances attribute to a substantial loss of the energy harvested. Consequently, the performance of the microgenerator is reduced, resulting in a notable discrepancy between the theoretical model prediction and measured data (Bartsch et al. 2009). To accurately predict the performance of the electret-based microgenerator, parasitic capacitances are lumped into a single capacitance C_p connected in parallel with the external load, R_L, as shown in Figure 5.5. The governing equation of the circuit including C_p as shown in Figure 5.5a is given by

$$C_p \frac{dV_{R_L}^{(n)}(t)}{dt} = \frac{dV_{R_L}^{(n)}(t)}{R_p^{(n)}} - \frac{V_{oc}^{(n)}(t)}{R_L}, \tag{5.37}$$

where $R_p^{(n)} = R_L \parallel R_i^{(n)}$. The solution of equation (5.37) can be expressed by

$$V_{R_L}^{(n)}(t) = c^{(n)} e^{\frac{-t}{R_p^{(n)} C_p}} + \phi^{(n)}(t), \tag{5.38}$$

where $\phi^{(n)}(t)$ is the steady state response defined as

$$\phi^{(n)}(t) = \frac{(-1)^n 8k R_p^{(n)} V_0}{R_0} \left(1 - \frac{2\omega t}{\pi} + \frac{2\omega R_p^{(n)} C_p}{\pi}\right), \tag{5.39}$$

and $c^{(n)}$ is an arbitrary constant and will be determined using the boundary conditions presented in (5.43). The "arbitrary" in this context means time invariant.

For the special time interval $[t_{k-1}, t_{k+2}]$ when k is even, the microgenerator is equivalent to the circuit shown in Figure 5.5b in which the governing equation is given by

$$C_p \frac{dV_{R_L}^{(k-1)}(t)}{dt} + \frac{V_{R_L}^{(k-1)}(t)}{R_L} = I_{22}(t). \tag{5.40}$$

The solution of equation (5.40) can be presented as

$$V_{R_L}^{(k-1)}(t) = c^{(k-1)} e^{\frac{-t}{R_L C_p}} + \psi(t), \tag{5.41}$$

where

$$\psi(t) = -\frac{4k\omega R_L C_0 V_0}{\pi}\left(1 - \frac{2\omega t}{\pi} + \frac{2\omega R_L C_p}{\pi}\right), \tag{5.42}$$

and $c^{(k-1)}$ is similar to $c^{(n)}$, which is an arbitrary constant and will be determined when applying boundary conditions presented in (5.43).

To obtain a complete solution that includes the effect of parasitic capacitance C_p, the constants $c^{(n)}$ in equations (5.38) and $c^{(k-1)}$ in (5.41) must be determined by applying the condition of continuity of the output voltage $V_{R_L}^{(n)}(t)$, which means that $V^{(n)}(t_{n+1})$, the voltage at the end of the current time interval $[t_n, t_{n+1}]$, must equal to $V^{(n+1)}(t_{n+1})$, the voltage at the beginning of the next time interval $[t_{n+1}, t_{n+2}]$. In addition, the voltage at the end of the output cycle must be the same as the voltage at the beginning of the output cycle. These conditions can be mathematically presented as

$$\begin{cases} V_{R_L}^{(n)}(t_{n+1}) &= V_{R_L}^{(n+1)}(t_{n+1}), \qquad \text{where} \quad 0 \leq n \leq 2k-1 \\ V_{R_L}^{(0)}(0) &= V_{R_L}^{(2k)}\left(\frac{\pi}{\omega}\right). \end{cases} \tag{5.43}$$

Equation (5.43) results in a system of $(2k-1)$ linear equations in term of $c^{(n)}$ and can be presented as

$$\mathbf{Ac} = \mathbf{b}, \tag{5.44}$$

where $\mathbf{A}$ is a $(2k-1)$-by-$(2k-1)$ matrix, $\mathbf{c}$ is a vector containing $(2k-1)$ constants $c^{(n)}$, and $\mathbf{b}$ is a $(2k-1)$-dimensional vector. For a general case without the repeated time instances causing zero overlapping area, the matrix $\mathbf{A}$ is given in (5.45). Each row of the matrix $\mathbf{A}$ has only two non-zero elements, one is on the diagonal and one is next to the right of the diagonal. The last row is different, in which one element is still on the diagonal, while the other is in the first column. Here, it is important to note that the supercript indexes k and $(k+1)$ are excluded. That means the k-th row

has two elements with their respective superscript indexes are $(k-1)$ and $(k+2)$.

$$\mathbf{A} = \begin{bmatrix} e^{\frac{-t_1}{R_p^{(0)}C_p}} & -e^{\frac{-t_1}{R_p^{(1)}C_p}} & 0 & \dots & 0 \\ 0 & e^{\frac{-t_2}{R_p^{(1)}C_p}} & -e^{\frac{-t_2}{R_p^{(2)}C_p}} & \dots & 0 \\ \vdots & \vdots & \ddots & \vdots & \vdots \\ 0 & 0 & \dots & e^{\frac{-t_{2k}}{R_p^{(2k-1)}C_p}} & -e^{\frac{-t_{2k}}{R_p^{(2k)}C_p}} \\ -e^{\frac{-t_0}{R_p^{(0)}C_p}} & 0 & \dots & 0 & e^{\frac{-t_{2k+1}}{R_p^{(2k)}C_p}} \end{bmatrix}. \tag{5.45}$$

The general form of vector $\mathbf{b}$ is presented in (5.46). Similar to matrix $\mathbf{A}$, the element on the k-th row of vector $\mathbf{b}$ is the subtraction of two terms with their indexes as $(k+2)$ and $(k-1)$.

$$\mathbf{b} = \begin{bmatrix} \phi^{(1)}(t_1) - \phi^{(0)}(t_1) \\ \phi^{(2)}(t_2) - \phi^{(1)}(t_2) \\ \vdots \\ \phi^{(2k)}(t_{2k-1}) - \phi^{(2k-1)}(t_{2k-1}) \\ \phi^{(0)}(t_0) - \phi^{(2k)}(t_{2k}) \end{bmatrix}. \tag{5.46}$$

For the special case where the ratio k is an even number, the representation of the matrices $\mathbf{A}$ and $\mathbf{b}$ are slightly different from the general case given in (5.45) and (5.46). The only modification needed is in $(k-1)$-th and k-th rows as highlighted in (5.47), while the rest is unchanged.

$$\underbrace{\begin{bmatrix} e^{\frac{-t_{k-1}}{R_p^{(k-2)}C_p}} & -e^{\frac{-t_{k-1}}{R_p^{(k-1)}C_p}} & \dots \\ \dots & e^{\frac{-t_{k+2}}{R_p^{(k-1)}C_p}} & -e^{\frac{-t_{k+2}}{R_p^{(k+2)}C_p}} \end{bmatrix}}_{\text{general case}} \rightarrow \underbrace{\begin{bmatrix} e^{\frac{-t_{k-1}}{R_p^{(k-2)}C_p}} & -e^{\frac{-t_{k-1}}{R_L C_p}} & \dots \\ \dots & e^{\frac{-t_{k+2}}{R_L C_p}} & -e^{\frac{-t_{k+2}}{R_p^{(k+2)}C_p}} \end{bmatrix}}_{\text{special case}} \tag{5.47}$$

Given the exact result of the output voltage by solving the system of linear equation (5.44), the time average power can then be calculated as the total energy gene-

Table 5.2. Parameters of the device presented in (Tsutsumino, Suzuki, Kasagi & Sakane 2006) are used to validate the analytical model.

Parameter	Value
A_0	100 mm^2
W	0.5 mm
ε_d	2.1
V_0	-100 V
d	20 μm
g	100, 175 and 200 μm
f	20 Hz
X	1 and 1.5 mm

rated in each time interval divided by the output cycle, which can be presented as

$$P_{\text{avg}} = \frac{2}{T}\int_0^{\frac{T}{2}} \frac{\left[V_{R_L}^{(n)}(t)\right]^2}{R_L}\, dt, \tag{5.48}$$

where $T = 2\pi/\omega$ is the cycle of the excitation.

5.3 Validation and discussion

An electret-based microgenerator with the parameters shown in Table 5.2 is utilized to validate the proposed analytical model developed in Section 5.2. The device consists of two conductive plates separated by various values of air gap g as shown in Table 5.2. The out-of-plan length of the two plates is 10 mm. Each plate is etched and patterned with twenty 0.5-mm wide electrodes, resulting in an active overlapping area $A_0 = 100$ mm^2. A 20 μm thick electret made from Teflon PTFE with dielectric constant $\varepsilon = 2.1$ is corona-charged to obtain a surface potential of -100 V and attached to one plate. Sinusoidal vibrations with amplitudes equal to 1 and 1.5 mm, corresponding to $k = 2$ and $k = 3$, respectively, are applied to create relative motion between the two plates for electric power generation. The analytical results of the considered microgenerator are then calculated and compared with the numerical simulation results obtained from the finite element modeling (FEM) and numerical

methods presented in (Boisseau et al. 2010). The lumped parasitic capacitance C_p can be determined either by measuring the intrinsic capacitance of the energy harvesting system or fitting the numerical results of time average power. In this section, we employ the latter approach to obtain C_p as shown in Table 5.3. The values of the minimum and maximum capacitances, $C_{\min}$ and $C_{\max}$, used in the simulation are also summarized in Table 5.3.

Figure 5.7 shows the calculated time-average output power generated from the microgenerator using the proposed analytical model and the numerical simulation. In general, the analytical results are in good agreements with the numerical simulation, particularly, the ability to accurately predict the effective power peak generated from the microgenerator. The discrepancy between the analytical model and numerical simulation is mainly due to the approximation made in (5.5). At a small value of air gap, for example $g = 100$ μm as shown in Figure 5.7a and 5.7d, the analytical model can accurately predict the output power at low values of load resistance, while notable errors can be observed at larger values of R_L. This is consistent with the assumption of small $R_L C_0$ made in (5.14). As the air gap increases, the stray capacitances induced by fringing fields become more significant compared with the maximum overlapping capacitances. Since the developed analytical model does include the effect of parasitic capacitances presented in Section 5.2, the analytical results at higher C_p provide a more accurate prediction of the power peaks and the optimal load resistances as shown in Figure 5.7b - 5.7f. In practice, the parasitic capacitances induced by external

Table 5.3. Lumped capacitances used in the analytical calculation and FEM capacitances used in the numerical simulation under different air gap distances and k, units are in μm for air gap g and pF for capacitances.

g	$C_{\min}$	$C_{\max}$	C_p	
			$k = 2$	$k = 3$
100	1.92	8.58	3.0	0.2
150	1.89	6.02	3.15	1.8
200	1.87	4.70	3.5	2.7

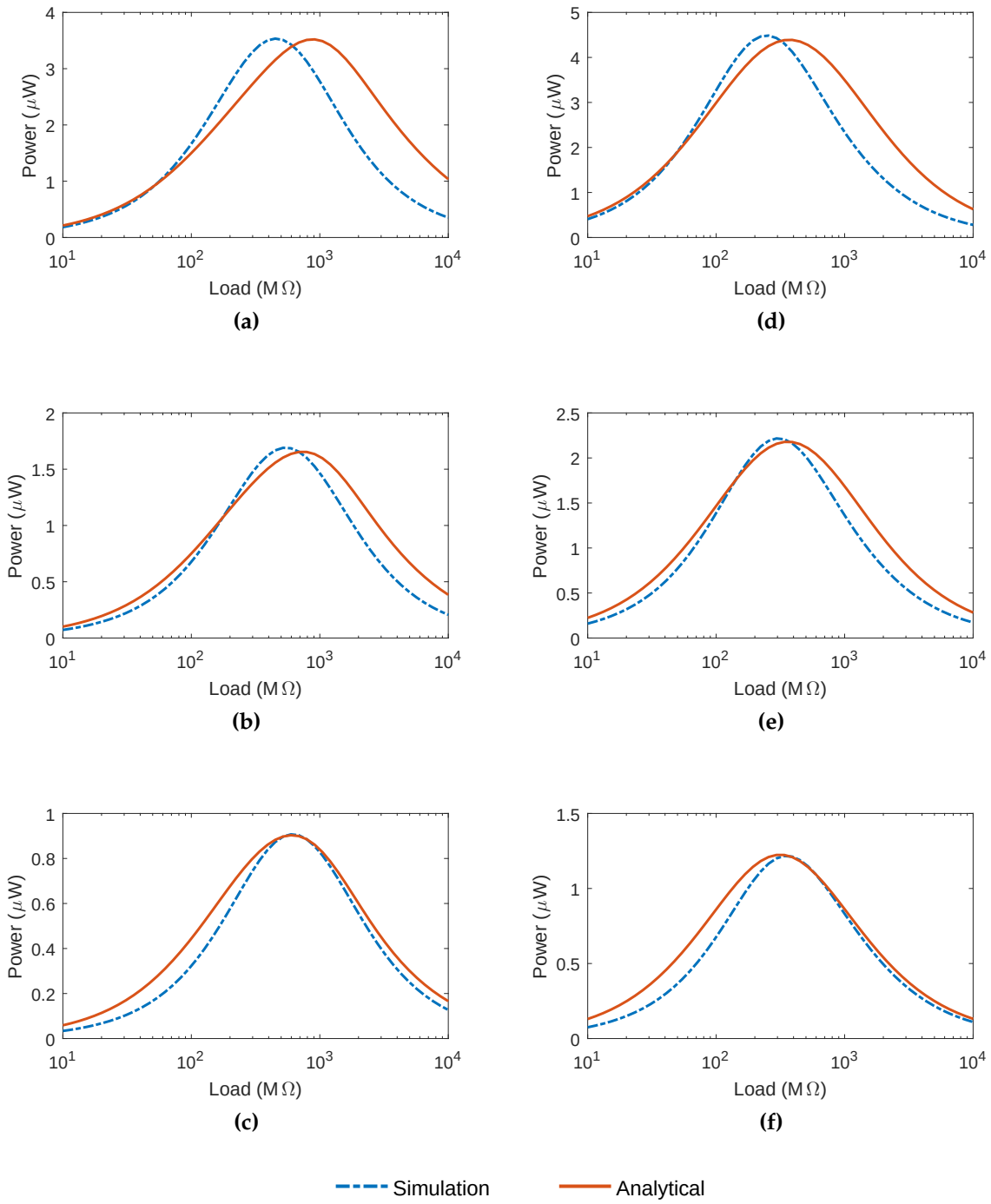

Figure 5.7. Output powers generated from the microgenerator using the analytical model are in good agreement with the simulation under various excitation amplitudes and air gap distances. The left figures are for $k = 2$, while the right ones are for $k = 3$. The air gap values from top row to bottom row are respectively 100, 150 and 200 μm.

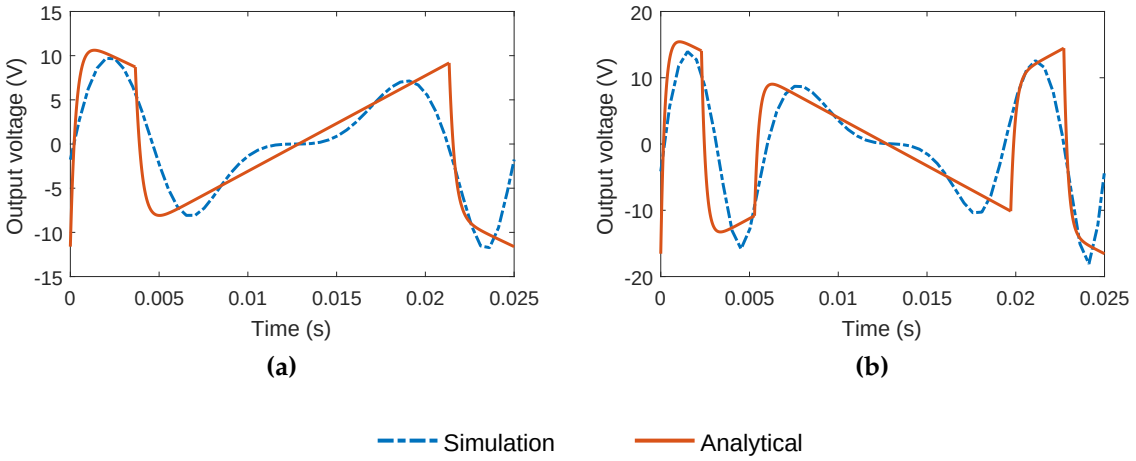

Figure 5.8. The calculated output voltage using the analytical model shows an adequate fit to the numerical simulation under two different excitation eamplitudes, (a) $k = 2$ and (b) $k = 3$, with the same load resistance $R_L = 100$ MΩ and the same air gap distance $g = 200$ μm. The discrepancy is due to the approximation from sinusoidal functions to parabolic functions and the linearization presented in Section 5.1.

harvesting circuitry and the microgenerator itself are often in the order to 10 pF, while the capacitances of microgenerators are only a few pF (Bartsch et al. 2009, Chen & Suzuki 2013). The analytical model is, therefore, capable of predicting the effective power generated from practical electret-based microgenerators.

The estimated output voltage obtained for the given microgenerator is also evaluated. The results in Figure 5.8 shows an adequate fit between the analytical model and the numerical simulation. The difference between the two signal shapes is, again, due to the approximation and the linearization made in Section 5.1. Another discrepancy is the sharp peaks of the output voltage at each time instance compared with the rounded curve of the numerical simulation. This mismatch is due to the non-differentiation of the theoretical overlapping area $A(t)$ at each time instance t_j in the analytical model as highlighted by the black circles shown in Figure 5.9. Nevertheless, the analytical model can provide a good prediction of the output voltage with reasonable accuracy.

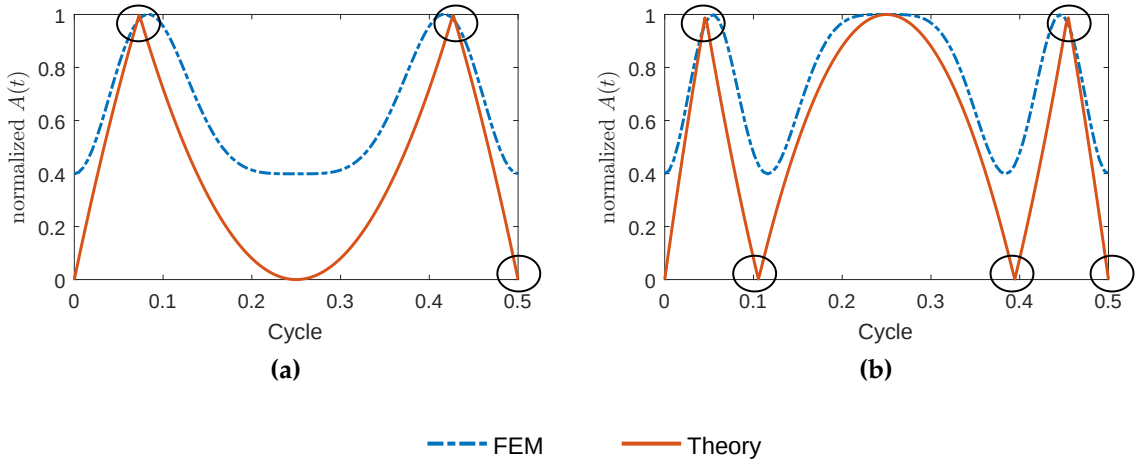

Figure 5.9. The non-differentitation of theoretical overlapping area highlighted in circles attributes to the discrepancy of sharp peaks in the analytical model comparing with smooth curve in the numerical simulation.

5.4 Conclusions

The generalized model presented in this chapter is more complicated than the simple case of small sinusoidal vibrations formulated in Chapter 4 due to the multi-electrode crossing effect. Hence, the instantaneous overlapping area cannot be described using a single function, but a piecewise function consist of several subfunctions. A similar modeling technique is then applied to different time intervals where the instantaneous overlapping area is represented by a single continuous function. Within these time intervals, the microgenerator can be modeled as a sawtooth voltage source in series with an equivalent resistance. There is a special time interval in which the microgenerator can be considered as a current source. Nonetheless, the significance of the analytical model is the in-depth insights into the operating mechanism and trade-off involved when designing an electret-based microgenerator.

Chapter 6

Conclusions and future works

6.1 Conclusions

This thesis has presented a novel approach to analytically model electret-based microgenerators under a sinusoidal translation - a practical excitation which is very close to ambient vibrations. The goal is to provide an understanding and insight into the operating mechanism and optimize the performance of these small-scale structures. There are two major contributions in this research.

First, the electrodynamics of electret-based microgenerators under the case of small sinusoidal excitations in which the vibration amplitude is smaller or equal to the width of an electrode. The modeling result shows that an electret-based microgenerator can be considered as a resistor in series with a sawtooth voltage source. The effect of parasitic capacitances induced by external harvesting circuitry and the microgenerator itself is then integrated into the model to obtain an accurate prediction of the output voltage and power. The analytical model is validated using a simulation which combines FEM and numerical methods published in the literature and shows a good agreement. In addition, the proposed model is then utilized and combined with the limitation of material properties, and voltage breakdown effect to optimize the power harvested at the output.

Second, the proposed model is then extended further and generalized to predict the electrodynamic behavior of electret-based microgenerators for an arbitrary sinusoidal vibration in which multiple electrode crossing might occur. A similar modeling approach to the previously developed model is then applied to model the microgenerator in different time intervals where the instantaneous overlapping area is a

continuous function. Within these time intervals, the electrodynamics of a microgenerator changes from a regular to a reverse sawtooth voltage source in series with an equivalent internal resistance or to a pure current source.

The research, however, has not presented an application of the generalized model. In addition, a fully functional microgenerator has yet been demonstrated. These are included in the future works.

6.2 Future works

Given these important understandings, the future works will focus on further optimizations, and hardware fabrications and integrations. These intended works are summarized as follows.

The first one is the optimization of ratio k which is the ratio between the excitation amplitude and the electrode width of a microgenerator. In the other words, given a fixed overlapping area and vibration amplitude, the idea is to determine the optimal number of electrodes to obtain the highest output power. One of the reasons for this work is the observation of the proportion of ratio k to the output power in the theoretical model for the case of a small sinusoidal excitation presented in Chapter 4. This means that as the number of electrodes increases, the theoretical output power might also increase. However, that also leads to an increase of stray capacitances induced by fringing fields at the edges of those electrodes. Hence, it is essential to find the optimal k that balances these effects.

The second work will focus more on hardware fabrications and experiments. The aim is to develop a liquid-based microgenerator employing the effect of the liquid sloshing phenomenon as presented in Appendix B. The reason is that the proposed concept can operate at very low-frequency excitations (2 - 5 Hz) (Choi et al. 2011) and provide a usable output voltage. The challenge is, however, the balance between the stability of charge retained in the electret and the amount of energy harvested at

the output. As reported by Wu et al. (2010), without coating an insulation layer on the bottom plate of a liquid-based microgenerator, the surface potential of the electret used exacerbates quickly, and consequently, shortens the operating lifetime. One of the solutions to overcome this problem is to introduce a 5-mm layer of parylene-C on the top surface of the bottom plate to prevent the charge decaying. The trade-off if using this solution is the reduction of system capacitance, resulting in a tiny power generated at the output. Thus, the question is to find a solution that maintaining the charges trapped inside the electret, while minimizing the impact to the output power.

Bibliography

Ahlbom, A., Bergqvist, U., Bernhardt, J., Cesarini, J., Grandolfo, M., Hietanen, M., Mckinlay, A., Repacholi, M., Sliney, D., Stolwijk, J. A. et al. (1998), 'Guidelines for limiting exposure to time-varying electric, magnetic, and electromagnetic fields (up to 300 GHz)', *Health physics* **74**(4), 494–521.

Akikur, R. K., Saidur, R., Ping, H. W. & Ullah, K. R. (2013), 'Comparative study of stand-alone and hybrid solar energy systems suitable for off-grid rural electrification: A review', *Renewable and Sustainable Energy Reviews* **27**, 738–752.

Aktakka, E. E., Kim, H. & Najafi, K. (2011), 'Energy scavenging from insect flight', *Journal of Micromechanics and Microengineering* **21**(9), 095016.

Akyildiz, I. F., Su, W., Sankarasubramaniam, Y. & Cayirci, E. (2002), 'Wireless sensor networks: a survey', *Computer networks* **38**(4), 393–422.

Altena, G., Renaud, M., Elfrink, R., Goedbloed, M., De Nooijer, C. & Van Schaijk, R. (2013), Design improvements for an electret-based mems vibrational electrostatic energy harvester, *in* 'Proc. PowerMEMS', p. 012078.

Amjadi, H. (1999), 'Charge storage in double layers of thermally grown silicon dioxide and APCVD silicon nitride', *IEEE Transactions on Dielectrics and Electrical Insulation* **6**(6), 852–857.

Arakawa, Y., Suzuki, Y. & Kasagi, N. (2004), Micro seismic power generator using electret polymer film, *in* 'Proc. PowerMEMS', Vol. 187, p. 17.

Arnold, D. P. & Wang, N. (2009), 'Permanent magnets for MEMS', *Journal of microelectromechanical systems* **18**(6), 1255–1266.

Ayala, I. N., Zhu, D., Tudor, M. J. & Beeby, S. P. (2009), Autonomous tunable energy harvester, *in* 'Proc. PowerMEMS', pp. 49–52.

Bartsch, U., Sander, C., Blattmann, M., Gaspar, J. & Paul, O. (2009), Influence of parasitic capacitances on the power output of electret-based energy harvesting generators, *in* 'Proc. PowerMEMS', pp. 332–335.

Basset, P., Galayko, D., Cottone, F., Guillemet, R., Blokhina, E., Marty, F. & Bourouina, T. (2014), 'Electrostatic vibration energy harvester with combined effect of electrical nonlinearities and mechanical impact', *Journal of Micromechanics and Microengineering* **24**(3), 035001.

Basset, P., Galayko, D., Paracha, A. M., Marty, F., Dudka, A. & Bourouina, T. (2009), 'A batch-fabricated and electret-free silicon electrostatic vibration energy harvester', *Journal of Micromechanics and Microengineering* **19**(11), 115025.

Beeby, S. P., ODonnell, T., Priya, S. & Inman, D. (2009), 'Electromagnetic energy harvesting', *Energy Harvesting Technologies* p. 129.

Beeby, S. P., Torah, R., Tudor, M., Glynne-Jones, P., O'donnell, T., Saha, C. & Roy, S. (2007), 'A micro electromagnetic generator for vibration energy harvesting', *Journal of Micromechanics and microengineering* **17**(7), 1257.

Beeby, S. P., Tudor, M. J. & White, N. M. (2006), 'Energy harvesting vibration sources for microsystems applications', *Measurement science and technology* **17**(12), R175.

Boisseau, S., Despesse, G. & Seddik, B. A. (2012), *Electrostatic conversion for vibration energy harvesting*, Intech.

Boisseau, S., Despesse, G. & Sylvestre, A. (2010), 'Optimization of an electret-based energy harvester', *Smart Materials and Structures* **19**(7), 075015.

Boland, J., Chao, Y.-H., Suzuki, Y. & Tai, Y. C. (2003), Micro electret power generator, *in* 'Proc. MEMS', pp. 538–541.

Boland, J., Messenger, J., Lo, K. & Tai, Y. (2005), Arrayed liquid rotor electret power generator systems, *in* 'Proc. MEMS', IEEE, pp. 618–621.

Broadhurst, M., Sessler, G., Davis, G., Gerhard-Multhaupt, R., Gross, B., Mascarenhas, S., Sessler, G., J., T. & West, J. (1987), *Electrets*, Springer Berlin Heidelberg.

Bu, L., Wu, X., Wang, X. & Liu, L. (2013*a*), 'Liquid encapsulated electrostatic energy harvester for low-frequency vibrations', *Journal of Intelligent Material Systems and Structures* **24**(1), 61–69.

Bu, L., Wu, X., Wang, X. & Liu, L. (2013*b*), 'Non-resonant electrostatic energy harvester for wideband applications', *Micro & Nano Letters* **8**(3), 135–137.

Chang, S., Yaul, F., Dominguez-Garcia, A., OSullivan, F., Otten, D. & Lang, J. (2009), Harvesting energy from moth vibrations during flight, *in* 'International Workshop on Micro and Nanotechnologies for Power Generation and Energy Conversion Applications', pp. 3–6.

Chen, R. & Suzuki, Y. (2013), 'Suspended electrodes for reducing parasitic capacitance in electret energy harvesters', *Journal of Micromechanics and Microengineering* **23**(12), 125015.

Ching, N. N., Wong, H. Y., Li, W. J., Leong, P. H. & Wen, Z. (2001), A laser-micromachined vibrational to electrical power transducer for wireless sensing systems, *in* 'Transducers 01 Eurosensors XV', Springer, pp. 38–41.

Chiu, Y. & Lee, Y.-C. (2012), 'Flat and robust out-of-plane vibrational electret energy harvester', *Journal of Micromechanics and Microengineering* **23**(1), 015012.

Choi, D.-H., Han, C.-H., Kim, H.-D. & Yoon, J.-B. (2011), 'Liquid-based electrostatic energy harvester with high sensitivity to human physical motion', *Smart Materials and Structures* **20**(12), 125012.

Cottone, F., Vocca, H. & Gammaitoni, L. (2009), 'Nonlinear energy harvesting', *Physical Review Letters* **102**(8), 080601.

Da Rosa, A. V. (2012), Fundamentals of renewable energy processes, Academic Press, chapter 5.

Dai, X., Miao, X., Sui, L., Zhou, H., Zhao, X. & Ding, G. (2012), 'Tuning of nonlinear vibration via topology variation and its application in energy harvesting', *Applied Physics Letters* **100**(3), 031902.

Defosseux, M., Allain, M., Defay, E. & Basrour, S. (2012), 'Highly efficient piezoelectric micro harvester for low level of acceleration fabricated with a cmos compatible process', *Sensors and Actuators A: Physical* **188**, 489–494.

Despesse, G., Jager, T., Jean-Jacques, C., Léger, J.-M., Vassilev, A., Basrour, S. & Charlot, B. (2005), Fabrication and characterization of high damping electrostatic micro devices for vibration energy scavenging, *in* 'Proc. Design, Test, Integration and Packaging of MEMS and MOEMS', pp. 386–390.

Dorf, R. C. (2003), *CRC handbook of engineering tables*, CRC Press. pg. 1-80.

Durou, H., Ardila-Rodriguez, G., Ramond, A., Dollat, X., Rossi, C. & Esteve, D. (2010), 'Micromachined bulk pzt piezoelectric vibration harvester to improve effectiveness over low amplitude and low frequency vibrations', *Proc. Power MEMS* pp. 27–30.

Edamoto, M., Suzuki, Y., Kasagi, N., Kashiwagi, K., Morizawa, Y., Yokoyama, T., Seki, T. & Oba, M. (2009), Low-resonant-frequency micro electret generator for energy harvesting application, *in* 'Proc. MEMS', IEEE, pp. 1059–1062.

Erturk, A., Hoffmann, J. & Inman, D. (2009), 'A piezomagnetoelastic structure for broadband vibration energy harvesting', *Applied Physics Letters* **94**(25), 254102.

Ferrari, M., Ferrari, V., Guizzetti, M., Marioli, D. & Taroni, A. (2008), 'Piezoelectric multifrequency energy converter for power harvesting in autonomous microsystems', *Sensors and Actuators A: Physical* **142**(1), 329–335.

Franco, S. (2002), *Design With Operational Amplifiers And Analog Integrated Circuits*, 3rd edn, McGraw-Hill, chapter 4, pp. 187–188.

Genter, S. & Paul, O. (2012), Parylene-C as an electret material for micro energy harvesting, *in* 'Proc. PowerMEMS', pp. 317–320.

Görge, G., Kirstein, M. & Erbel, R. (2001), 'Microgenerators for energy autarkic pacemakers and defibrillators: Fact or fiction?', *Herz* **26**(1), 64–68.

Gradshteyn, I. S. & Ryzhik, I. M. (2014), *Table of integrals, series, and products*, Academic press, chapter 3, p. 318.

Graham, J. B., DeWar, H., Lai, N., Lowell, W. R. & Arce, S. M. (1990), 'Aspects of shark swimming performance determined using a large water tunnel', *Journal of Experimental Biology* **151**(1), 175–192.

Green, M. A., Emery, K., Hishikawa, Y., Warta, W. & Dunlop, E. D. (2015), 'Solar cell efficiency tables (version 45)', *Progress in photovoltaics: research and applications* **23**(1), 1–9.

Harne, R. & Wang, K. (2013), 'A review of the recent research on vibration energy harvesting via bistable systems', *Smart materials and structures* **22**(2), 023001.

Harne, R. & Wang, K. (2016), 'Axial suspension compliance and compression for enhancing performance of a nonlinear vibration energy harvesting beam system', *Journal of Vibration and Acoustics* **138**(1), 011004.

Hirasaki, E., Moore, S. T., Raphan, T. & Cohen, B. (1999), 'Effects of walking velocity on vertical head and body movements during locomotion', *Experimental brain research* **127**(2), 117–130.

Hsieh, W. H., Hsu, T.-Y. & Tai, Y.-C. (1997), A micromachined thin-film Teflon electret microphone, *in* 'Proc. Transducers', Vol. 1, IEEE, pp. 425–428.

Huang, W.-S., Tzeng, K.-E., Cheng, M.-C. & Huang, R.-S. (2007), 'A silicon MEMS micro power generator for wearable micro devices', *Journal of the Chinese Institute of Engineers* **30**(1), 133–140.

Husain, E. & Nema, R. S. (1982), 'Analysis of Paschen curves for air, N2 and SF6 using the Townsend breakdown equation', *IEEE Transactions on Electrical Insulation* **EI-17**(4), 350–353.

Ibrahim, M. & Salehian, A. (2015), 'Modeling, fabrication, and experimental validation of hybrid piezo-magnetostrictive and piezomagnetic energy harvesting units', *Journal of Intelligent Material Systems and Structures* **26**(10), 1259–1271.

Jefimenko, O. D. & Walker, D. K. (1978), 'Electrostatic current generator having a disk electret as an active element', *IEEE Transactions on Industry Applications* (6), 537–540.

Jiang, Y., Masaoka, S., Fujita, T., Uehara, M., Toyonaga, T., Fujii, K., Higuchi, K. & Maenaka, K. (2011), 'Fabrication of a vibration-driven electromagnetic energy harvester with integrated NdFeB/Ta multilayered micro-magnets', *Journal of Micromechanics and Microengineering* **21**(9), 095014.

Kashiwagi, K., Okano, K., Miyajima, T., Sera, Y., Tanabe, N., Morizawa, Y. & Suzuki, Y. (2011), 'Nano-cluster-enhanced high-performance perfluoro-polymer electrets for energy harvesting', *Journal of Micromechanics and Microengineering* **21**(12), 125016.

Kim, H. S., Kim, J.-H. & Kim, J. (2011), 'A review of piezoelectric energy harvesting based on vibration', *International journal of precision engineering and manufacturing* **12**(6), 1129–1141.

Kiziroglou, M., He, C. & Yeatman, E. (2010), 'Flexible substrate electrostatic energy harvester', *Electronics letters* **46**(2), 166–167.

Lee, B., Lin, S., Wu, W., Wang, X., Chang, P. & Lee, C. (2009), 'Piezoelectric MEMS generators fabricated with an aerosol deposition PZT thin film', *Journal of Micromechanics and Microengineering* **19**(6), 065014.

Lee, J. M., Yuen, S. C., Li, W. J. & Leong, P. H. W. (2003), Development of an AA size energy transducer with micro resonators, *in* 'Proc. ISCAS.', Vol. 4, IEEE, pp. IV–IV.

Li, W. J., Wong, P. K., Chan, G. M. H. & Leong, P. H. W. (2000), 'A micromachined vibration-induced power generator for low power sensors of robotic systems', *Proc. World Automation Congress 8th International Symposium on Robotics with Applications* .

Liu, H., Lee, C., Kobayashi, T., Tay, C. J. & Quan, C. (2012), 'Piezoelectric MEMS-based wideband energy harvesting systems using a frequency-up-conversion cantilever stopper', *Sensors and Actuators A: Physical* **186**, 242–248.

Liu, H., Qian, Y. & Lee, C. (2013), 'A multi-frequency vibration-based MEMS electromagnetic energy harvesting device', *Sensors and Actuators A: Physical* **204**, 37–43.

Liu, J.-Q., Fang, H.-B., Xu, Z.-Y., Mao, X.-H., Shen, X.-C., Chen, D., Liao, H. & Cai, B.-C. (2008), 'A MEMS-based piezoelectric power generator array for vibration energy harvesting', *Microelectronics Journal* **39**(5), 802–806.

Lo, B. & Yang, G.-Z. (2005), Key technical challenges and current implementations of body sensor networks, *in* 'Proc. 2nd International Workshop on Body Sensor Networks'.

Lo, H.-W. & Tai, Y.-C. (2008), 'Parylene-based electret power generators', *Journal of Micromechanics and Microengineering* **18**(10), 104006.

Lo, H. W., Whang, R. & Tai, Y. C. (2007), A simple micro electret power generator, *in* 'Proc. MEMS', IEEE, pp. 859–862.

Mann, B. & Sims, N. (2009), 'Energy harvesting from the nonlinear oscillations of magnetic levitation', *Journal of Sound and Vibration* **319**(1), 515–530.

Masaki, T., Sakurai, K., Yokoyama, T., Ikuta, M., Sameshima, H., Doi, M., Seki, T. & Oba, M. (2011), 'Power output enhancement of a vibration-driven electret generator for wireless sensor applications', *Journal of Micromechanics and Microengineering* **21**(10), 104004.

McInnes, C., Gorman, D. & Cartmell, M. P. (2008), 'Enhanced vibrational energy harvesting using nonlinear stochastic resonance', *Journal of Sound and Vibration* **318**(4), 655–662.

Meninger, S., Mur-Miranda, J. O., Amirtharajah, R., Chandrakasan, A. & Lang, J. H. (2001), 'Vibration-to-electric energy conversion', *IEEE Transactions on Very Large Scale Integration (VLSI) Systems* **9**(1), 64–76.

Miao, P., Mitcheson, P., Holmes, A., Yeatman, E., Green, T. & Stark, B. (2006), 'MEMS inertial power generators for biomedical applications', *Microsystem Technologies* **12**(10-11), 1079–1083.

Mikeka, C. & Arai, H. (2011), Design issues in radio frequency energy harvesting system, *in* Y. K. Tan, ed., 'Sustainable Energy Harvesting Technologies - Past, Present and Future', InTech, chapter 10.

Miki, D., Honzumi, M., Suzuki, Y. & Kasagi, N. (2009), MEMS electret generator with electrostatic levitation, *in* 'Proc. of PowerMEMS', pp. 169–172.

Mitcheson, P. D., Yeatman, E. M., Rao, G. K., Holmes, A. S. & Green, T. C. (2008), 'Energy harvesting from human and machine motion for wireless electronic devices', *Proc. of the IEEE* **96**(9), 1457–1486.

Montecucco, A., Siviter, J. & Knox, A. R. (2014), 'The effect of temperature mismatch on thermoelectric generators electrically connected in series and parallel', *Applied Energy* **123**, 47–54.

Morimoto, K., Kanno, I., Wasa, K. & Kotera, H. (2010), 'High-efficiency piezoelectric energy harvesters of c-axis-oriented epitaxial pzt films transferred onto stainless steel cantilevers', *Sensors and Actuators A: Physical* **163**(1), 428–432.

Munson, B., Rothmayer, A. & Okiishi, T. (2012), Fundamentals of fluid mechanics, 7th edition, Wiley, chapter 2.

Mur-Miranda, J. O., Fanti, G., Feng, Y., Omanakuttan, K., Ongie, R., Setjoadi, A. & Sharpe, N. (2010), Wireless power transfer using weakly coupled magnetostatic resonators, *in* 'Energy Conversion Congress and Exposition (ECCE)', IEEE, pp. 4179–4186.

Nakano, J., Komori, K., Hattori, Y. & Suzuki, Y. (2015), MEMS rotational electret energy harvester for human motion, *in* 'Proc. PowerMEMS', p. 012052.

Naruse, Y., Matsubara, N., Mabuchi, K., Izumi, M. & Suzuki, S. (2009), 'Electrostatic micro power generation from low-frequency vibration such as human motion', *Journal of Micromechanics and Microengineering* **19**(9), 094002.

Ng, T. & Liao, W. (2005), 'Sensitivity analysis and energy harvesting for a self-powered piezoelectric sensor', *Journal of Intelligent Material Systems and Structures* **16**(10), 785–797.

Oliver, J. M. & Priya, S. (2010), 'Design, fabrication, and modeling of a four-bar electromagnetic vibration power generator', *Journal of Intelligent Material Systems and Structures* **21**(13), 1303–1316.

Paradiso, J. A. & Starner, T. (2005), 'Energy scavenging for mobile and wireless electronics', *IEEE Pervasive computing* **4**(1), 18–27.

Perez, M., Boisseau, S., Gasnier, P., Willemin, J., Geisler, M. & Reboud, J. (2016), 'A cm scale electret-based electrostatic wind turbine for low-speed energy harvesting applications', *Smart materials and structures* **25**(4), 045015.

Perez, M., Boisseau, S., Gasnier, P., Willemin, J. & Reboud, J. (2015), 'An electret-based aeroelastic flutter energy harvester', *Smart materials and structures* **24**(3), 035004.

Perpetuum (2013), 'Datasheet of energy harvesters PMG66001', https://perpetuum2016.files.wordpress.com/2016/09/perpetuum-ltd-vibration-energy-harvester-data-sheet-21october2013.pdf. [Online; accessed on May 29th, 2017].

Priya, S., Song, H.-C., Zhou, Y., Varghese, R., Chopra, A., Kim, S.-G., Kanno, I., Wu, L., Ha, D. S., Ryu, J. et al. (2017), 'A review on piezoelectric energy harvesting: materials, methods, and circuits', *Energy Harvesting and Systems* **4**(1), 3–39.

Renaud, M., Altena, G., Elfrink, R., Goedbloed, M., de Nooijer, C. & van Schaijk, R. (2015), 'Modeling and characterization of electret based vibration energy harvesters in slot-effect configuration', *Smart Materials and Structures* **24**(8), 085023.

Romero, E., Warrington, R. O. & Neuman, M. R. (2009), Body motion for powering biomedical devices, *in* 'Proc. EMBS', IEEE, pp. 2752–2755.

Roundy, S. & Wright, P. K. (2004), 'A piezoelectric vibration based generator for wireless electronics', *Smart Materials and structures* **13**(5), 1131–1142.

Roundy, S., Wright, P. K. & Rabaey, J. (2003*a*), 'A study of low level vibrations as a power source for wireless sensor nodes', *Computer communications* **26**(11), 1131–1144.

Roundy, S., Wright, P. K. & Rabaey, J. M. (2003*b*), Energy scavenging for wireless sensor networks, Springer, chapter 5.

Sakane, Y., Suzuki, Y. & Kasagi, N. (2008), 'The development of a high-performance perfluorinated polymer electret and its application to micro power generation', *Journal of Micromechanics and Microengineering* **18**(10), 104011.

Sari, I., Balkan, T. & Kulah, H. (2008), 'An electromagnetic micro power generator for wideband environmental vibrations', *Sensors and Actuators A: Physical* **145**, 405–413.

Sari, I., Balkan, T. & Külah, H. (2010), 'An electromagnetic micro power generator for low-frequency environmental vibrations based on the frequency upconversion technique', *Journal of Microelectromechanical Systems* **19**(1), 14–27.

Sessler, G. (1987), Physical principles of electrets, *in* 'Electrets', Springer, pp. 13–80.

Sessler, G. & West, J. (1972), 'Production of high quasipermanent charge densities on polymer foils by application of breakdown fields', *Journal of Applied Physics* **43**(3), 922–926.

Shahruz, S. (2006), 'Design of mechanical band-pass filters for energy scavenging', *Journal of Sound and Vibration* **292**(3), 987–998.

Smith, E. (2013), *Mechanical Engineer's Reference Book*, Elsevier Science, chapter 7, p. 7/126.

SolarPower Europe (2016), 'Global market outlook for solar power 2016-2020', https://resources.solarbusinesshub.com/solar-industry-reports/item/global-market-outlook-for-solar-power-2016-2020. [Online; accessed on April 22nd, 2017].

Sudevalayam, S. & Kulkarni, P. (2011), 'Energy harvesting sensor nodes: Survey and implications', *IEEE Communications Surveys & Tutorials* **13**(3), 443–461.

Suzuki, Y. (2011), 'Recent progress in MEMS electret generator for energy harvesting', *IEEJ Transactions on Electrical and Electronic Engineering* **6**(2), 101–111.

Tada, Y. (1986), 'Theoretical characteristics of generalized electret generator, using polymer film electrets', *IEEE transactions on electrical insulation* (3), 457–464.

Tada, Y. (1992), 'Experimental characteristics of electret generator, using polymer film electrets', *Japanese journal of applied physics* **31**(3R), 846.

Tanaka, H., Ono, G., Nagano, T. & Ohkubo, N. (2005), Electric power generation using piezoelectric resonator for power-free sensor node, *in* 'Proc. of Custom Integrated Circuits Conference', IEEE, pp. 97–100.

Tao, K., Ding, G., Wang, P., Yang, Z. & Wang, Y. (2012), Fully integrated micro electromagnetic vibration energy harvesters with micro-patterning of bonded magnets, *in* 'Proc. MEMS', IEEE, pp. 1237–1240.

Tao, K., Wu, J., Tang, L., Xia, X., Lye, S. W., Miao, J. & Hu, X. (2016), 'A novel two-degree-of-freedom MEMS electromagnetic vibration energy harvester', *Journal of Micromechanics and Microengineering* **26**(3), 035020.

Temme, N. (2011), Special functions: An introduction to the classical functions of mathematical physics, Wiley, chapter 5.

Tesla, N. (1897), 'System of transmission of electrical energy'. USPTO, US 645576 A.

Tsutsumino, T., Suzuki, Y., Kasagi, N., Kashiwagi, K. & Morizawa, Y. (2006), Micro seismic electret generator for energy harvesting, *in* 'Proc. PowerMEMS', pp. 279–282.

Tsutsumino, T., Suzuki, Y., Kasagi, N. & Sakane, Y. (2006), Seismic power generator using high-performance polymer electret, *in* 'Proc. MEMS', pp. 98–101.

Wang, N. & Arnold, D. P. (2009), Fully batch-fabricated MEMS magnetic vibrational energy harvesters, *in* 'Proc. PowerMEMS', pp. 348–351.

Weisstein, E. W. (2002), 'Hypergeometric function', From MathWorld - A Wolfram Web Resource. [Online; accessed on September 14th, 2016].

Williams, C. & Yates, R. B. (1996), 'Analysis of a micro-electric generator for microsystems', *Sensors and Actuators A: Physical* **52**(1), 8–11.

Wu, H., Tang, L., Yang, Y. & Soh, C. K. (2013), 'A novel two-degrees-of-freedom piezoelectric energy harvester', *Journal of Intelligent Material Systems and Structures* **24**(3), 357–368.

Wu, T., Suzuki, Y. & Kasagi, N. (2010), 'Low-voltage droplet manipulation using liquid dielectrophoresis on electret', *Journal of Micromechanics and Microengineering* **20**(8), 085043.

Xue, H., Hu, Y. & Wang, Q.-M. (2008), 'Broadband piezoelectric energy harvesting devices using multiple bimorphs with different operating frequencies', *IEEE transactions on ultrasonics, ferroelectrics, and frequency control* **55**(9).

Yang, B., Lee, C., Kotlanka, R. K., Xie, J. & Lim, S. P. (2010), 'A MEMS rotary comb mechanism for harvesting the kinetic energy of planar vibrations', *Journal of Micromechanics and Microengineering* **20**(6), 065017.

Yang, Z., Halvorsen, E. & Dong, T. (2014), 'Electrostatic energy harvester employing conductive droplet and thin-film electret', *Journal of Microelectromechanical Systems* **23**(2), 315–323.

Yang, Z., Wang, J. & Zhang, J. (2008), 'A micro power generator using PECVD SiO2/Si3N4 double layer as electret', *Proc. PowerMEMS* pp. 317–20.

Yang, Z., Wang, J. & Zhang, J. (2011), 'A high-performance micro electret power generator based on microball bearings', *Journal of Micromechanics and Microengineering* **21**(6), 065001.

Yen, B. C. & Lang, J. H. (2006), 'A variable-capacitance vibration-to-electric energy harvester', *IEEE Transactions on Circuits and Systems I: Regular Papers* **53**(2), 288–295.

Yun, J., Patel, S. N., Reynolds, M. S. & Abowd, G. D. (2011), 'Design and performance of an optimal inertial power harvester for human-powered devices', *IEEE Transactions on Mobile Computing* **10**(5), 669–683.

Zhang, Q. & Kim, E. S. (2015), 'Micromachined energy-harvester stack with enhanced electromagnetic induction through vertical integration of magnets', *Journal of Microelectromechanical Systems* **24**(2), 384–394.

Zhu, D., Tudor, M. J. & Beeby, S. P. (2009), 'Strategies for increasing the operating frequency range of vibration energy harvesters: A review', *Measurement Science and Technology* **21**(2), 022001.

Appendix A

Corona discharge station design

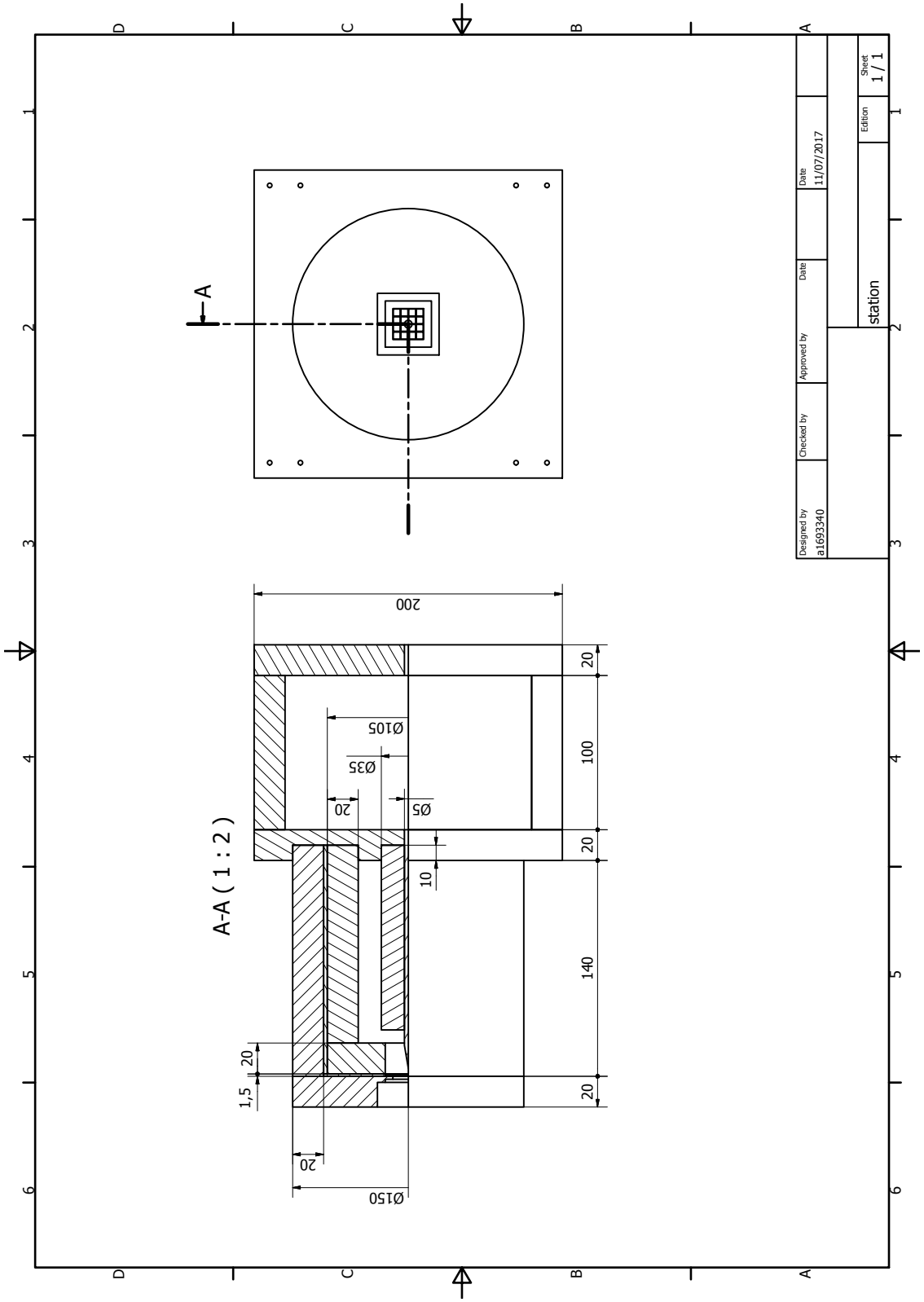

Appendix B

A liquid sloshing electret-based microgenerator

This chapter presents the design of an electret-based microgenerator employing a conductive liquid to vary the system capacitance for power generation. Matlab Simulink is employed to numerically simulate the performance of the microgenerator. The last part of the chapter outlines the fabrication of a prototype and a preliminary experiment result.

B.1 Concept of the microgenerator

The microgenerator proposed in this work is similar to the one presented in (Choi et al. 2011), except electret is used to initiate the power generation. The proposed microgenerator consists of two conductive plates with electret embedded onto one plate. The gap between the two plate is partially filled with a conductive liquid such as mercury or gallium or salt water (also known as sodium chloride). Figure B.1a illustrates the simplest design of the microgenerator in a planar configuration, which can operate efficiently under translational excitations or rotations along the out-of-plane axis.

The principle of the microgenerator operation is based on the sloshing phenomenon of the conductive liquid used, which acts as a flexible-shape electrode. At the initial state shown in Figure B.1a, the capacitance of the microgenerator is very low due to the presence of the air gap between the top plate and the conductive liquid,

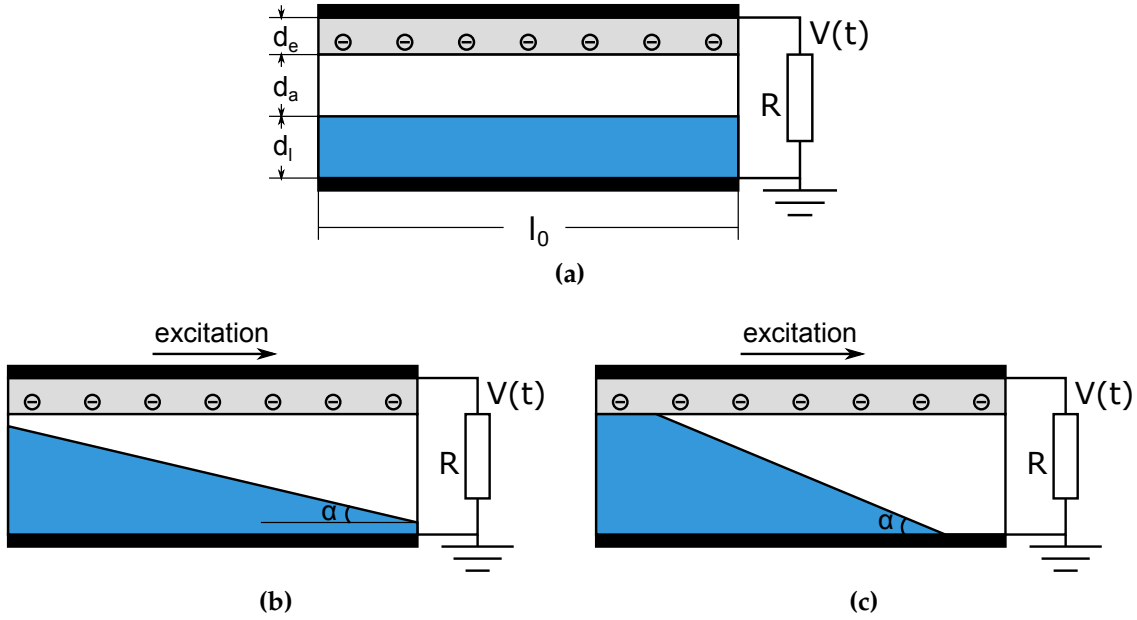

Figure B.1. The electret-based microgenerator proposed employs the sloshing phenominon of a conductive liquid to vary the system capacitance for power generation, (a) stationary condition, and the sloshing conditions, including (b) non-contact and (c) in contact with the electret.

presented as

$$C_{\text{init}} = \frac{\varepsilon\varepsilon_0 A_0}{d_e + \varepsilon d_a}, \tag{B.1}$$

where A_0 is the overlapping area between the two conductive plates, d_e is the thickness of the electret, d_a is the initial air gap, ε is the dielectric constant and ε_0 is the permittivity of free space.

Under a translational excitation or a rotation along the out-of-plane axis, the liquid sloshes back and forth as illustrated in Figure B.1b. As the liquid is in contact with the electret attached to the top plate as shown in Figure B.1c, the capacitance of the microgenerator becomes

$$C_{\text{contact}} = \frac{\varepsilon\varepsilon_0 (A_0 - A_{\text{contact}})}{d_e + \varepsilon(d_a + d_l)} + \frac{\varepsilon\varepsilon_0 A_{\text{contact}}}{d_e}, \tag{B.2}$$

where A_{contact} is the contact area between the conductive liquid and electret and d_l is

the thickness or height of the liquid at stationary condition.

One simple way to estimate the performance of the microgenerator is to consider the capacitance ratio between the initial and excited states. For simplicity, the electret thickness, d_e, is assumed to be very small compared with the initial air gap, d_a, and the liquid height, d_l. Given these assumptions, the capacitance ratio λ can, therefore, be expressed and simplified to

$$\lambda = \frac{C_{\text{contact}}}{C_{\text{init}}} \approx \frac{\varepsilon\varepsilon_0 A_{\text{contact}}}{d_e} \cdot \frac{d_a}{\varepsilon_0 A_0} \approx \frac{A_{\text{contact}}}{A_0} \frac{\varepsilon d_a}{d_e}. \tag{B.3}$$

While the ratio between A_{contact} and A_0 mostly depends on the excitation acceleration and the viscosity of the liquid used, the capacitance ratio, λ, can be increased further by designing a very small d_e compared with d_a. As reported in (Choi et al. 2011), under a 2.5 cm peak-to-peak acceleration at 5 Hz, a 1-cm^3 prototype with $d_e = 1$ μm resulted in $\lambda = 2000$, leading to a very high voltage potentially generated at the output.

The key point to achieve the potential capacitance change as reported is to ensure that the conductive liquid can be in contact with the electret. Without this condition, the capacitance variation is very small, resulting in a tiny power generated at the output. Hence, the microgenerator needs to be designed in such a way that allows the repeated occurrence of this event.

To gain more insights into the microgenerator performance, a combination of finite element modeling and numerical method is carried out in the following section to simulate the electrodynamics for output voltage and power prediction.

B.2 Simulation

The simulation described in this section is very similar to the one presented in Subsection 3.2.3. The principle of this simulation is to employ a finite element solver

to calculate the capacitance of the microgenerator at various values of displacement. The computed capacitance is then substituted into equation (3.11) to solve for the charge $Q(t)$ induced in the microgenerator electrode. Thus, the only change of this current simulation compared with the one presented in Subsection 3.2.3 is the capacitance computation due to the difference of the microgenerator geometry.

In general, Computational Fluid Dynamic (CFD) is the desirable tool to investigate the sloshing phenomenon of the liquid used. The resulting geometry of the free surface or the interface between the liquid and air is then entered into electrostatics finite element solver to calculate the capacitance of the microgenerator. Although the whole process can provide more accurate results, the utilization of CFD is complicated and requires extensive modeling and computation. Hence, to ease the analysis, the motion of the liquid is simplified to rigid-body motions (Munson et al. 2012, Section 2.12), in which the free surface is a straight line as illustrated in Figure B.1b. In addition, the effect of the collision when the liquid hits the electret on top is also ignored. In such situation, the slope of the free surface can be calculated as

$$\tan \alpha = -\frac{a_x}{g + a_y}, \tag{B.4}$$

where a_x, a_y are respectively the external accelerations applying on the x and y direction, g is the gravitational acceleration and α is the angle formed by the free surface and the horizontal axis. The minus sign indicates that the major mass of the liquid moves to the opposite direction of the input acceleration. In case of a pure horizontal translation excitation, there is no acceleration occur in the vertical direction, hence, $a_y = 0$.

Given the slope of the free surface, the angle at which the free surface starts to be in contact with the electret, α_{contact}, is an interest. Depending on the amount of the liquid filled in the microgenerator as illustrated in Figure B.2, the expression of

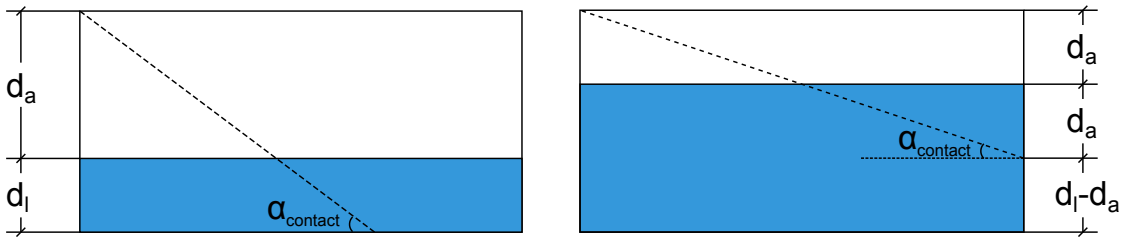

Figure B.2. Illustration of different scenarios where the liquid is filled with (a) less than half of the container, and (b) more than or equal to half of the container.

α_{contact} in term of the microgenerator's dimensions is different. In general, the expression of α_{contact} can be expressed as

$$\tan\left(\alpha_{\text{contact}}\right) = \begin{cases} \dfrac{d_a + \min(d_a, d_l)}{l_0} & \text{if} \quad d_a \leq d_l \\ \dfrac{(d_a + d_l)^2}{2 d_l l_0} & \text{if} \quad d_a > d_l \end{cases}, \tag{B.5}$$

where l_0 is the length of the microgeneration in the horizontal direction.

Given results in (B.4) and (B.5), the minimum acceleration required to enable the occurrence of the contacting state between the liquid and the electret is expressed as

$$a_{x-\text{contact}} = -g \tan(\alpha_{\text{contact}}). \tag{B.6}$$

To achieve a high variation of system capacitance or ensure the occurrence of the contacting state, at some time instance, the input acceleration must be greater than $a_{x-\text{contact}}$. In case of a sinusoidal excitation $x = X \sin \omega t$, the required condition becomes

$$\begin{aligned} &\max(|a_x|) > |a_{x-\text{contact}}| \\ \implies &\omega^2 X > g \tan(\alpha_{\text{contact}}). \end{aligned} \tag{B.7}$$

Hence, it is essential to appropriately design the microgenerator to meet the

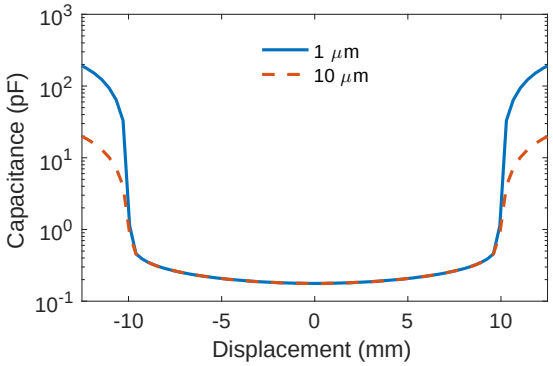

Figure B.3. FEM capacitances of the liquid based microgenerator under a 2.5-cm peak-to-peak vibration at 5 Hz with a 1 and 10 μm thick electrets made from Teflon PTFE.

required condition derived in (B.7) in order to enable the contacting state between the conductive liquid and the electret to obtain a high ratio of capacitance change, so that a higher performance can be achieved.

Given the considered assumptions, the simulation is undertaken on a 1-cm^3 microgenerator half-filled with a conductive liquid. Thin film electrets with different thicknesses are glued to one plate of the microgenerator and corona-charged to obtain a surface potential of -100 V. The microgenerator is then undergone a 2.5-cm peak-to-peak translation excitation at 5 Hz. In this case, the maximum acceleration of the external vibration is 12.3 m/s^2, while the minimum acceleration required to enable the contacting state is 9.81 m/s^2. Hence, the condition given in (B.7) is satisfied.

The simulation procedure is similar to the one in 3.2.3. The geometry of the microgenerator at different angle α is generated in a finite element solver to compute the capacitances between the two plates. At each value of α, the FEM capacitance is recorded and plotted in Figure B.3 as a function of translational displacement x. The conversion from α to x is done by employing the relation given in (B.4) combined with

$$a_x = -\omega^2 x. \tag{B.8}$$

Figure B.3 shows the capacitances when using two different electret thicknesses, 1 and 10 μm obtained from the FEM solver. At a displacement less than 1 cm, the liquid is not in contact with the electret, and hence, the capacitance variation is almost flat. However, when the displacement is larger than 1 cm, the contact between the liquid and electret is observed, resulting in a very large capacitance change. The ratio between the maximum and minimum capacitances of the 1 μm PTFE film is 1130, which is reasonable with the result reported by (Choi et al. 2011). The difference between the FEM value and the measurement result reported in (Choi et al. 2011) is due to the difference of materials used. If a material with a higher dielectric is used, for example when $\varepsilon = 7$, a ratio of up to 3000 can be obtained. Although a thin electret film is desirable to achieve a higher power generated, it complicates the fabrication processes, especially for a quick prototype. A too thin film also has a potential of reliability for a long term operation due to wearing. However, as the thickness of the electret increases, the maximum capacitance is decreased, while the minimum capacitance is unchanged as shown in Figure B.3. As a result, a small ratio of capacitances is observed, leading to a reduction of power generated at the output. Hence, the choice of electret thickness needs to balance all of these concerns, power and reliability. Another important note is the irregular shape of the capacitance, which cannot be approximated using a sinusoidal function as the one presented in Subsection 3.2.3. The simulation is, therefore, carried out by using linear interpolation to represent the value of FEM capacitances.

The simulation is implemented into Matlab Simulink as shown in Figure B.4 to solve for the output voltage across the external load R_L. A sub program is also included in the simulation to determine when the system reaches steady state. The obtaining output voltage is then used to compute the root-mean-square (RMS) voltage V_{rms}. Finally, the time average power is calculated following the same formula given in (3.15).

Figure B.5 shows the result of time average power under a 2.5 cm peak-to-peak

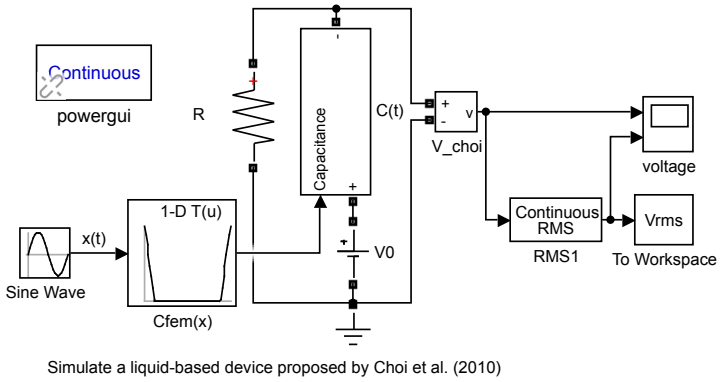

Figure B.4. The Matlab Simulink-based model of the liquid-sloshing microgenerator with 100 V per-charged electret under 2.5 cm peak-to-peak vibration at 5 Hz.

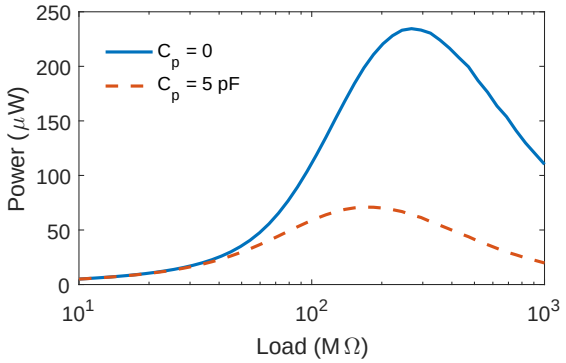

Figure B.5. Time average output power of the liquid microgenerator with 1-μm thick PTFE electret with and without the effect of parasitic capacitances induced by external harevsting circuitry.

translational excitation at 5 Hz. Owing to the high capacitance ratio, the liquid-based microgenerator can generate more than 200 μW. However, as a 5 pF lumped parasitic capacitance is added to simulate the effect induced by external harvesting circuitry, the power is reduced to 168 μW; nonetheless, this amount of power generated is still sufficient to power microelectronic devices.

The output voltage is also analyzed and shown in Figure B.6a. The shape of the output voltage is similar to a sawtooth signal presented in Chapter 4. The hypothesis for this signal shape is the parabolic-like capacitance variation of the microgenerator in the time domain as shown in Figure B.6b, and hence, the output signal can be approximated as a sawtooth shape following the formulation presented in Chapter 4. The horizontal line with zero volt represents the non-contact

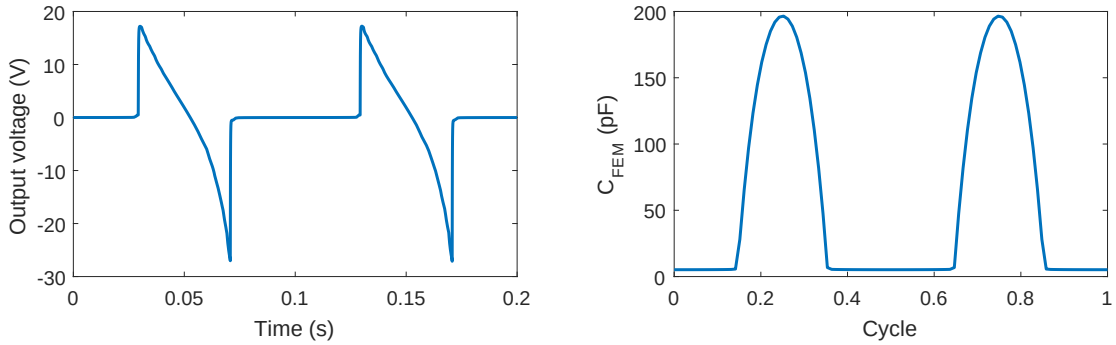

Figure B.6. (a) Output voltage of the liquid-based microgenerator with 5 pF parasitic capacitance at $R_L = 10$ MΩ, and (b) FEM capacitance variation in the time domain is similar to a parabolic wave, leading to a similar output voltage signal presented in Chapter 4.

period in which the capacitance variation is tiny.

Given the simulated resutls in this section, the liquid-based microgenerator is capable of producing adequate amount of energy to power microelectronic devices. The following section will outline the fabrication to prototype a liquid-based microgenerator.

B.3 Fabrication and experiment

This section presents the fabrications of electrets and the liquid-based microgenerator proposed in Appendix B.1 and a preliminary testing result. The section starts with the setup of a corona-discharge station to form electret. The fabrication and assembly of the liquid-based microgenerator is then followed. The final part is the preliminary testing result and a discussion.

B.3.1 Fabrication

For a quick prototype, a 100 μm thick adhesive PTFE tape (3M PTFE Skived Film Tape 5480) is utilized as the dielectric material to form electret. The fabrication process of the prototype is as follows: First, the PTFE adhesive tape is bonded on a

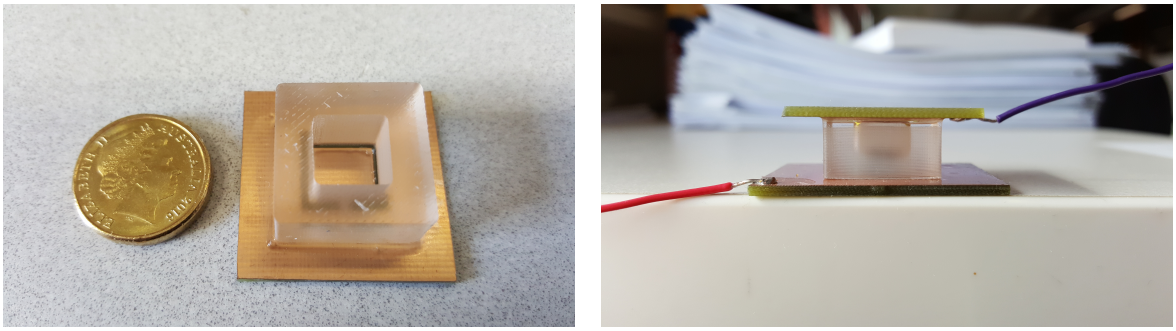

(a) (b)

Figure B.7. A prototype of the liquid-based microgenerator, (a) a PMDS housing is bonded with a copper substrate, and (b) the completed assembly of the prototype.

1-by-1 cm^2 copper substrate. The sample is then corona-charged with the grid voltage of -1 kV. As reported in (Wu et al. 2010), it is necessary to coat the electret with an insulation layer to prevent the retained charges from exacerbating. In this study, PDMS is employed to spin-coat the electret using a rotation speed of 500 rpm for 2 minutes. Second, a PDMS housing is casted and bonded with another prepare substrate as shown in Figure B.7a. A liquid consists of 25 percent sodium chloride mass is then half-filled the cavity. Finally, the substrate with the PDMS-coated electret is bonded with the housing to obtain the encapsulated structure shown in Figure B.7b.

Due to the limited resources available at the university facility, a few parameters of the prototype cannot be determined. The first one is the surface potential of the fabricated electret. Hence, it is assumed to be equal to the gird voltage supplied. The second one is the thickness of the PDMS coated to protect the electret tape. This very thin layer does affect to the performance of the prototype. As a result, future work will need to employ an electrostatic volt meter and a profiler to obtain precise values of these parameters to be able to compare the experimental results with the simulation presented in Appendix B.2.

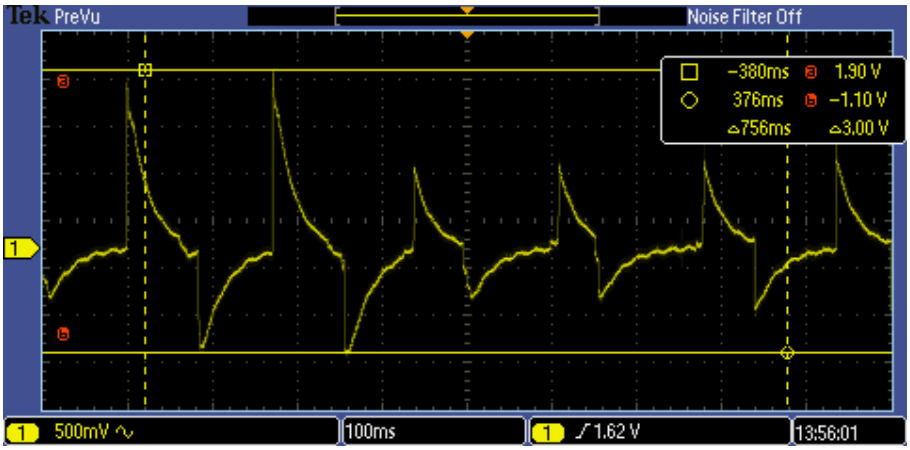

Figure B.8. The liquid-based prototype using Gallium as the conductive liquid can generate up to 1.6 V peak-to-peak voltage when being hand-shaken.

B.3.2 Experiment

As analyzed in Appendix B.2, a small increase of the electret thickness or the insulation layer coated leads to a significant reduction of the output voltage and power. Hence, a 100 μm thick PTFE tape combined with a PDMS layer coated in this experiment is expected to result in a very low performance. Nevertheless, this prototype is to demonstrate the proof-of-concept of this liquid-based microgenerator. The prototype is tested using a non-standard method by using hand-shaking as the external excitation. For the sodium chloride liquid, the open circuit voltage is barely observable through a 20-MΩ oscilloscope. The reason is due to the large thickness of the electret and protective layer used. Hence, another prototype using Gallium as the conductive liquid is made and tested under the same condition without the protective layer. The open circuit voltage result shown in Figure B.8 demonstrates that the prototype can generate up to 1.6 V peak-to-peak.

The signal shape shown in Figure B.8 is different from the simulation results shown in Figure B.6a. The discrepancy is mainly caused by the assumption of rigid-body motion of the liquid. Hence, a refiner model taking the effect of liquid sloshing should be developed to provide a better prediction.

Appendix C

Detailed solutions of differential equations presented in Chapter 5

C.1 Solution of equation (5.10)

To employ the integrating factor to solve equation (5.10), we define a the function $M_1(t)$ such that

$$\begin{aligned} M_1(t) &= \int \frac{dt}{4kR_LC_0\left[\frac{\omega t}{\pi}\left(1-\frac{\omega t}{\pi}\right)-\frac{m}{2k}\right]} \\ &= \frac{1}{2kR_LC_0}\int \frac{dt}{\frac{-2\omega^2}{\pi^2}t^2+\frac{2\omega}{\pi}t-\frac{m}{k}} \\ &= \frac{1}{2kR_LC_0}\frac{\pi}{2\omega\sqrt{1-\frac{2m}{k}}}\ln\left|\frac{\frac{-2\omega^2}{\pi^2}t+\frac{\omega}{\pi}-\frac{\omega}{\pi}\sqrt{1-\frac{2m}{k}}}{\frac{-2\omega^2}{\pi^2}t+\frac{\omega}{\pi}+\frac{\omega}{\pi}\sqrt{1-\frac{2m}{k}}}\right| \\ &= \frac{\pi}{4k\omega R_LC_0\sqrt{1-\frac{2m}{k}}}\ln\left[\frac{\frac{2\omega t}{\pi}-\left(1-\sqrt{1-\frac{2m}{k}}\right)}{\left(1+\sqrt{1-\frac{2m}{k}}\right)-\frac{2\omega t}{\pi}}\right] \\ &= \gamma_{2m}\ln\left(\frac{t-t_{2m}}{t_{2k+1-2m}-t}\right), \end{aligned} \tag{C.1}$$

where γ_j is given in (5.12).

The integrating factor can be calculated using the result of $M_1(t)$ and presented as

$$\exp\left[M_1(t)\right] = \left(\frac{t-t_{2m}}{t_{2k+1-2m}-t}\right)^{\gamma_{2m}}. \tag{C.2}$$

The solution of equation (5.10) can, therefore, be given by

$$\begin{aligned} Q_1(t) &= \beta_1 \exp\left[-M_1(t)\right] - \frac{V_0}{R_L} \exp\left[-M_1(t)\right] \int_{t_{2m}}^{t-t_{2m}} \exp[M_1(t)]\, dt \\ &= \beta_1 \left(\frac{t_{2k+1-2m} - t}{t - t_{2m}}\right)^{\gamma_{2m}} - \frac{V_0}{R_L} \left(\frac{t_{2k+1-2m} - t}{t - t_{2m}}\right)^{\gamma_{2m}} \times \\ &\quad \underbrace{\int_{t_{2m}}^{t-t_{2m}} \left(\frac{t - t_{2m}}{t_{2k+1-2m} - t}\right)^{\gamma_{2m}} dt.}_{N_1(t)} \end{aligned} \tag{C.3}$$

It is worthy to note that the interval of the integral given in $N_1(t)$ is chosen in this case for the time interval $[t_{2m}, t_{2m+1}]$. Similar approach can be carried out for the interval $[t_{2k-2m}, t_{2k+1-2m}]$ by replacing the time instance t_{2m} by t_{2k-2m} in the interval of the interval $N_1(t)$.

$N_1(t)$ has to be rewritten in such a form which can be calculated using the result (3.194-1) in (Gradshteyn & Ryzhik 2014). Let $z = t - t_{2m}$, the representation of the integral $N_1(t)$ in this case is

$$\begin{aligned} N_1(t) &= \int_{t_{2m}}^{t-t_{2m}} \left(\frac{z}{t_{2k+1-2m} - t_{2m} - z}\right)^{\gamma_{2m}} dz \\ &= (t_{2k+1-2m} - t_{2m})^{-\gamma_{2m}} \int_0^z \left(\frac{z}{1 - \frac{z}{t_{2k+1-2m} - t_{2m}}}\right)^{\gamma_{2m}} dz \\ &= \frac{z^{\gamma_{2m}+1}}{(\gamma_{2m}+1)(t_{2k+1-2m} - t_{2m})^{\gamma_{2m}}} \times \\ &\quad {}_2F_1\left(\gamma_{2m}, \gamma_{2m}+1; \gamma_{2m}+2; \frac{z}{t_{2k+1-2m} - t_{2m}}\right). \end{aligned} \tag{C.4}$$

$N_1(t)$ can be simplified by applying the Euler's transformation of hypergeometric

functions (Temme 2011) to present as

$$
\begin{aligned}
N_1(t) = & \frac{z^{\gamma_{2m}+1}}{(\gamma_{2m}+1)(t_{2k+1-2m}-t_{2m})^{\gamma_{2m}}}\left(1-\frac{z}{t_{2k+1-2m}-t_{2m}}\right)^{1-\gamma_{2m}} \times \\
& {}_2F_1\left(1,2;\gamma_{2m}+2;\frac{z}{t_{2k+1-2m}-t_{2m}}\right) \\
= & \frac{z^{\gamma_{2m}+1}(t_{2k+1-2m}-t_{2m}-z)^{1-\gamma_{2m}}}{(\gamma_{2m}+1)(t_{2k+1-2m}-t_{2m})}\,{}_2F_1\left(1,2;\gamma_{2m}+2;\frac{z}{t_{2k+1-2m}-t_{2m}}\right) \\
= & \frac{(t-t_{2m})^{\gamma_{2m}+1}\,(t_{2k+1-2m}-t)^{1-\gamma_{2m}}}{(\gamma_{2m}+1)(t_{2k+1-2m}-t_{2m})}\,{}_2F_1\left(1,2;\gamma_{2m}+2;\frac{t-t_{2m}}{t_{2k+1-2m}-t_{2m}}\right).
\end{aligned}
\tag{C.5}
$$

Given the expression of $N_1(t)$, the solution $Q_1(t)$ can be expressed as

$$
\begin{aligned}
Q_1(t) = \beta_1\left(\frac{t_{2k+1-2m}-t}{t-t_{2m}}\right)^{\gamma_{2m}} & - \frac{V_0\,(t-t_{2m})\,(t_{2k+1-2m}-t)}{R_L(1+\gamma_{2m})(t_{2k+1-2m}-t_{2m})} \times \\
& {}_2\mathrm{F}_1\left(1,2;2+\gamma_{2m};\frac{t-t_{2m}}{t_{2k+1-2m}-t_{2m}}\right).
\end{aligned}
\tag{5.11}
$$

C.2 Solution of equation (5.21)

A similar approach as the one presented in Appendix C.1 is employed to solve equation (5.21). A function $M_2(t)$ is defined such that

$$
\begin{aligned}
M_{21}(t) = = & \int \frac{dt}{2kR_LC_0\left(\frac{2\omega^2}{\pi^2}t^2-\frac{2\omega}{\pi}t+\frac{m+1}{k}\right)} \\
= & \frac{\pi}{4k\omega R_LC_0\sqrt{1-\frac{2m+2}{k}}}\ln\left|\frac{\frac{2\omega^2}{\pi^2}t-\frac{\omega}{\pi}-\frac{\omega}{\pi}\sqrt{1-\frac{2m+2}{k}}}{\frac{2\omega^2}{\pi^2}t-\frac{\omega}{\pi}+\frac{\omega}{\pi}\sqrt{1-\frac{2m+2}{k}}}\right| \\
= & \gamma_{2m+2}\ln\left(\frac{t-t_{2k-2m-1}}{t-t_{2m+2}}\right).
\end{aligned}
\tag{C.6}
$$

The integrating factor is calculated using the result of the function $M_2(t)$ and

expressed as

$$\exp\left[M_{21}(t)\right] = \left(\frac{t - t_{2k-2m-1}}{t - t_{2m+2}}\right)^{\gamma_{2m+2}}. \tag{C.7}$$

The induced charge $Q_{21}(t)$ of equation (5.21) can, therefore, be written as

$$\begin{aligned} Q_{21}(t) &= \beta_{21}\exp\left[-M_{21}(t)\right] - \frac{V_0}{R_L}\exp\left[-M_{21}(t)\right]\int_{t_{2k-2m-1}}^{t-t_{2k-2m-1}}\exp[M_2(t)]\,dt \\ &= \beta_{21}\left(\frac{t - t_{2m+2}}{t - t_{2k-2m-1}}\right)^{\gamma_{2m+2}} - \frac{V_0}{R_L}\left(\frac{t - t_{2m+2}}{t - t_{2k-2m-1}}\right)^{\gamma_{2m+2}} \times \\ &\quad \underbrace{\int_{t_{2k-2m-1}}^{t-t_{2k-2m-1}}\left(\frac{t - t_{2k-2m-1}}{t - t_{2m+2}}\right)^{\gamma_{2m+2}} dt}_{N_{21}(t)}. \end{aligned} \tag{C.8}$$

$N_{21}(t)$ is then rearranged as

$$\begin{aligned} N_{21}(t) &= \int_{t_{2k-2m-1}}^{t-t_{2k-2m-1}}\left(\frac{t - t_{2k-2m-1}}{t - t_{2m+2}}\right)^{\gamma_{2m+2}} dt \\ &= \int_{t_{2k-2m-1}}^{t-t_{2k-2m-1}}\left[\frac{t - t_{2k-2m-1}}{(t_{2k-2m-1} - t_{2m+2}) + (t - t_{2k-2m-1})}\right]^{\gamma_{2m+2}} dt \\ &= (t_{2k-2m-1} - t_{2m+2})^{-\gamma_{2m+2}}\int_{t_{2k-2m-1}}^{t-t_{2k-2m-1}}\left(\frac{z_2}{1 + \frac{z_2}{t_{2k-2m-1} - t_{2m+2}}}\right)^{\gamma_{2m+2}} dz_2, \end{aligned} \tag{C.9}$$

where $z_2 = t - t_{2k-2m-1}$.

Applying the result (3.194-1) in (Gradshteyn & Ryzhik 2014) gives

$$\begin{aligned} N_{21}(t) = &\frac{z_2^{\gamma_{2m+2}+1}}{(1+\gamma_{2m+2})(t_{2k-2m-1} - t_{2m+2})^{\gamma_{2m+2}}} \times \\ &{}_2F_1\left(\gamma_{2m+2}, \gamma_{2m+2}+1; \gamma_{2m+2}+2; \frac{-z_2}{t_{2k-2m-1} - t_{2m+2}}\right). \end{aligned} \tag{C.10}$$

Applying Euler's transform gives

$$N_{21}(t) = \frac{(t - t_{2k-2m-1})(t - t_{2m+2})}{(1+\gamma_{2m+2})(t_{2k-2m-1} - t_{2m+2})} \left(\frac{t - t_{2k-2m-1}}{t - t_{2m+2}}\right)^{\gamma_{2m+2}} \times {}_2F_1\left(1, 2; 2+\gamma_{2m+2}; \frac{t_{2k-2m-1} - t}{t_{2k-2m-1} - t_{2m+2}}\right). \tag{C.11}$$

Therefore, the solution $Q_{21}(t)$ can be obtained as

$$Q_{21}(t) = \beta_{21}\left(\frac{\frac{2\omega t}{\pi} - \alpha_{2m+2}}{\frac{2\omega t}{\pi} - \alpha_{2k-2m-1}}\right)^{\gamma_{2m+2}} - \frac{V_0\,(t - t_{2k-2m-1})\,(t - t_{2m+2})}{R_L(1+\gamma_{2m+2})\,(t_{2k-2m-1} - t_{2m+2})} \times {}_2F_1\left(1, 2; 2+\gamma_{2m+2}; \frac{t_{2k-2m-1} - t}{t_{2k-2m-1} - t_{2m+2}}\right). \tag{5.22}$$

C.3 Solution of equation (5.32)

The integrating factor of equation (5.32) can be calculated as

$$M_{22}(t) = \int \frac{dt}{kR_LC_0\left(1 - \frac{2\omega t}{\pi}\right)^2} = \frac{\pi}{2k\omega R_LC_0\left(1 - \frac{2\omega t}{\pi}\right)}. \tag{C.12}$$

Hence, the solution of equation (5.32) is given by

$$Q_{22}(t) = \beta_{22}e^{\frac{-\pi}{2k\omega R_LC_0\left(1-\frac{2\omega t}{\pi}\right)}} - \frac{V_0}{R_L}e^{\frac{-\pi}{2k\omega R_LC_0\left(1-\frac{2\omega t}{\pi}\right)}} \underbrace{\int e^{\frac{\pi}{2k\omega R_LC_0\left(1-\frac{2\omega t}{\pi}\right)}} dt}_{N_{22}(t)}. \tag{C.13}$$

To obtain the solution, $N_{22}(t)$ must be determined. To achieve that, let

$$\begin{aligned} z_{22} &= \frac{\pi}{2k\omega R_LC_0\left(1 - \frac{2\omega t}{\pi}\right)} \\ \rightarrow t &= \frac{\pi}{2\omega}\left(1 - \frac{\pi}{2k\omega R_LC_0z_{22}}\right) \\ \rightarrow dt &= \frac{\pi^2}{4k\omega^2R_LC_0z_{22}^2}dz_{22}. \end{aligned} \tag{C.14}$$

$N_{22}(t)$ can be rewritten as

$$N_{22}(t) = \frac{\pi^2}{4k\omega^2 R_L C_0} \int \frac{e^{z_{22}}}{z_{22}^2} dz_{22}. \tag{C.15}$$

According to (Gradshteyn & Ryzhik 2014, result 2.325-2), $N_{22}(t)$ can be expressed as

$$\begin{aligned} N_{22}(t) &= \frac{\pi^2}{4k\omega^2 R_L C_0} \left[\mathrm{Ei}\left(z_{22}\right) - \frac{e^{z_{22}}}{z_{22}} \right] \\ &= \frac{\pi^2}{4k\omega^2 R_L C_0} \mathrm{Ei}\left[\frac{\pi}{2k\omega R_L C_0 \left(1 - \frac{2\omega t}{\pi}\right)} \right] - \frac{\pi}{2\omega} \left(1 - \frac{2\omega t}{\pi}\right) e^{\frac{\pi}{2k\omega R_L C_0 \left(1 - \frac{2\omega t}{\pi}\right)}}, \end{aligned} \tag{C.16}$$

where $\mathrm{Ei}(z)$ is an exponential integral function defined as

$$\mathrm{Ei}(z) = -\int_z^{\infty} \frac{e^{-y}}{y} dy. \tag{C.17}$$

Hence, the solution $Q_{22}(t)$ of equation (5.32) can be given by

$$\begin{aligned} Q_{22}(t) = \beta_{22} e^{\frac{-\pi}{2k\omega R_L C_0 \left(1 - \frac{2\omega t}{\pi}\right)}} + \frac{\pi V_0}{2\omega R_L} \left(1 - \frac{2\omega t}{\pi}\right) - \frac{\pi^2 V_0}{4k\omega^2 R_L^2 C_0} \times \\ \mathrm{Ei}\left[\frac{\pi}{2k\omega R_L C_0 \left(1 - \frac{2\omega t}{\pi}\right)} \right]. \end{aligned} \tag{5.33}$$

Appendix D

Scientific genealogy

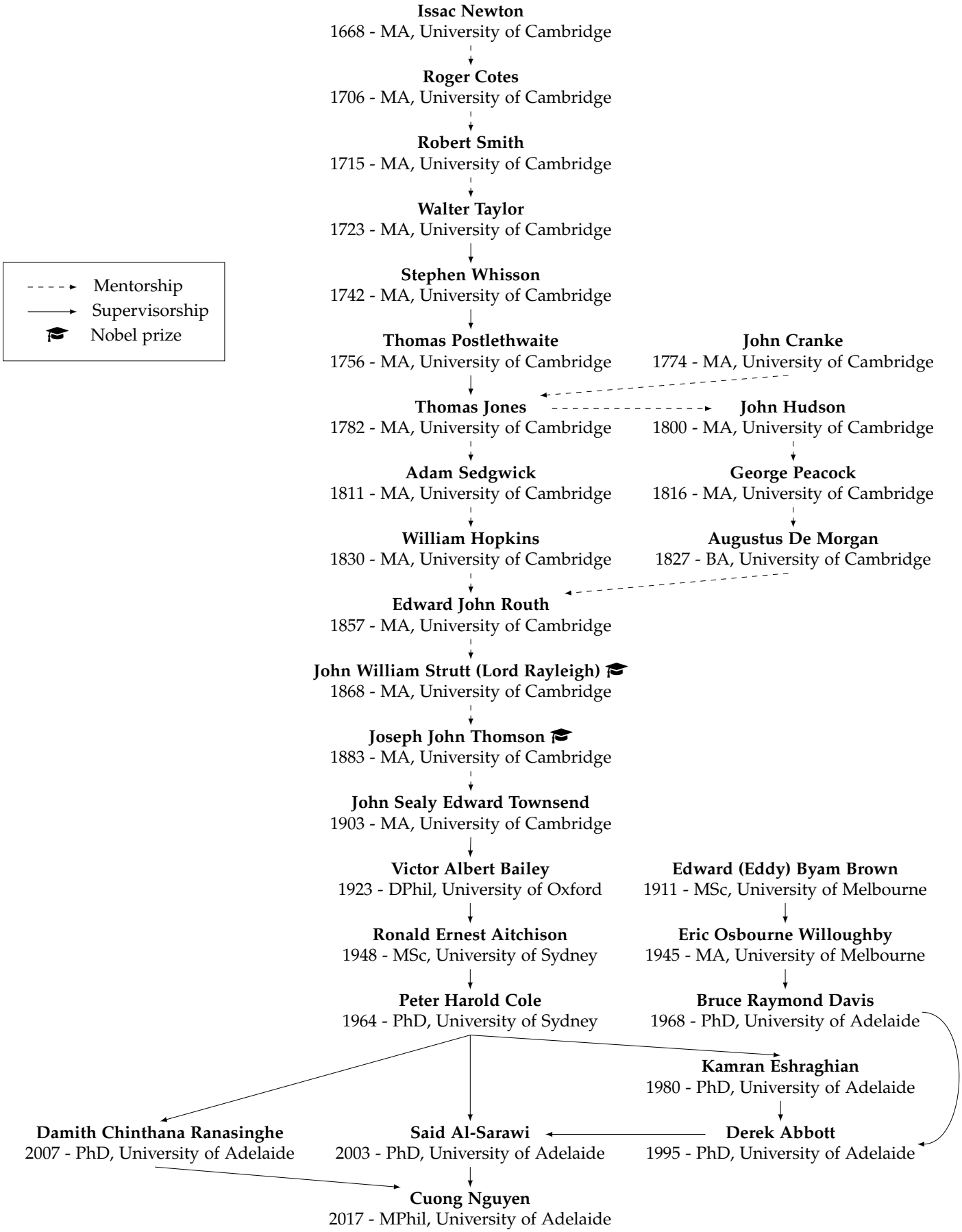
Mentorship
Supervisorship
Nobel prize
Issac Newton
1668 - MA, University of Cambridge
Roger Cotes
1706 - MA, University of Cambridge
Robert Smith
1715 - MA, University of Cambridge
Walter Taylor
1723 - MA, University of Cambridge
Stephen Whisson
1742 - MA, University of Cambridge
Thomas Postlethwaite
1756 - MA, University of Cambridge
John Cranke
1774 - MA, University of Cambridge
Thomas Jones
1782 - MA, University of Cambridge
John Hudson
1800 - MA, University of Cambridge
Adam Sedgwick
1811 - MA, University of Cambridge
George Peacock
1816 - MA, University of Cambridge
William Hopkins
1830 - MA, University of Cambridge
Augustus De Morgan
1827 - BA, University of Cambridge
Edward John Routh
1857 - MA, University of Cambridge
John William Strutt (Lord Rayleigh)
1868 - MA, University of Cambridge
Joseph John Thomson
1883 - MA, University of Cambridge
John Sealy Edward Townsend
1903 - MA, University of Cambridge
Victor Albert Bailey
1923 - DPhil, University of Oxford
Edward (Eddy) Byam Brown
1911 - MSc, University of Melbourne
Ronald Ernest Aitchison
1948 - MSc, University of Sydney
Eric Osbourne Willoughby
1945 - MA, University of Melbourne
Peter Harold Cole
1964 - PhD, University of Sydney
Bruce Raymond Davis
1968 - PhD, University of Adelaide
Kamran Eshraghian
1980 - PhD, University of Adelaide
Damith Chinthana Ranasinghe
2007 - PhD, University of Adelaide
Said Al-Sarawi
2003 - PhD, University of Adelaide
Derek Abbott
1995 - PhD, University of Adelaide
Cuong Nguyen
2017 - MPhil, University of Adelaide